

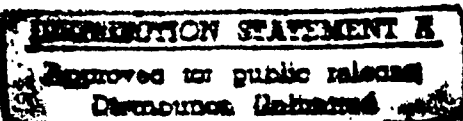


Four-Wave Mixing and Optical Phase Conjugation in
Vertical Cavity Surface Emitting Devices

DISSERTATION

Gregory J. Vansuch, Major, USAF

AFIT/DS/ENP/97-01



DEPARTMENT OF THE AIR FORCE
AIR UNIVERSITY
AIR FORCE INSTITUTE OF TECHNOLOGY

Wright-Patterson Air Force Base, Ohio

19970403 062

AFIT/DS/ENP/97-01

Four-Wave Mixing and Optical Phase Conjugation in
Vertical Cavity Surface Emitting Devices

DISSERTATION

Gregory J. Vansuch, Major, USAF

AFIT/DS/ENP/97-01

DTIC QUALITY INSPECTED 2

Approved for public release; distribution unlimited

**Four-wave Mixing and Optical Phase Conjugation in
Vertical Cavity Surface Emitting Devices**

DISSERTATION

Presented to the Faculty of the School of Engineering
of the Air Force Institute of Technology
Air University
In Partial Fulfillment of the
Requirements for the Degree of
Doctor of Philosophy

Gregory J. Vansuch, B.S., M.A., M.S.
Major, USAF

January 1997

Approved for public release; distribution unlimited

Four Wave Mixing and Optical Phase Conjugation in
Vertical Cavity Surface Emitting Devices

Gregory J. Vansuch, B.S., M.A., M.S.
Major, USAF

Don B. Roh
Dr. Won B. Roh

Chairman, Advisory Committee

16 Jan 97
Date

Jeff W. Grantham
Dr. Jeffrey W. Grantham, Major, USAF

Member, Advisory Committee

8 Jan 97
Date

James A. Lott
Dr. James A. Lott, Major, USAF

Member, Advisory Committee

16 JAN 1997
Date

Paul I. King
Dr. Paul I. King

Dean's Representative

16 Jan 97
Date

Accepted:

Robert A. Calico, Jr.

Dean, School of Engineering

Preface

In this research I examined four-wave mixing (FWM) in Vertical Cavity Surface Emitting Lasers (VCSELs) and Resonant Cavity Light Emitting Diodes (RCLEDs). These are new photonic devices whose microscopic structure offers unique features for optimizing FWM and discerning the conjugate signal produced by the mixing.

Many people contributed to the success of my research. I must first thank Dr. Jeff Grantham, my research advisor. His help was invaluable, from forming the idea to overcoming the many obstacles man and nature put in my way. I'm particularly grateful for his help in the past year, when he was assigned to Wright Labs (Eglin AFB) on other duties and still found time to help me. I thank Dr. Won Roh for his support with sponsor money for equipment to make the experiment happen. Dr. Jim Lott supplied the VCSELs and RCLEDs, the heart of the research, through his work and connections at the University of New Mexico. Mr. Rick Patton provided invaluable technical help in getting the equipment working and keeping it working. And my thanks go to Bill Cooley, who shared my lab, my successes, my frustrations, and learned more about four-wave mixing than he wanted.

Thanks to my sponsors at Wright Laboratory, who provided the funds to make the experiment happen. I'm grateful for the generosity of Profs. Kevin Malloy, Julian Cheng, and Stephen Hersee at the University of New Mexico who grew the VCSELs and graciously gave me a sample--twice!

Finally, I thank my wife, Diana, for her endless support. Without her constant encouragement, I could not have succeeded.

Table of Contents

	Page
Preface.....	iii
Table of Contents.....	iv
List of Figures.....	vi
List of Tables.....	ix
Abstract	x
1. Introduction	1
1.1. Motivation	1
1.2. Problem Statement.....	2
1.3. Research Objectives.....	5
1.4. Organization	5
2. Background.....	6
2.1. Phase Conjugation	6
2.2. Four-wave Mixing.....	8
2.2.1. FWM in Transparent, Non-Absorbing Media	8
2.2.2. FWM in Absorbing Media	14
2.3. Four-wave Mixing in Semiconductor Lasers.....	16
2.4. VCSEL Structure.....	20
2.5. Cavities With Gain	24
3. Methods.....	27
3.1. Experimental Methods	27
3.1.1. Experimental Equipment.....	27
3.1.2. Experimental Procedure.....	30

3.2. Modeling Methods.....	33
3.2.1. Asymmetric Cavity Model	34
3.2.2. Lumped Oscillator Model	46
4. Results and Analysis	51
4.1. RCLED Results	51
4.1.1. Device Information.....	51
4.1.2. Pump-Probe Detuning	54
4.1.3. Pump Power and Bias Current	59
4.1.4. Probe Beam Offset.....	70
4.2. VCSEL Results.....	73
4.2.1. Device Information.....	73
4.2.2. Pump-Probe Detuning	78
4.2.3. Pump Power and Bias Current	82
4.2.4. Pump-Cavity Detuning.....	86
4.2.5. Probe Beam Offset.....	89
4.3. Additional Modeling Results	91
5. Conclusions.....	95
Bibliography.....	97
Appendix A: FORTRAN Code for Asymmetric Cavity Model	104
Appendix B: MathCad Document for Analytic Solution.....	120
Vita.....	127

List of Figures

Figure	Page
1. Typical Edge Emitting Semiconductor Laser	3
2. Typical VCSEL.....	4
3. Wavefront Replication By Phase Conjugate Mirror.....	8
4. Degenerate Four-wave Mixing Geometry	10
5. Electric Susceptibility of a Two-Level System	15
6. Model of Four Wave Mixing in Semiconductors.....	16
7. Transmission of Fabry-Perot Cavity vs. Frequency for Three Incidence Angles	23
8. Reflectivity of Fabry-Perot Cavity with an Active Region	26
9. Experimental Apparatus	28
10. Typical Fabry-Perot Spectrum of Four Wave Mixing.....	31
11. Effect of Pump Jitter on FWM Spectrum	33
12. Calculated Quantum Well Gain vs. Carrier Density	35
13. Calculated Probe and Conjugate Transmissivity vs. Pump-Probe Detuning for Various Lifetimes	43
14. Published Probe and Conjugate Transmissivity vs. Pump-Probe Detuning for Various Lifetimes	44
15. Probe and Conjugate Field Intensity in a Cavity	46
16. Injected Locked Field Intensity vs. Free Running Intensity and Injected Field Intensity	49
17. Spectral Reflectivity of RCLED	53
18. Spectral Measurement of Light from a RCLED	55
19. Light vs. Current for RCLED	56
20. Model Predictions of Conjugate Reflectivity vs. Pump-Probe Detuning for Various Pump Powers.....	57

21. Conjugate Reflectivity in RCLED vs. Pump-Probe Detuning	58
22. Decay Coefficient vs. Pump Power	59
23. Calculated Pump, Probe, and Conjugate Reflectivities vs. Bias Current for Three Hypothetical Cavities.....	60
24. Model Predictions of R_c vs. Pump Power and Current.....	62
25. Conjugate Reflectivity vs. Pump Power and Injection Current.....	63
26. Model of RCLED Reflectivity vs. Current and Injected Power.....	65
27. Measured Mode-Center Reflectivity of RCLED vs. Current and Pump Power	66
28. Spectral Reflectivity of RCLED vs. Current.....	68
29. Spectral Gain and Spontaneous Emission for GaAs Quantum Wells.....	69
30. Optical Flat Creating Parallel, Offset Beams.....	70
31. Angular Discrimination of Conjugate Beam Through a Lens	71
32. Conjugate Reflectivity vs. Pump-Probe Angle.....	72
33. Spatial Separation of Conjugate from Pump and Probe	73
34. Output Power vs. Current for UNM VCSEL	75
35. Spontaneous Emission From UNM VCSEL for Various Currents.....	76
36. Spectral Reflectivity of UNM VCSEL for Various Currents	77
37. Calculated Conjugate Reflectivity vs. Pump-Probe Detuning in VCSEL.....	79
38. Measured Conjugate Reflectivity vs. Pump-Probe Detuning.....	80
39. Spectrum of VCSEL with Injected Pump.....	81
40. Detuned VCSEL and WR vs. Injected Pump Power	82
41. Calculated Probe and Conjugate Reflectivity vs. Pump Power for Various Currents	83
42. Measured Conjugate and Probe Reflectivity vs. Pump Power for Various Currents	84
43. Conjugate and Probe Reflectivity vs. Pump Power and Current.....	85

44. Spectral Reflectivity of VCSEL at 5.5 mA for Three Temperatures	87
45. Pump, Probe, and Conjugate Reflectivity vs. Pump Power and Temperature Tuning	88
46. Spectral Reflectivity of VCSEL for Four Power Levels.....	89
47. Conjugate Reflectivity vs. Pump-Probe Angle.....	90
48. Relative Intensity of Three Beams vs. Razor Blade Position.....	90
49. Calculated Pump, Probe, and Conjugate Reflectivity vs. Current for Three Values of Linewidth Enhancement Factor.....	93
50. Calculated Pump, Probe, and Conjugate Reflectivity vs. Current for Various Pump Powers.....	94

List of Tables

Table	Page
1. Spectral and Angular Half-Width of Fabry-Perot Transmission Modes.....	23
2. Growth Layer Description for UNM RCLED	52
3. Growth Layer Description for UNM VCSEL.....	74

Abstract

Four-wave mixing (FWM), a nonlinear optical process, was investigated in resonant cavity light emitting diodes (RCLEDs) and vertical cavity surface emitting lasers (VCSELs) below lasing threshold. These semiconductor photonic devices consisted of an optical gain region of quantum wells sandwiched between two distributed Bragg reflector (DBR) mirrors. Pump and probe lasers were injected into the devices to generate FWM. The dependence of FWM on bias current, pump laser power, and spectral and spatial separation between pump and probe lasers was investigated experimentally. A computer model of FWM based on the wave and carrier density equations was developed and agreed well with experimental results.

Conjugate reflectivities of 1.0 were obtained in the VCSEL when bias current was below threshold but above transparency. Reasonable conjugate reflectivities were obtained for pump-probe detunings up to 2 GHz in both devices. Noncollinear FWM was performed for the first time in VCSELs or RCLEDs at angles up to 10°. Both experiment and model showed the possibility of generating a strong reflected conjugate signal while minimizing the reflected pump signal. The noncollinear FWM demonstrated the possibility of phase front conjugation for correcting aberrated signals in vertical cavity devices.

1. Introduction

1.1. Motivation

The Air Force interest in optics goes back to its earliest days, when it was primarily a reconnaissance branch of the Army. Since then, we have used optical systems for target detection, identification, and fire control, in addition to the original reconnaissance mission. Two areas of recent heightened interest are the use of optical systems to replace electronics (called photonics) and the use of optical systems (lasers) as weapons. In both of these applications, the transmitting medium (optical fiber or earth's atmosphere) can cause severe aberrations in the optical field over long distances. There are many efforts to correct these aberrations. This thesis addresses one--phase conjugation.

Phase conjugation is a nonlinear optical effect which produces an exact reversal in the phase front of incoming radiation. This results in a beam that retraces the incoming path and completely reverses all of the aberrations induced along the path. This makes phase conjugation an attractive technique for correcting aberrations.

A number of nonlinear optical processes can produce phase conjugation: stimulated Brillouin scattering, the photorefractive effect, and four-wave mixing are the most common. (Fisher, 1983) (Four-wave mixing, the process chosen in the research, will be explained in Chapter 2.) A common requirement for nonlinear optical processes is high optical field intensities. This can be a difficult problem if the signal one seeks to conjugate is a low power laser. A solution is to do the phase conjugation inside a Fabry-Perot cavity, where the internal fields can be much higher than the injected field and allow the nonlinear optical process to occur. It also helps to find a nonlinear medium with a strong electric susceptibility. Some of the largest susceptibilities are in semiconductors when photon energies are near the band gap. (Fisher, 1983: 308) Faced with a small signal to

conjugate, it makes sense to try putting a semiconductor material in a Fabry-Perot cavity as a phase conjugator. The most rugged, compact way to do this is to build a monolithic structure entirely out of semiconductor material. One example of such a structure is a semiconductor laser.

The high efficiency of semiconductor structures is documented in the numerous journal articles on four-wave mixing in semiconductor lasers. Most of these experiments (Chinn, 1991; Jiang, 1994; Liu, 1994; Mecozzi, 1993; Nakajima, 1985b; Simpson, 1993) involve the laser operating above threshold, with the internally generated laser field acting as the pump field and the probe (signal) field injected into the laser. The problem is discrimination of the phase conjugate field from the rest of the fields (pumps and probe). In the experiments, discrimination is achieved by slightly detuning the various fields' frequencies from each other, and using a Fabry-Perot interferometer to distinguish the fields. The use of a narrow band filter to distinguish the conjugate field is not very appealing and not very practical for Air Force applications. It would be better to have another way to discriminate the conjugate field from the rest of the field. This motivates the present research.

1.2. Problem Statement

What can be done to optimize four-wave mixing and phase conjugation in semiconductor lasers? The ideas for this research were motivated by the development of a new type of semiconductor laser: the Vertical Cavity Surface Emitting Laser (VCSEL). Semiconductor lasers have been around since 1962, and have generally been similar to the design shown in Figure 1. Because of their geometry, edge emitters have clear polarization preferences, multiple longitudinal modes due to a long cavity, and an asymmetric beam due to unequal diffraction from the cleaved waveguide facet. The newer VCSEL design, typified by Figure 2, is distinct from the edge emitter in being very short, circular in cross-section, with highly reflective mirrors. As a result, VCSELs have only a

weak polarization preference, a single longitudinal mode, and a symmetrically diffracted beam. A cousin of the VCSEL, the Resonant Cavity Light Emitting Diode (RCLED) differs from the VCSEL only in the number of distributed Bragg reflector (DBR) layers in the mirrors. The RCLED has fewer DBR layers, making lower reflectivity mirrors that prevent lasing, but has highly enhanced spontaneous emission.

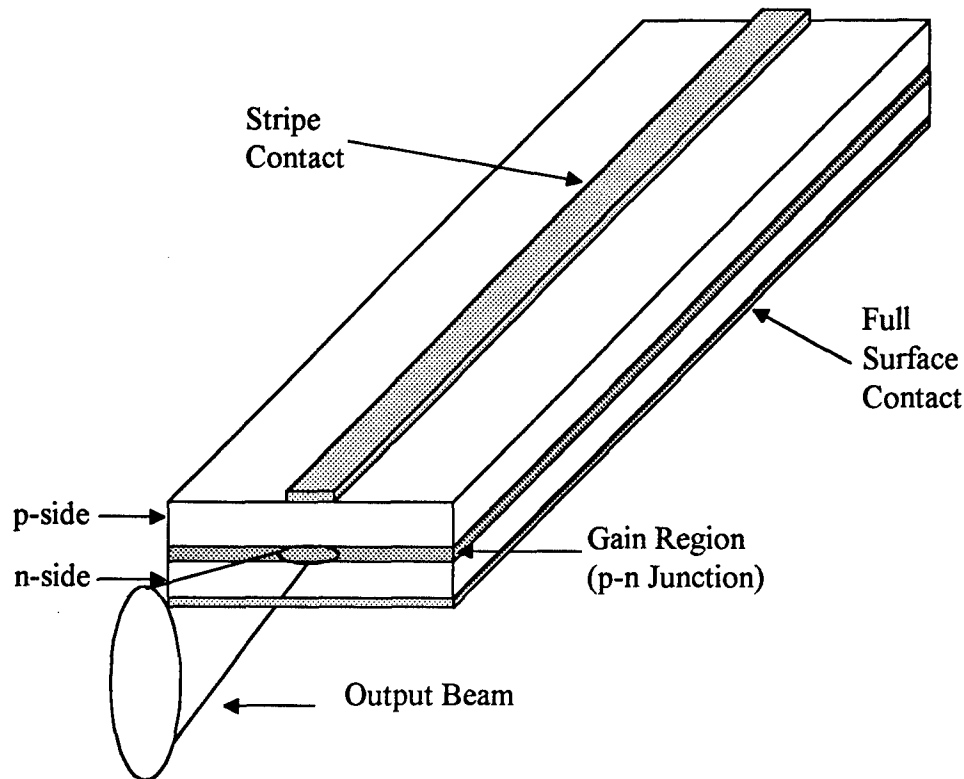


Figure 1. Typical Edge Emitting Semiconductor Laser.

The VCSEL design sparked some ideas for phase conjugation which were pursued in this research effort. First, the mirrors can be grown to the desired reflectivity. Unlike edge emitters, which use the semiconductor-air interface as a weak mirror, VCSEL mirrors are quarter wave stacks of dielectric material, which can be adjusted in reflectivity by varying the number of layers grown. Since the mirror reflectivity can be selected by growth of mirror layers and the gain adjusted by carrier injection, the Fabry-Perot cavity

can be fine tuned until its on-resonance reflectivity is nearly zero. This allows discrimination of the conjugate field, since it will be the only field coming back out of the VCSEL if the normal reflectivity is zero, and maximization of the four-wave mixing.

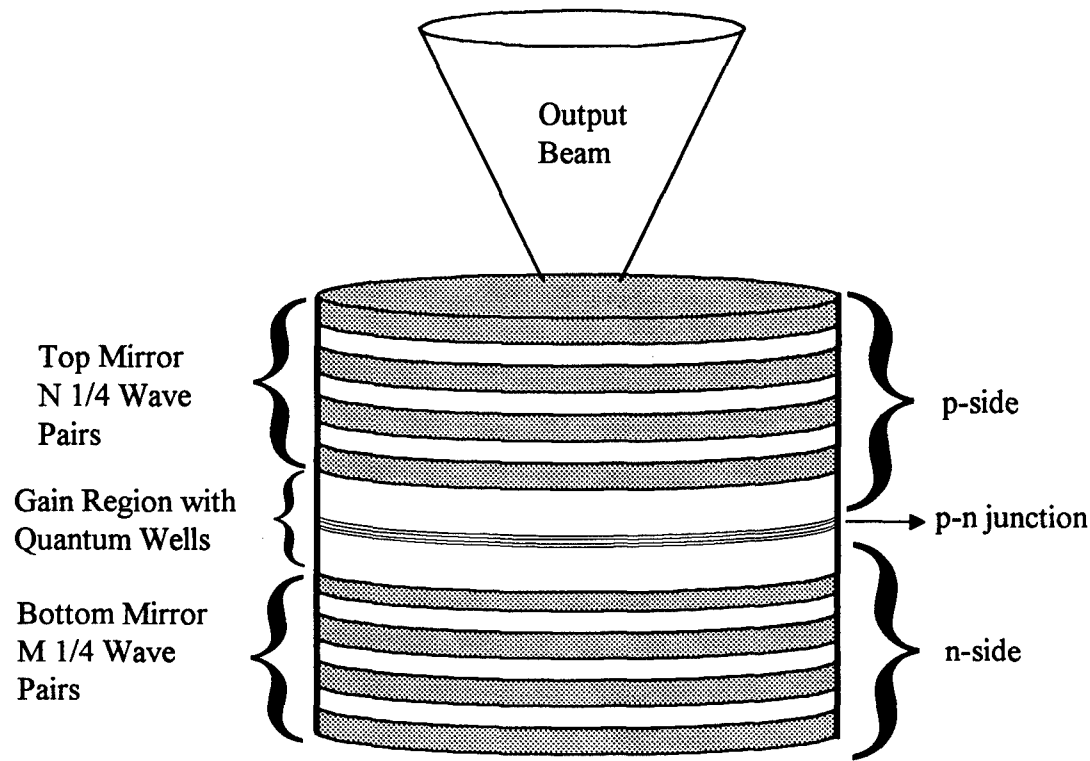


Figure 2. Typical VCSEL.

A second possibility is the use of angle discrimination, which is the most common technique used in most four-wave mixing experiments other than those in semiconductor lasers. VCSELs have such short cavity lengths that the range of angles accepted into the cavity on-resonance is very wide compared to other lasers. Another way to state this is that the VCSEL is a poor spatial filter compared to larger Fabry-Perot cavities. If the probe field can be offset in angle from the pump fields, it should be possible to spatially discriminate the conjugate field from the other fields.

1.3. Research Objectives

The objective of this research was to determine how to maximize the conjugate signal produced by four-wave mixing in RCLEDs and VCSELs below threshold and how to best discriminate the conjugate signal from the pump and probe signals. To do so, the effects of important parameters were studied: current, pump laser power, pump-probe detuning, and pump-probe angle.

1.4. Organization

The remainder of this document explains how the objective of the research were met. Chapter 2 provides background information so the reader can understand the research results. Chapter 3 describes the experimental and modeling methods used in the research. Chapter 4 presents the results and analysis of both experiment and modeling. Chapter 5 summarizes significant conclusions.

2. Background

To make the results of this research clear, some explanation of prior work, concepts, and terms is required. This chapter explains the concepts of phase conjugation and four-wave mixing, describes VCSELs and RCLEDs in some detail, and introduces the idea of a cavity with gain material and cavity balance.

2.1. Phase Conjugation

The ability of phase conjugation to self-correct aberrations in the incoming probe beam is described in many texts. (Butcher, 1990: 235; Fisher, 1983: 1-18) The simplest demonstration of the phenomenon is in Fisher's book. Starting with Maxwell's equations and the assumption that the material is homogeneous, nonmagnetic, nonconducting, with no free charges, one can obtain the standard wave equation in a nonlinear medium for plane waves (in SI units).

$$\nabla^2 \mathbf{E} = \mu_0 \frac{\partial^2 \mathbf{D}}{\partial t^2} = \mu_0 \frac{\partial^2}{\partial t^2} (\epsilon_0 \mathbf{E} + \mathbf{P}) \quad (1)$$

Here \mathbf{E} is the electric field, \mathbf{P} is the polarization, \mathbf{D} is the displacement, ϵ_0 is the vacuum permittivity, and μ_0 is the vacuum permeability, and bold-face indicates a vector or matrix/tensor quantity. The polarization can, in turn, be written as dependent on \mathbf{E} through the electric susceptibility tensor (χ). The susceptibility can be expanded in terms of its dependence on \mathbf{E} , and the terms grouped in a convenient way.

$$\mathbf{P} = \epsilon_0 \chi : \mathbf{E} = \epsilon_0 (\chi^{(1)} + \chi^{(2)} : \mathbf{E} + \chi^{(3)} : : \mathbf{E} \mathbf{E} + \dots) : \mathbf{E} = \epsilon_0 \chi^{(1)} : \mathbf{E} + \mathbf{P}_{NL} \quad (2)$$

In equation (2) the colons (:) represent the operation of a tensor on a number of vectors. The first term in χ is a constant, and the rest of the terms are grouped together to form the nonlinear part of the polarization (\mathbf{P}_{NL}). This can be substituted in equation (1), and by noting $\epsilon = \epsilon_0(1 + \chi^{(1)})$, one can obtain equation (3).

$$\nabla^2 \mathbf{E} - \epsilon \mu_0 \frac{\partial^2 \mathbf{E}}{\partial t^2} = \mu_0 \frac{\partial^2 \mathbf{P}_{NL}}{\partial t^2} \quad (3)$$

This is the classic wave equation in a nonlinear medium with a source term based on the nonlinear polarization. For a linear medium, the source term disappears and it is simply the familiar wave equation.

The aberration-correcting characteristic of phase conjugation can be demonstrated with the case of a monochromatic, non-plane wave propagating in the $+z$ direction through a medium with dielectric constant $\epsilon(\mathbf{r})$. For notational ease, the dielectric constant and the electric field are written as scalars. The electric field can be written as

$$E(\mathbf{r}, t) = \frac{1}{2} \mathcal{E}(\mathbf{r}) \exp(-i(\omega t - kz)) + c.c., \quad (4)$$

where ω is the angular frequency, k is the propagation constant in the medium, \mathcal{E} is the complex amplitude, \mathbf{r} represents the three spatial coordinates, and c.c. means complex conjugate. Putting this wave into the wave equation for a linear medium ($\mathbf{P}_{NL}=0$), we find the resulting equation.

$$\nabla_t^2 \mathcal{E} + [\omega^2 \mu \epsilon(\mathbf{r}) - k^2] \mathcal{E} + 2ik \frac{\partial \mathcal{E}}{\partial z} = 0 \quad (5)$$

As an exercise in mathematics, take the complex conjugate of equation (5), producing

$$\nabla_t^2 \mathcal{E}^* + [\omega^2 \mu \epsilon(\mathbf{r}) - k^2] \mathcal{E}^* - 2ik \frac{\partial \mathcal{E}^*}{\partial z} = 0, \quad (6)$$

assuming that μ and ϵ are real. Note that equation (6) can be interpreted as the same wave equation applied to a wave propagating in the $-z$ direction, with amplitude proportional to the complex conjugate of the original wave. That is, if one can produce a backward-traveling wave with amplitude proportional to the complex conjugate of the incoming wave, it will exactly retrace the path of the incoming wave and replicate its

wavefront *everywhere*. To demonstrate this graphically, Figure 3 shows the wavefront replication by a phase conjugate "mirror" compared to a normal mirror.

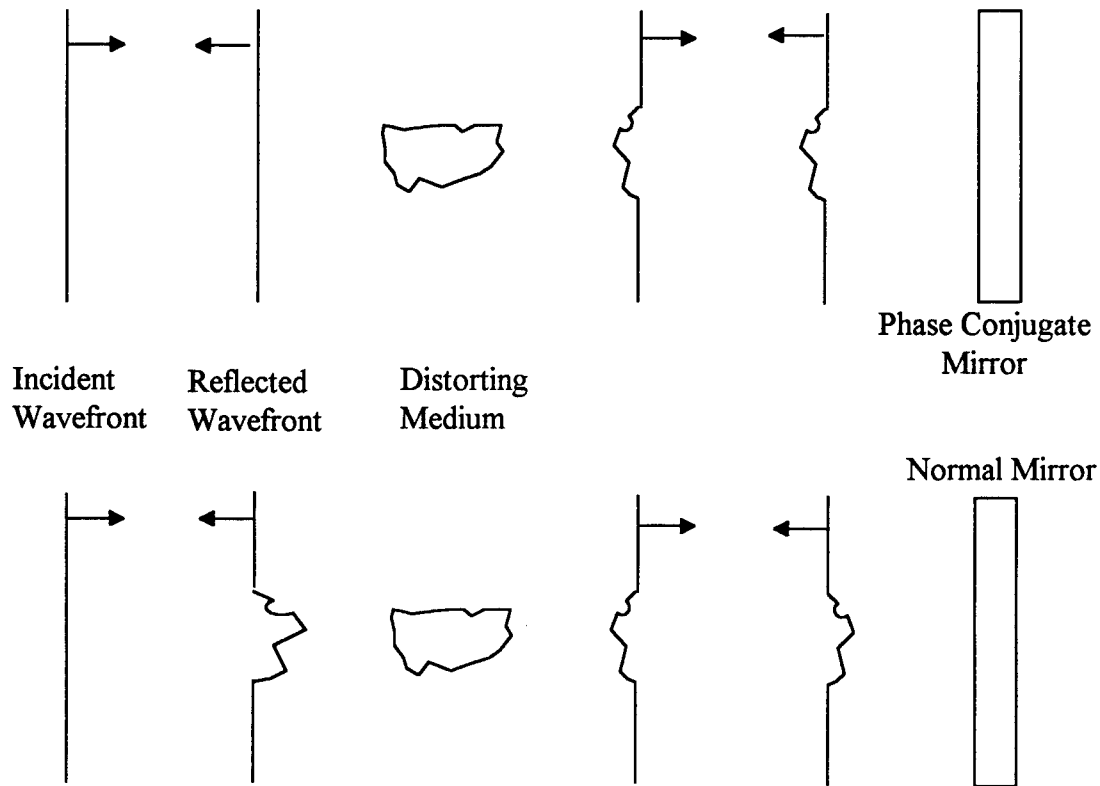


Figure 3. Wavefront Replication By Phase Conjugate Mirror.

The challenge is to produce this phase conjugate wave. A number of nonlinear optical processes have produced phase conjugate waves. The next section examines the process that is most effective in semiconductors: four-wave mixing.

2.2. *Four-wave Mixing*

2.2.1. *FWM in Transparent, Non-Absorbing Media*

The early research in four-wave mixing was for transparent, non-absorbing media. Numerous straightforward explanations of the phenomenon can be found in the literature. (Fisher, 1983: 23-78; Yariv, 1977; Butcher, 1990) The fundamental relationship that

creates the nonlinear mechanism is equation (2), which relates the material polarization (\mathbf{P}) to the electric field (\mathbf{E}). In equation (2) \mathbf{P}_{NL} is described in terms of its dependence on \mathbf{E} , but in general \mathbf{P}_{NL} is a function of many things. For example, as will be shown later, it can be a strong function of carrier density (N) in semiconductors.

But in non-absorbing media, the expansion of χ in terms of powers of \mathbf{E} is the most useful one. One can write equation (2) in component notation and expand χ . The result is equation (7), where the i,j,k,l indices represent directions in Cartesian coordinates ($x=1, y=2, z=3$) and K_n is an integer representing degeneracy of the nonlinear mechanism.

$$P_i = \epsilon_0 \sum_{j=1}^3 \sum_{k=1}^3 \sum_{l=1}^3 (\chi_{ij}^{(1)} E_j + K_2 \chi_{ijk}^{(2)} E_j E_k + K_3 \chi_{ijkl}^{(3)} E_j E_k E_l + \dots) \quad (7)$$

This needs to be simplified for use in the wave equation. The first term (linear) is conventionally absorbed into the expression for ϵ , as shown in the derivation of equations (2) and (3). In a medium with inversion symmetry, including all materials in this study, $\chi^{(n)} = 0$ for n even. (Butcher, 1990: 138) So the first important term in \mathbf{P}_{NL} is the $\chi^{(3)}$ term. In a non-absorbing medium, this term is much larger than higher order terms, so the rest are neglected as an approximation.

Although the transparent medium case does not apply directly to this research, it provides an easy framework for introducing the four-wave mixing (FWM) terminology. The classic FWM experiment involves mixing two strong pump waves and one weak probe wave, to create the fourth wave, called the conjugate wave. A typical FWM configuration is shown in Figure 4.

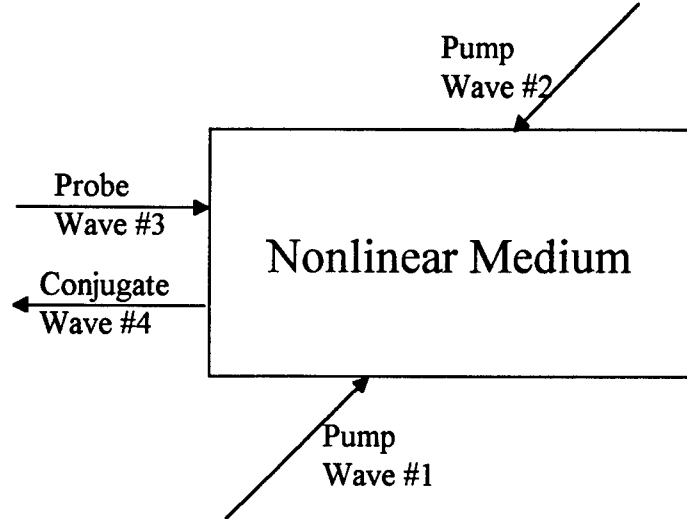


Figure 4. Degenerate Four-wave Mixing Geometry.

To show mathematically how the conjugate wave is generated, the total electric field is written as the sum of all four waves, which in general will have different frequencies (ω_α) and wave vectors (\mathbf{k}_α). By convention, the pump waves are labeled 1 and 2, the probe 3, and the conjugate 4.

$$\mathbf{E}(\mathbf{r}, t) = \frac{1}{2} \sum_{\alpha=1}^4 \bar{\mathcal{E}}(\omega_\alpha, \mathbf{r}) \exp[i(\omega_\alpha t - \mathbf{k}_\alpha \cdot \mathbf{r})] + c.c. \quad (8)$$

Assume there is no conjugate wave initially, so waves 1,2,3 are the sources that generate the \mathbf{P}_{NL} . Using the notation of equation (8) in the $\chi^{(3)}$ term of equation (7), the expression for \mathbf{P}_{NL} is

$$P_i(\mathbf{r}, t) = \frac{1}{2} \epsilon_0 K_{ijkl} (-\omega_\sigma; \omega_1, \omega_2, -\omega_3) \mathcal{E}_{1,j}(\omega_1, \mathbf{r}) \mathcal{E}_{2,k}(\omega_2, \mathbf{r}) \mathcal{E}_{3,l}^*(\omega_3, \mathbf{r}) \times \exp\{i[(\omega_1 + \omega_2 - \omega_3)t - (\mathbf{k}_1 + \mathbf{k}_2 - \mathbf{k}_3) \cdot \mathbf{r}]\} + c.c. \quad (9)$$

In this notation, a positive frequency represents a photon annihilation and a negative frequency represents a photon creation. Note that $\omega_\sigma \equiv \omega_1 + \omega_2 - \omega_3$ refers to the frequency of the *polarization* wave. This expression focuses on the term that involves the

annihilation of two pump photons and the creation of a probe photon. This choice also dictates the minus sign for \mathbf{k}_3 and the complex conjugation of \mathcal{E}_3 . (See Butcher's book for an explanation of the physical reasons behind this notation.) Note that there are many other terms in \mathbf{P}_{NL} , involving different combinations of each of the three types of photons. For example, there is a term with three ω_2 photons, a term with two ω_1 photons and one ω_3 photon, and so on. These give rise to other nonlinear optical effects outside the realm of this study. The term chosen for equation (9) is the FWM term of interest.

To apply this to the experiment indicated in Figure 4, look at the exponential factor in equation (9). The pump beams are opposite in direction, and if $\omega_2 = \omega_1$, then $\mathbf{k}_1 + \mathbf{k}_2 = 0$. The exponential term becomes $\exp\{i[\omega_\sigma t - (-\mathbf{k}_3) \cdot \mathbf{r}]\}$. So the polarization oscillates like a wave traveling *opposite* to the probe with frequency $\omega_\sigma = 2\omega_1 - \omega_3$. FWM is usually described as either degenerate (DFWM) or non-degenerate (NDFWM). Degenerate refers to the case when all waves have the same frequency, so $\omega_3 = \omega_1 = \omega_2$. For NDFWM, the probe frequency is different than the pump frequency, and usually described as $\omega_3 = \omega_1 + \Omega$. As a result the polarization's temporal frequency is $\omega_\sigma = \omega_1 + \omega_1 - \omega_1 = \omega_1 \equiv \omega$ for DFWM, and $\omega_\sigma = \omega_1 + \omega_1 - (\omega_1 + \Omega) = \omega_1 - \Omega \equiv \omega - \Omega$ for NDFWM, so in all cases ω refers to the frequency of the pump wave. For DFWM $-\mathbf{k}_3 = \mathbf{k}_4$, but for NDFWM, $\mathbf{k}_3 + \mathbf{k}_4 = \Delta\mathbf{k} \neq 0$, making a phase mismatch between the polarization wave and the conjugate wave. Sometimes this $\Delta\mathbf{k}$ limits the NDFWM detuning.

This *polarization* wave will, in turn, generate an *electromagnetic* wave with the same frequency (ω_σ). There are two ways to see why this is true. The first is conservation of energy. If there is no absorption occurring in the medium, then if two pump photons are annihilated and one probe photon is created, the extra energy must go into creation of another photon. The energy difference is $h\omega_\sigma/2\pi$, the same frequency as the polarization wave. A second way to look at it is through the power transferred from the \mathbf{P} field to the \mathbf{E} field. As Fisher points out (Fisher, 1983: 9), the power transferred

between the two fields is the volume integral of $\mathbf{P} \cdot \mathbf{E}$, and if the two waves are at different frequencies, the integral (due to orthogonality of complex exponentials) will be zero.

The final step in this analysis shows how the conjugate wave is produced in FWM. As a second order differential equation, the wave equation is difficult to solve. It can be simplified by making the slowly varying envelope approximation (SVEA). First, assume scalar plane waves traveling in the $+z$ direction, as in equation (4), and assume $\mathcal{E}(\mathbf{r}) \approx \mathcal{E}(z)$. That is, the amplitude variation is greatest in the z direction. Applying the wave equation to this wave, we obtain

$$\left(-k^2 \mathcal{E} + \frac{\partial^2 \mathcal{E}}{\partial z^2} + i2k \frac{\partial \mathcal{E}}{\partial z} \right) + \mu_0 \epsilon \omega^2 \mathcal{E} = -\mu_0 \omega^2 \rho \quad (10)$$

where the common complex exponential has been factored out and ρ is the complex amplitude of the polarization vector. The SVEA assumes

$$\left| k \frac{\partial \mathcal{E}}{\partial z} \right| \gg \left| \frac{\partial^2 \mathcal{E}}{\partial z^2} \right| \quad (11)$$

which means the complex amplitude changes slowly on the scale of the wavelength of the light. This is a reasonable assumption in the case of a continuous wave and long smooth pulses. Dropping the second derivative and noting that $k^2 E = \mu_0 \epsilon \omega^2 E$ for a plane wave, we are left with the simplified version of the wave equation.

$$i2k \frac{\partial \mathcal{E}}{\partial z} = -\mu_0 \omega^2 \rho \quad (12)$$

Now inserting the expression for the polarization from equation (9) and bringing the constants to the right side of the equation, we have the relationship between the created wave and the phase conjugate of the pump wave.

$$\frac{\partial \mathcal{E}_{4,i}}{\partial z} = \frac{1}{4} i \epsilon_0 \mu_0 \frac{\omega^2}{k} K_3 \chi_{ijkl} (-\omega_\sigma) \mathcal{E}_{1,j}(\omega_1, \mathbf{r}) \mathcal{E}_{2,k}(\omega_2, \mathbf{r}) \mathcal{E}_{3,l}^*(\omega_3, \mathbf{r}) \times \exp\{i[(\omega - \Omega)t - (-\mathbf{k}_3) \cdot \mathbf{r}]\} + c.c. \quad (13)$$

This is not the full equation; other terms involving the conjugate of fields 1 and 2 exist. But it is clear that in the solution to the set of equations describing the fields there will be a term where $\mathcal{E}_4 \propto \mathcal{E}_3^*$. For the proper boundary conditions and for probe intensities much smaller than pump intensities, this is the dominant term, so within these restrictions the fourth wave is proportional to the complex conjugate of the probe wave.

The generation of the conjugate wave is often described with the terminology of gratings, since the concept of a light wave scattering off gratings is a familiar one. (Fisher, 1983: 49-50) In FWM, two gratings are produced. Pump 1 and the probe interfere to create a spatial intensity pattern, and therefore a spatial pattern of index variation, and pump 2 scatters off it. At the same time, pump 2 and the probe interfere, and pump 1 scatters off their grating. The conjugate wave is the combination of the two scattered waves.

While the geometry in Figure 4 is one of the most common, it is not unique. With an angle between the pump wave and the probe/conjugate waves, the overlap region is small. To maximize the overlap, the waves are made collinear, but this makes it hard to distinguish the conjugate wave from the pumps and probe. One way to solve this is to make the pump waves linearly polarized in one direction and the probe wave polarized in the orthogonal direction. Due to symmetry requirements in cubic crystals, the conjugate wave will then be polarized parallel to the probe wave. Since the probe wave travels in the opposite direction of the conjugate wave, it is easy to distinguish the conjugate wave. Note that this process uses a different element of the tensor $\chi^{(3)}$ than did the previous example. The first case, with everything co-polarized (in the x direction, for example), used the element $\chi^{(3)}_{xxxx}$. The second case used the element $\chi^{(3)}_{xyyx}$, which is usually a smaller value. For cubic crystals, $\chi^{(3)}_{xyyx} = \chi^{(3)}_{xxxx}/3$. (Fisher, 1983: 313-4) Note that

this exact relationship does not necessarily hold in the absorbing cases discussed next. But it's clear FWM with waves of different polarizations will have a smaller χ than if the same waves were co-polarized.

Another way to have collinear propagation and still distinguish the conjugate wave is by changing the frequency of the probe wave and performing non-degenerate four-wave mixing (NDFWM). If the pump waves are at frequency ω and the probe wave is at frequency $\omega+\Omega$, the conjugate wave will be at frequency $\omega-\Omega$, as shown earlier. By resolving the measured field spectrally, one can distinguish the conjugate wave from the pump and probe waves.

2.2.2. *FWM in Absorbing Media*

When operating near an absorption in the medium, it no longer makes sense to expand χ in terms of a power dependence on E , because there is no dominant leading term. For atomic two-level systems, the susceptibility can instead be calculated using density matrix techniques. (Fisher, 1983: 217-222) The resulting expression is

$$\chi = \frac{2\alpha_0}{k} \frac{i(1+i\delta)}{1+\delta^2} \frac{1}{1+|E|^2/I_{sat}} \quad (14)$$

where α_0 is the small signal absorption, k is the wave number, δ is the normalized detuning from line center, I_{sat} is the saturation intensity, and E is the electric field scaled so that $|E|^2$ has units of intensity. Figure 5 shows summations of the first n terms in the polynomial expansion of χ in powers of $|E|$ ($=E$) compared to the full expression in equation (14). It's clear the expansion is useless anywhere near or above the saturation intensity, when $|E|^2=I_{sat}$. Equation (14) has been used with much success to predict the efficiency of DFWM in atomic and molecular systems near resonance. (Abrams, 1978; Brown, 1983)

In semiconductor solids near the band gap energy, we face a similar situation. However, the derivation of χ from first principles is not as straightforward as a two level system. A thorough and insightful derivation is presented by Chow (Chow, 1994: 111-118). The use of Chow's exceeding detailed approach is beyond the scope of this research.

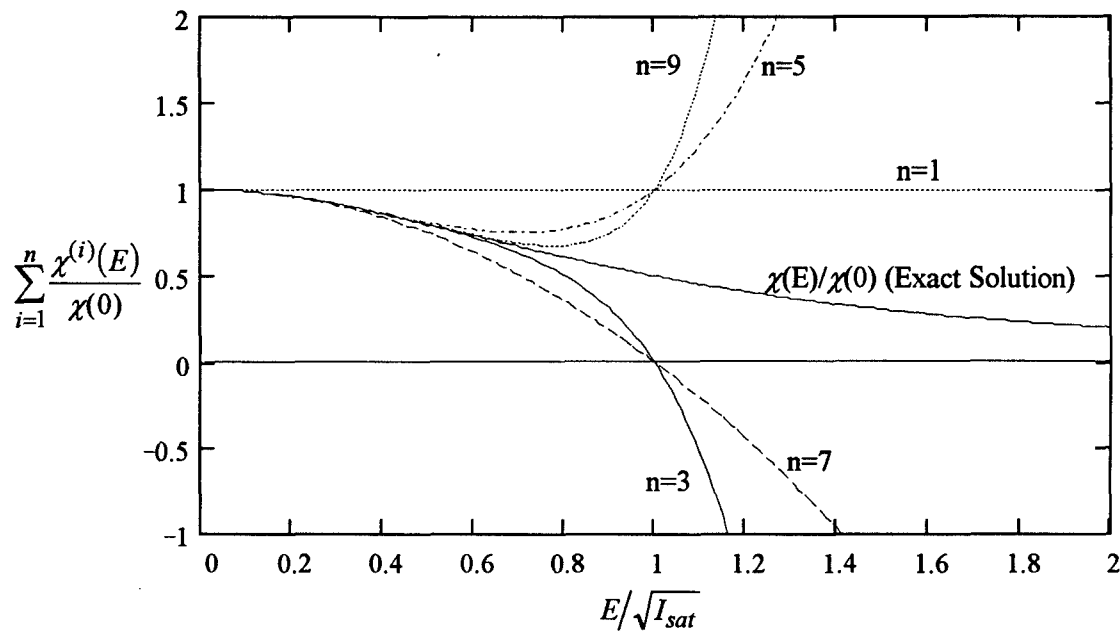


Figure 5. Electric Susceptibility of a Two-Level System. The exact solution is shown along with five polynomial approximations. Note that terms with $i=2,4,6\dots$ are zero.

An early effort to characterize resonant four-wave mixing in a semiconductor (Kukhtarev, 1980) modeled the carrier (N) dependent permittivity as

$$\varepsilon = \varepsilon_0 - \gamma N, \quad (15)$$

where γ is a proportionality constant, and used it with a spatially modulated intensity pattern from the beam interference to create a grating based on carrier density variations. As scalars, the permittivity is related to the susceptibility by $\chi = \varepsilon - 1$. This same picture

has been used by each successive theory (see Figure 6), but adding more details and refinement each time. It differs from the standard theory by having an intermediate mechanism (carrier density N) between the light intensity and the index grating. This means in semiconductors one could achieve the same gratings and nonlinear optical effect by directly modulating the carrier density. A clever experiment involving simultaneous measurement of the optical and electrical spectrum (Nietzke, 1989) showed that the conjugate wave production was directly correlated to carrier density fluctuations in a semiconductor laser, verifying the intermediate step.

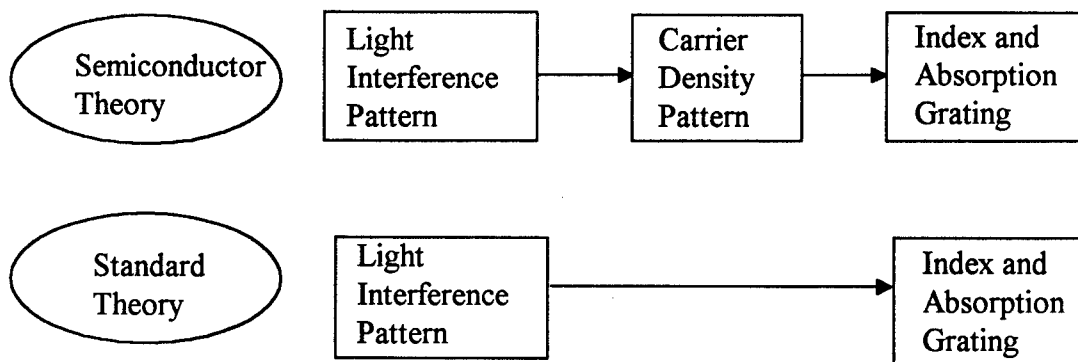


Figure 6. Model of Four-wave Mixing in Semiconductors.

In both theories, the grating explains the creation of the conjugate wave. Any two of the three input waves interfere and create the grating (whether directly or indirectly), while the third input wave scatters off the grating to create the conjugate wave. (Fisher, 1983: 50)

2.3. *Four-wave Mixing in Semiconductor Lasers*

Now we turn to a review of FWM in semiconductor lasers. Most of the experiments and theory have focused on edge-emitting lasers, due to the maturity of the technology. Hundreds of articles have been written on the subject since the first discovery

of the phenomenon. (Nakajima, 1985a/b) Interest is high because NDFWM has a number of uses besides aberration corrections via phase conjugation. These include wavelength conversion and characterization of laser parameters.

Reported FWM experiments in VCSELs have been fewer: only three as of this writing (Boggavarapu, 1993; Jiang, 1994; Simpson, 1995b). All three articles have focused on the fundamental dynamics behind NDFWM. All have investigated VCSELs operating above threshold.

Most of the NDFWM theory has been developed from a fundamental model built by Agrawal. (Agrawal, 1988a) His approach is outlined here. He starts with the wave equation (3) and assumes a field composed of pump ($\omega_0=\omega$), probe ($\omega_1=\omega+\Omega$), and conjugate ($\omega_2=\omega-\Omega$) waves. The susceptibility is assumed to be linearly dependent on the gain and carrier density

$$\chi(N) = -\frac{nc}{\omega}(\beta + i)g(N) = -\frac{nc}{\omega}(\beta + i)a(N - N_0) \quad (16)$$

where N is carrier density, $g(N)$ is the carrier dependent gain, N_0 is carrier density at transparency, a is the linear gain coefficient, c is the speed of light in vacuum, n is the real linear index of refraction, i is the imaginary number, and β is the unitless linewidth enhancement factor, defined as

$$\beta = -\frac{\partial[\text{Re}(\chi(N))]/\partial N}{\partial[\text{Im}(\chi(N))]/\partial N}. \quad (17)$$

Agrawal's fundamental picture of the FWM is a time-domain picture. He assumes the waves are collinear, so there are no spatial gratings in the sense of the original FWM theory. The energy of pump and probe photons are assumed to be above the bandgap of the semiconductor, so we're dealing with a strong absorbing or amplifying medium. This is in contrast to the extensive FWM work done in semiconductors below bandgap.

(Turner, 1996) The interaction is assumed to be NDFWM, and the beat frequency due to the pump-probe detuning produces beats in the carrier density due to gain saturation effects. The carrier density obeys the rate equation

$$\frac{dN}{dt} = \frac{J}{ed} - \frac{N}{\tau_s} - \frac{g(N)}{\hbar\omega} |\mathbf{E}|^2 + D\nabla^2 N \quad (18)$$

with injected current density J , electron charge e , active region thickness d , carrier recombination time τ_s , and diffusion coefficient D . The carrier rate equation is solved using an assumed solution of the form

$$N(t) = \bar{N} + [N_1 \exp(-i\Omega t) + N_1^* \exp(+i\Omega t)], \quad (19)$$

where \bar{N} is the steady state value of the carrier density and N_1 is the small fluctuation of the carrier density. The solution from the carrier density equation is then plugged into the wave equation. Note this form assumes the carrier density fluctuates in time due to the detuning of the pump and probe fields, a process called population pulsations.

The results of four-wave mixing are most often reported as conjugate reflectivity, the ratio of the output conjugate wave intensity to the injected probe wave intensity at the entrance to the device, or

$$R_c = \left| \frac{E_{conjugate}(z=0)}{E_{injected}(z=0)} \right|^2, \quad (20)$$

where the values for $E_{conjugate}$ and $E_{injected}$ are obtained from solving the wave equation using the given boundary conditions. The device extends from $z=0$ to $z=L$. The conjugate reflectivity, which can be greater than 1, depends primarily on Ω , β , J , and the pump power. The mathematical expression for R_c will be presented later, as it depends on the methods and assumptions used to solve the equations. In general, R_c decreases with increasing Ω , and increases with increasing β , J , and pump power.

This fairly simple theory has been adapted to apply to various situations. Agrawal himself has two different solutions, one for $\Omega\tau_s < 1$ and one for $\Omega\tau_s > 1$. For small Ω the dominant mechanism for nonlinearity is actual carrier density modulations. For larger Ω the interband carrier recombination cannot keep up with the temporal speed of the intensity modulations, so a faster but weaker process takes place. Agrawal attributes it to spectral hole burning, a fast intraband process. In later work, others (Tiemeijer, 1991; Mecozzi, 1995a) show that a number of intraband processes (carrier heating, spectral hole burning, Kerr effect, and two photon absorption) are responsible for the FWM at larger detunings. In fact, NDFWM is used to characterize the time constants for each of these mechanisms. (Mecozzi, 1995a)

Agrawal's theory has been the starting point for many modifications. One modification is to introduce gain saturation by the electric field. (Mecozzi, 1993) The expression for susceptibility (equation 16) becomes

$$\chi(N) = -\frac{nc}{\omega}(\beta + i)a(N - N_0)(1 - \sigma|E|^2) \quad (21)$$

with σ the gain compression parameter. Mecozzi solves the equations with this modified gain expression, and gets good correlation to experiment. (Mecozzi, 1993: 1486) Note this gain saturation is not the conventional saturation due to reduction in total carrier density by a field, but is localized saturation of gain at the frequency of the field. It is often called spectral hole burning. (Agrawal, 1988b)

The most important modification applicable to this research is the work by Yee and Shore (Yee, 1994a), which modifies Agrawal's theory to include cavity effects. That is, it explicitly accounts for the forward and backward traveling components of the pump, probe and conjugate waves in a resonant cavity, which Agrawal ignored. In their generalization, they allow for asymmetric cavities, where the asymmetry can be from

unequal mirrors or variations in the current within the cavity. This model served as the basis for most of the modeling work in this dissertation.

A rather different approach has been taken by Simpson and others (Simpson, 1991; Simpson, 1995a/b; Simpson, 1996a; Liu, 1993; Liu, 1994) in a series of articles investigating nonlinear dynamics in semiconductor lasers. Their approach solves the carrier density equation (18) and a rate equation for the field in the cavity instead of the wave equation. These equations will be presented later in the theoretical methods section. Simpson's approach has matched experimental data very well, but has limited use in examining lasers below threshold. (Simpson, 1996)

Finally, while all of the FWM literature in semiconductor lasers is NDFWM in order to allow collinear propagation, one group also tried introducing an angle between the pump and probe beams to achieve angle discrimination. (Awaji, 1993) While successful, they had to use a broad stripe edge emitting laser, and the conjugate reflectivity dropped drastically with angle, from $R_c \approx 50$ at $\theta = 0^\circ$ to $R_c \approx 4$ at $\theta = 5^\circ$. Note the reflectivities are still greater than one. It is not clear whether they attempted DFWM.

2.4. *VCSEL Structure*

The VCSEL structure is different enough from the traditional edge emitting laser that a discussion of how its differences affect FWM is needed. The first difference is the length. While edge emitting lasers are a few hundred μm long, electrically pumped VCSEL cavities are usually less than 1 μm long. Optically pumped VCSELs can be longer, since there is no need for an abrupt p-n junction. This makes the longitudinal mode spacing very large. Typical edge emitter mode spacing is 100 GHz, well within the speed of intraband effects, while a 1λ VCSEL has a mode spacing of 10^5 GHz.

Cavity length also affects the spectral width of the cavity modes and the subsequent spatial and spectral filtering. The shorter the cavity, the broader the spectral and angular acceptance. This can be shown by first deriving the expressions for reflection

and transmission of a simple Fabry-Perot cavity with top mirror reflectivity R_1 and transmittivity T_1 , bottom mirror reflectivity R_2 , amplitude gain γ , cavity length d , input angle θ , wave number k , and refractive index n . The result is

$$R = \left| \sqrt{R_1} - \frac{T_1 \sqrt{R_2} \exp(2\gamma d_{eff}) \exp(i2kd_{eff})}{1 - \sqrt{R_1 R_2} \exp(2\gamma d_{eff}) \exp(i2kd_{eff})} \right|^2 \quad (22)$$

$$T = \left| \frac{\sqrt{T_1 T_2} \exp(\gamma d_{eff}) \exp(ikd_{eff})}{1 - \sqrt{R_1 R_2} \exp(2\gamma d_{eff}) \exp(i2kd_{eff})} \right|^2 \quad (23)$$

where d_{eff} is simply $d/\cos\theta$. The spectral half-width at half-maximum ($\Delta\nu$) can be calculated by finding the value of k where transmission is half of its peak value on resonance, and subtracting it from the adjacent value of k for a resonance peak. The resulting Δk can be transformed into a $\Delta\nu$, resulting in

$$\Delta\nu = \frac{c}{4\pi n d_{eff}} \cos^{-1} \left(2 - \frac{\sqrt{R_1 R_2}}{2} \exp(2\gamma d_{eff}) - \frac{1}{2\sqrt{R_1 R_2}} \exp(-2\gamma d_{eff}) \right) \quad (24)$$

which makes it clear that a smaller d_{eff} results in a larger $\Delta\nu$.

Derivation of the expression for angular half-width at half-maximum ($\Delta\theta_m$) is a little more involved, since it depends on the cavity mode number m . This is shown in Figure 7, which depicts the transmission spectrum for a Fabry-Perot interferometer for three different incident angles. To calculate the angle at which the peak of the off-axis transmission shifts to the half-maximum of the on-axis transmission (my definition of $\Delta\theta_m$), one has to pick a mode m . And clearly for higher m , the $\Delta\theta_m$ will be smaller.

Solving the equations for $\Delta\theta_m$ produces the result in equation (25). The dependence on cavity length is not as clear as in equation (24), because it is embedded in

the mode number m . For a given frequency, the longer the cavity, the greater the mode number of that frequency. Note the $\exp(2\gamma d)$ factor is a much weaker d dependence.

$$\Delta\theta_m = \cos^{-1} \left[1 - \frac{1}{2m\pi} \cos^{-1} \left(2 - \frac{\sqrt{R_1 R_2}}{2} \exp(2\gamma d) - \frac{1}{2\sqrt{R_1 R_2}} \exp(-2\gamma d) \right) \right] \quad (25)$$

Table 1 shows some sample calculations for four different designs. The two VCSELs and the resonant cavity light emitting diode (RCLED) are devices available for this research. (The electrically pumped devices are explained in Tables 2 and 3.) The edge emitter is a typical design. All calculations were done for $n = 3.5$ and setting $\gamma = 0$ for demonstration purposes. It's clear that the short cavities have much broader acceptance, both angularly and spectrally. This angular acceptance can be thought of as a measure of the power of the cavity as a spatial filter. A cavity/laser with narrower angular acceptance will filter out parts of a wave front that deviate too much from a plane wave. The cavities with greater acceptance will allow wavefronts with more aberrations, and perhaps allow a true phase front conjugation. For optical phase conjugation, short cavities are preferable.

Another characteristic of VCSELs that distinguishes them from edge emitters is the high reflectivity mirrors. The resulting high finesse means that an injected probe wave's frequency has to be within the width of the Fabry-Perot transmission mode to successfully make it into the VCSEL cavity. Contrast this to the low finesse edge emitters, where virtually any frequency has a decent input coupling. The high finesse also means the fields inside the VCSEL cavity are much higher than for an edge emitter, given the same injected field. The last column of Table 1 shows the ratio of maximum intensity inside the cavity (I_{max}) to the injected intensity (I_{in}) for the lasers, assuming $\gamma = 0$.

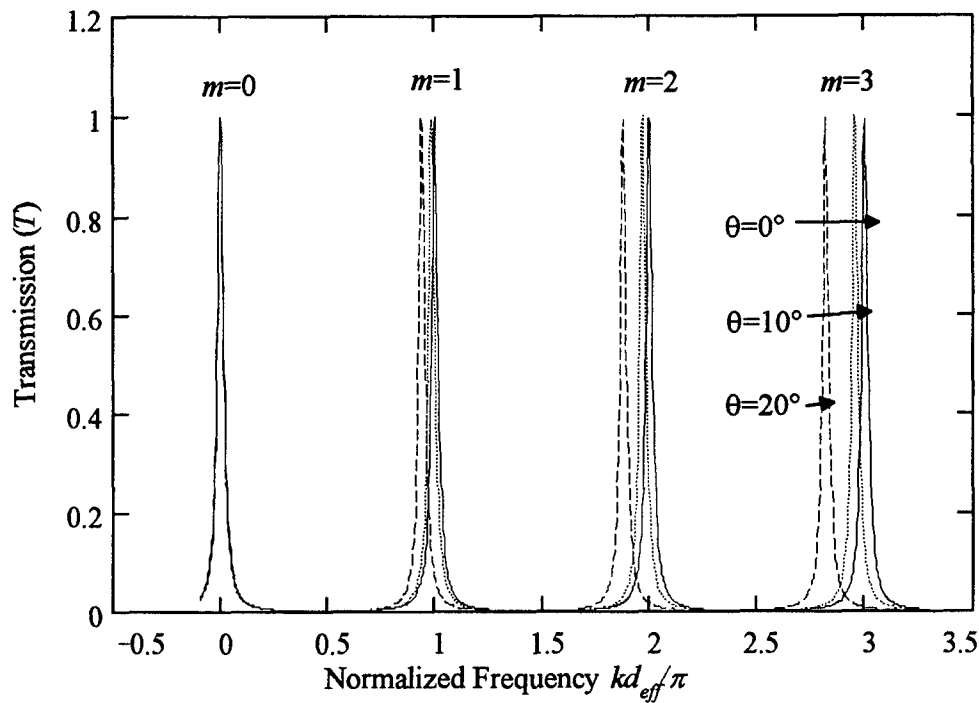


Figure 7. Transmission of Fabry-Perot Cavity vs. Frequency for Three Incidence Angles.

Table 1. Spectral and Angular Half-Width of Fabry-Perot Transmission Modes.

Device	d (μm)	m	R_1	R_2	$\Delta\nu$ (GHz)	$\Delta\theta$ (degrees)	I_{\max}/I_{in}
Electrically Pumped RCLED	0.24	2	0.8	0.98	3460	8.0	60
Electrically Pumped VCSEL	0.24	2	0.98	0.98	574	3.2	200
Optically Pumped VCSEL	2.6	18	0.98	0.98	64	1.08	200
Edge Emitter	426	3550	0.3	0.3	22	0.64	3.5

While VCSELs can be designed to guarantee a single longitudinal mode, the transverse modes are much harder to control. (This is the opposite of edge emitters, where transverse modes are easy to control, and longitudinal modes are notoriously

difficult.) Transverse modes in VCSELs are determined by the waveguide geometry, just as in edge emitters. But many VCSELs are wide enough that microscopic details like the placement of contacts and direction of current flow can determine the transverse modes.

Most VCSELs have a cylindrical geometry, and so have no clear polarization preference, unlike edge emitters which prefer TE modes over TM modes. In fact, there are numerous efforts to introduce some kind of polarization control into VCSELs, without which the polarization is unpredictable from device to device. (Choquette, 1993) For injection of light into a VCSEL at normal incidence, it means that all polarizations have the same input coupling and mode characteristics when the laser is operating below threshold.

2.5. *Cavities With Gain*

This research focused on nonlinear wave mixing in optical cavities with gain/absorption material. The basic equation describing linear reflection and transmission in such a cavity was given in equations (22) and (23). While the reader is certainly familiar with optical cavities, the presence of an active medium introduces effects which are key to this research, and will be introduced here. Figure 8a shows a plot of the spectral reflectivity near one mode of such a cavity for a variety of gain values. Note the two mirrors have unequal reflection coefficients, so with zero gain the total reflection on resonance does not go to zero as it does in Fabry-Perot cavities with equal mirrors. By adding some negative gain (absorption), the reflection on resonance can be made zero, as shown in Figure 8a. When this occurs, we say the cavity is "balanced." One way to think of this is to look at equation 22 and realize that if we replace $\sqrt{R_2} \exp(2\gamma d_{eff})$ with $\sqrt{R_2'}$, we have the same equation as a cavity with no gain and mirror 2 with a new reflectivity of R_2' . When $R_2' = R_1$, the reflectivity on resonance goes to zero; the gain has balanced the cavity.

The value of γd that balances a given cavity is simple to derive from equation (22), and is

$$\gamma d_{eff} = \frac{1}{4} \ln(R_1/R_2) \quad (26)$$

where γ is the amplitude (not intensity) gain coefficient. If the first mirror is more reflective than the second, gain balances the cavity; if the second mirror is more reflective, absorption balances it. This balancing gain value is shown as $\gamma 1$ on Figure 8b. Also shown is the lasing point, where

$$\gamma d_{eff} = -\frac{1}{4} \ln(R_1 R_2) \quad (27)$$

and is labeled $\gamma 2$.

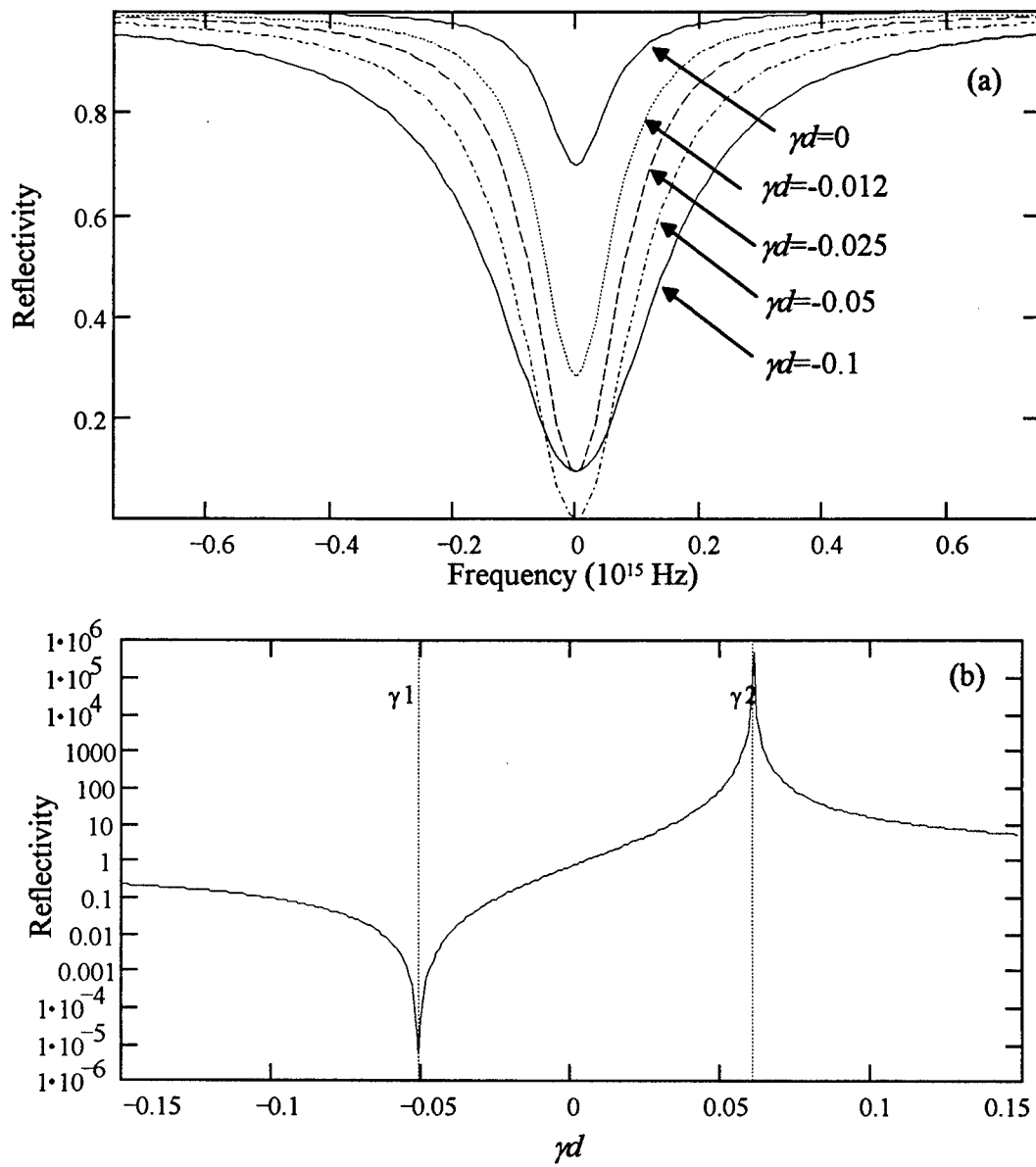


Figure 8. Reflectivity of Fabry-Perot Cavity with an Active Region. Mirror reflectivities are $R_1=0.8$, $R_2=0.98$. Plot (a) shows spectral reflectivity for a few values of γd , while plot (b) shows reflectivity at resonance as a function of gain. The values $\gamma 1$ and $\gamma 2$ are calculated via equations (26) and (27).

3. Methods

The goal was to characterize four-wave mixing in vertical cavity devices below threshold as thoroughly as possible. Although this is primarily an experimental characterization, some theoretical work was done by adapting existing models. The methods used in the investigation are explained below.

3.1. Experimental Methods

This section focuses on the typical experiment used to generate the data being analyzed. Since data are limited by the equipment and techniques used, both are described.

3.1.1. Experimental Equipment

The equipment used in the majority of experiments is depicted in Figure 9. The pump laser was a semiconductor laser (SDL-5422) with power of 150 mW in a single longitudinal mode. It was roughly tuned with temperature and current adjustments, though there were mode hops throughout the tuning regime, which was 839-844 nm. The probe laser was an external-cavity semiconductor laser (New Focus 6226), tuned by a tiltable grating and adjustable cavity length. This gave single mode operation and continuous tunability from 830 nm to 850 nm. The maximum output was about 12 mW. Both lasers were optically isolated to prevent effects of feedback from the mirrors or cross-injection. The lasers were combined at a beamsplitter and carefully aligned to propagate collinearly. One of the beamsplitter output legs went to the VCSEL sample, and the other to a wavemeter (Burleigh WA-10) with 0.002 nm resolution, which was used to tune the two lasers to the same wavelength.

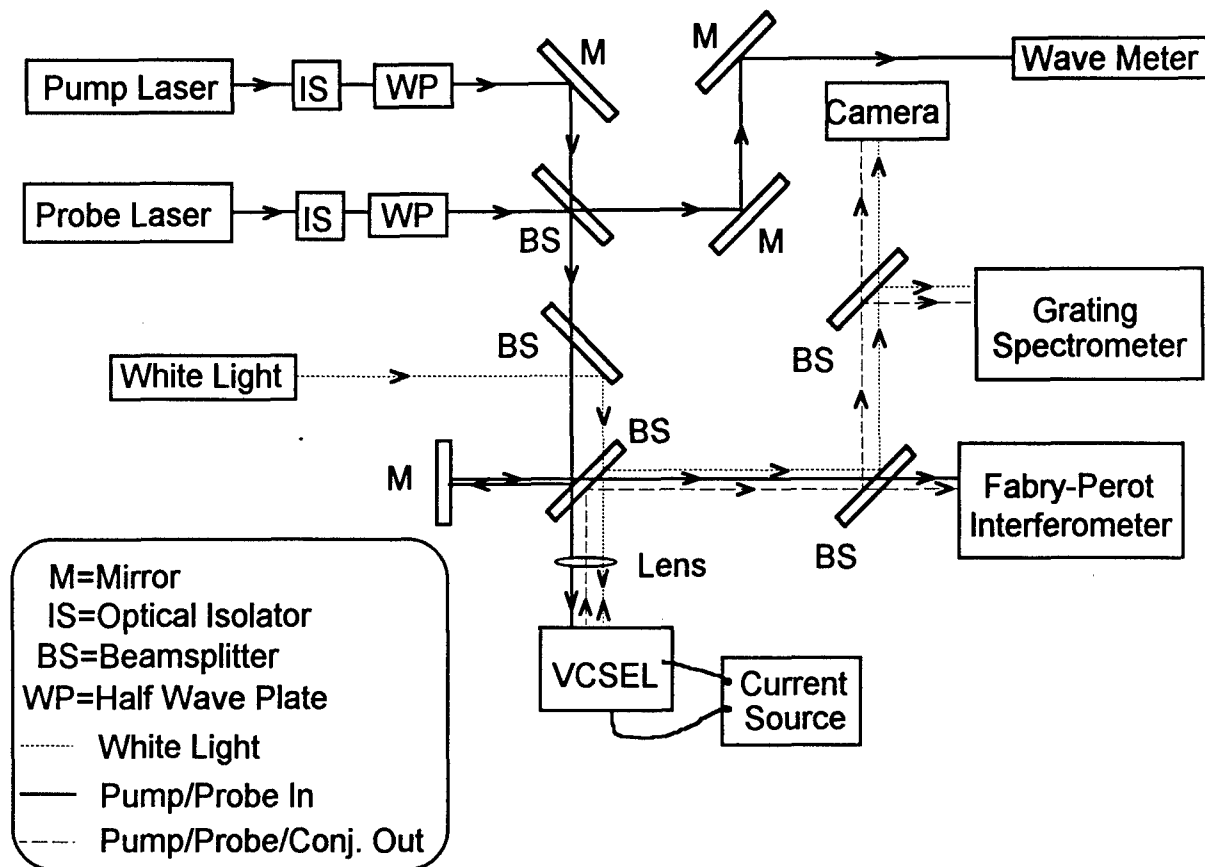


Figure 9. Experimental Apparatus.

The spectral matching of the injected laser to VCSEL was aided by sending a white light through the same path and using a camera to observe the VCSEL surface with the reflected white light. The reflection was also observed on the spectrometer, which displayed the spectral reflectivity of the VCSEL, including the wavelength of the cavity mode.

The VCSEL samples were mounted on a translation stage, which was moved to select a particular device and to adjust the optical injection of the lasers into the VCSEL. The VCSEL was mounted on a copper block, which served as electrical contact for the bottom side of the device and as a thermal conductor for the thermoelectric cooler (TEC).

The TEC adjusted the copper block (and the VCSEL substrate) temperature from about 15°C to 40°C.

After the pump and probe combined in the VCSEL, the resulting output was sent to diagnostic equipment. The camera was used primarily as an optical alignment tool, but also to observe changes in intensity and spatial pattern in the lasers. The spectrometer had an optical multichannel analyzer (OMA) attached, giving spectra in near real time. This was used to coarsely match the input laser wavelengths to the emission wavelength of the VCSEL's Fabry-Perot cavity mode. There were two Fabry-Perot Interferometers (FPI) in the experiment; only one was used at a time. The high resolution FPI was a confocal design (Burleigh SA) with a free spectral range of 2 GHz and a finesse of 150, giving a resolution of 12 MHz. The other FPI (Burleigh RC) had planar mirrors with adjustable free spectral range and finesse of 70. The planar FPI was primarily used with large free spectral range (~100 GHz) to help in coarse wavelength adjustment, observe broad VCSEL lasing lines, and measure large detuning effects.

Other equipment was inserted as necessary. A power meter was used to measure pump or probe laser power at various locations. A polarization analyzer was used to characterize the effects of various elements on the polarization of the beams. A heterodyne system was used to measure the linewidths of both lasers, and consisted of an optical fiber delay line, acousto-optic modulator, fast photodetector, and spectrum analyzer.

With this arrangement the parameters of importance in four-wave mixing in VCSELs could be controlled and measured. Pump and probe power were independently adjusted. Both lasers were tuned relative to the VCSEL and each other. Polarization of both input beams was adjusted to be parallel or orthogonal to each other and the VCSEL's polarization.

3.1.2. Experimental Procedure

The procedure typically used to perform an experiment follows. First the VCSEL device was selected and positioned to inject the pump and probe beam into it, by monitoring the reflection from the VCSEL with the camera. Then the VCSEL bias current was adjusted to the regime of interest.

Tuning the pump laser to the VCSEL wavelength usually required adjusting the pump laser's current and temperature along with the VCSEL's temperature, all while monitoring both pump and VCSEL output on the spectrometer. The spectrometer was only good for matching wavelengths to ± 0.5 nm, which is about 200 GHz. If the VCSEL was lasing, finer tuning was achieved by monitoring the VCSEL and pump on the low resolution FPI and making the current and temperature adjustments. When the VCSEL was below threshold, fine tuning was more difficult. The tunable diode laser (probe) was used to measure spectral reflectivity of the device with 0.002 nm (1 GHz) resolution by tuning the laser, monitoring its wavelength with the wavemeter, and measuring reflectivity wavelength by wavelength. The VCSEL mode wavelength could usually be identified by a dip or peak in the spectral reflectivity. Then temperature and current adjustments were made, and the procedure repeated until the pump laser and VCSEL were tuned appropriately. For the RCLED, the spectral width of the cavity mode was so broad (4 nm) that coarse tuning on the spectrometer was sufficient.

Once the pump laser and VCSEL wavelengths were matched, tuning the probe laser was simple, since it tuned smoothly over the region of interest. The wavemeter was used to match the probe to the pump wavelength to within 0.002 nm (1 GHz). Then the fine resolution FPI, with free spectral range of 2 GHz, was used to get the probe tuned to within 20 MHz of the pump. Once this zero detuning point was found, pump-probe detuning could be monitoring exclusively on the FPI.

Next, the pump power, probe power, VCSEL current or temperature, pump-probe detuning, or whatever parameter was of interest was varied. Note that not all were

equally easy to vary. A change in VCSEL current, for example, shifted the wavelength of the VCSEL, requiring repetition of the elaborate wavelength matching procedures described above. A change in pump-probe detuning, on the other hand, was a simple twist of a knob.

The parameters of interest were typically conjugate reflectivity (R_c), probe reflectivity (R_p), and pump reflectivity (R_{pump} or R). R and R_p are defined like R_c in equation (20), except that R is normalized by the injected pump, not injected probe. R_c and R_p were measured from the FPI. A typical FPI scan is shown in Figure 10, indicating the pump, probe, and conjugate fields. The strengths of the probe and conjugate fields were measured from the height of their peaks on the FPI scan. It was easy to convert this to optical power for the probe, since we could simply send the probe alone into the FPI and measure the response in volts/microwatts.

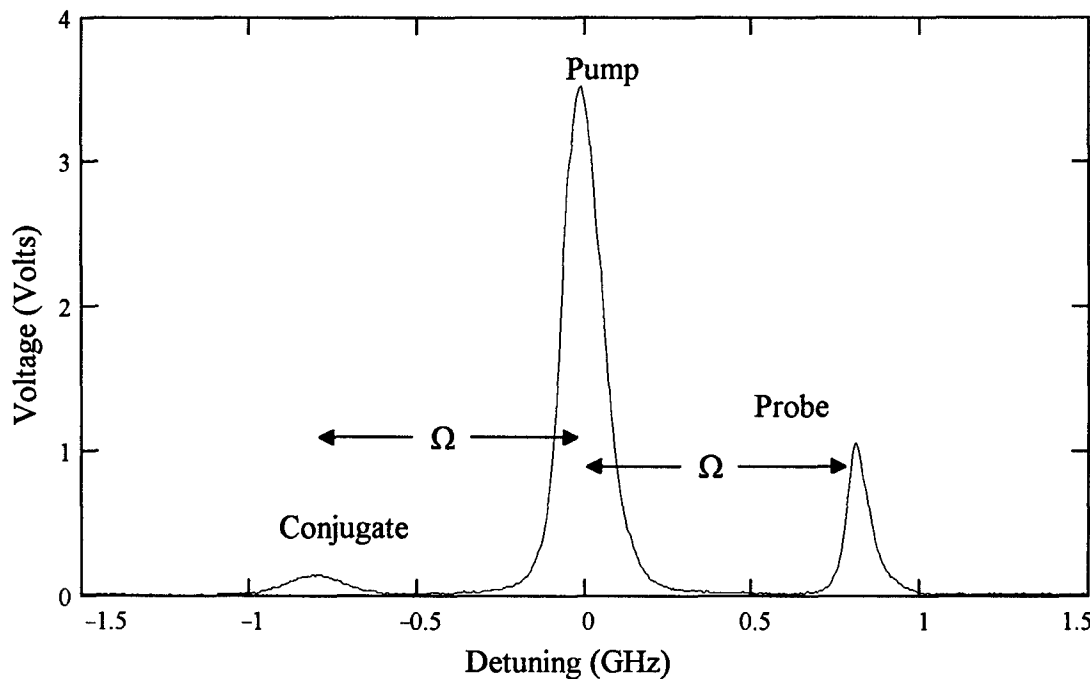


Figure 10. Typical Fabry-Perot Spectrum of Four-wave Mixing.

The same could not be done for the conjugate, which never exists alone and so the power in watts could not be directly measured. The FPI response for the conjugate will be different than for the probe because the conjugate has a different linewidth than the probe. A combination of tools is required to solve this problem. First is a theory about the relative linewidths of the pump, probe, and conjugate fields involved in four-wave mixing. (Hui, 1992) Hui reports that in this kind of experiment, the fundamental linewidths due to spontaneous emission are related by the following equation.

$$\Delta\nu_{conjugate} = 4\Delta\nu_{pump} + \Delta\nu_{probe} \quad (28)$$

These linewidths can be measured with a self-heterodyne technique mentioned earlier and documented in a number of publications. (Gallion, 1984; Ludvigsen, 1994) Measurements showed $\Delta\nu_{probe}=5$ kHz and $\Delta\nu_{pump}=5-15$ MHz, which match manufacturer claims very well, so the linewidth of the conjugate field is dominated by the pump linewidth. Unfortunately other parameters, like jitter of the pump laser and the FPI, obscure this simple relation and make conversion of FPI peak voltage into optical power very uncertain. A demonstration of the pump jitter is shown in Figure 11, which shows four sequential measurements of the FWM spectrum. The probe frequency is relatively steady, but the pump jitters considerably, probably due to imperfect shielding and grounding of the current source. If one tries to average spectra to increase signal-to-noise ratios, the jitter results in considerable smearing of the spectrum, obscuring the simple linewidth relationship derived by Hui.

Because the effect of this jitter varied from day to day and experiment to experiment, conjugate reflectivity results reported herein were calculated with Hui's factor of 4 for consistency purposes. This may over- or under-estimate the values of R_c , but by no more than a factor of two. More importantly, great effort was made to ensure that the

measurement error was consistent within a set of data, making the trends in each set of data valid.

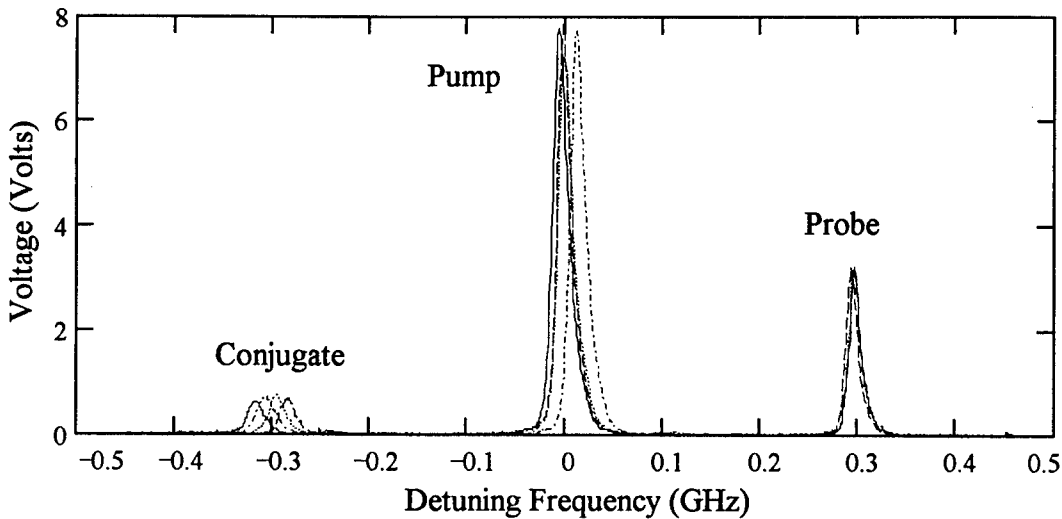


Figure 11. Effect of Pump Jitter on FWM Spectrum. The four scans were taken 30 milliseconds apart, and show maximum frequency shifts of 20 MHz.

3.2. *Modeling Methods*

Because this investigation is primarily experimental, the modeling effort was an adaptation of other researchers' models. The experiments of interest included below threshold and near threshold operation of the VCSELs, which encompass more than the existing models were designed to handle. The adaptations done in this research were to bridge the gaps between the models.

Two models were used. The first was a modified version of the asymmetric cavity model of Yee and Shore (Yee, 1994a). The second was the lumped oscillator model of Simpson and Liu (Simpson, 1991). The asymmetric cavity model was used for the majority of the analysis, since it was the most general and powerful. However, it took longer to run. The lumped oscillator model had analytical solutions and ran much faster,

but applied only to VCSELs near or above threshold. It was used primarily to analyze the effects of pump-probe detuning in the VCSEL near threshold.

3.2.1. Asymmetric Cavity Model

The asymmetric cavity model of Yee and Shore (Yee, 1994a) formed the basis of most of the modeling. Their model, based on the population pulsation concept pioneered by Agrawal (Agrawal, 1988a), envisioned a laser operating above threshold, with gain linearly dependent on carrier density. Their contribution was to allow arbitrary spatial dependence of carriers, and low or unequal mirror reflectivities. Because of this, the solution requires numerical integration of the linear differential equations describing the growth of the pump, probe, and conjugate fields in space. The rest of this section describes the asymmetric cavity model as modified for this research.

The model was adapted to handle the below-threshold case by allowing an injected pump field. The assumption that gain varies linearly with carriers also breaks down when trying to describe both below- and above-threshold behavior, so a nonlinear gain expression was used, of the form

$$g(N) = K_0 - \frac{K_1}{1 + N/K_2} = K_0 - \frac{K_1 K_2}{K_2 + N} \quad (29)$$

where N is the carrier density and the constants (K_0, K_1, K_2) are determined by fitting the equation to a gain curve calculated by other means. In this case, a theoretical model of quantum well gain was used to determine the spectral gain curves for a number of carrier densities. (Fitzgerald, 1994) Then a wavelength was chosen and the gain at that wavelength was plotted versus carrier density and equation (29) fit to the data points. Figure 12 shows a few of the spectral gain plots and the single wavelength gain vs. carrier density.

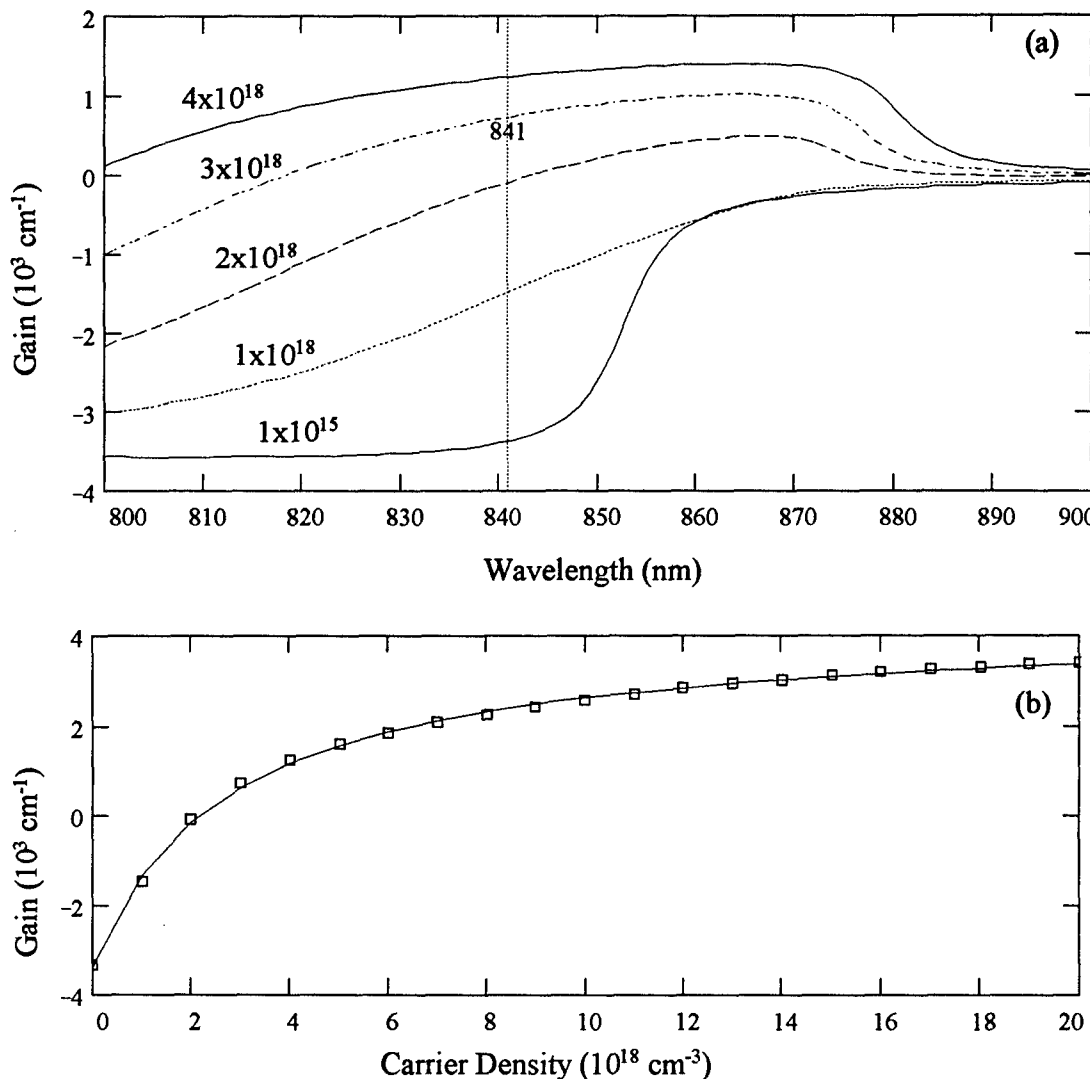


Figure 12. Calculated Quantum Well Gain vs. Carrier Density. (a) shows the full spectral gain for various carrier densities, and plot (b) shows gain at 841 nm for a wider range of carrier densities. Also shown is the curve fitting Equation (29) to the single wavelength gain data. All calculations were for a constant temperature $T=300\text{K}$.

This model solves the wave equation and the carrier density equation. The assumption is that both the material polarization and the electric field oscillate in the form

$$\begin{aligned}
 E(t) &= e^{-i\omega_0 t} (E_0 + E_1 e^{-i\Omega t} + E_2 e^{+i\Omega t}) \\
 P(t) &= e^{-i\omega_0 t} (P_0 + P_1 e^{-i\Omega t} + P_2 e^{+i\Omega t})
 \end{aligned} \tag{30}$$

where ω_0 is the frequency of the strong pump field (E_0) and Ω is the detuning between the pump and the weak probe (E_1). The third field (E_2) is the conjugate field, detuned from the pump field by $-\Omega$. The interaction between the field and the medium is

$$P = \epsilon_0 \chi E. \quad (31)$$

The nonlinear gain expression, equation (29), is substituted into equation (16), resulting in

$$\chi(N) = -\frac{nc}{\omega_0}(\beta+i)g(N) = -\frac{nc}{\omega_0}(\beta+i)\left(K_0 - \frac{K_1}{1+N/K_2}\right). \quad (32)$$

The wave equation is simplified by assuming the fields of interest can be written as scalar fields in a particular transverse mode of the cavity. The three electric fields and three polarization fields can be written as having a common transverse function, so

$$\begin{aligned} E(x, y, z) &= U(x, y) \sum_{j=0}^2 E_j(z) \exp(-i\omega_j t) \\ P(x, y, z) &= U(x, y) \sum_{j=0}^2 P_j(z) \exp(-i\omega_j t) \end{aligned} \quad (33)$$

where $U(x, y)$ is the transverse function representing the mode. The frequencies are linked by the relationship

$$\omega_1 - \omega_0 = \omega_0 - \omega_2 = \Omega. \quad (34)$$

The expressions in equation (33) are substituted in the wave equation, which is then integrated over x and y , giving rise to a confinement factor Γ . The one-dimensional wave equation then becomes

$$\frac{d^2 E_j}{dz^2} + k_j^2 E_j = -\frac{\Gamma \omega_j^2}{\epsilon_0 c^2} P_j \quad (35)$$

where $k_j = n\omega_j/c$ and n is the effective index of refraction for the mode.

The model begins by solving the carrier equation with the carrier diffusion term ignored (36). The effect of diffusion is usually to "wash out" gratings with a small spatial period compared to the diffusion length. But for these VCSELs the carriers are confined to the quantum wells, which are much too thin to have carrier gratings within them, so diffusion effects can be ignored, thus

$$\frac{dN(t)}{dt} = \frac{J}{ed} - \frac{N}{\tau} - \frac{g(N,t)}{\hbar\omega} |E(t)|^2. \quad (36)$$

The expression for a pulsating population, equation (19), is substituted for $N(t)$. For the gain $g(N,t)$ we expand the expression for $g(N)$, equation (29), in a Taylor series about the steady state value of carrier density (\bar{N}) and allow the first order terms to contain the time variation.

$$\begin{aligned} g(N,t) &= g(\bar{N}) + \frac{\partial g}{\partial N} \bigg|_{\bar{N}} (N(t) - \bar{N}) \\ &= K_0 - \frac{K_1 K_2}{\bar{N} + K_2} + \frac{K_1 K_2}{(\bar{N} + K_2)^2} (N_1 e^{-i\Omega t} + N_1^* e^{+i\Omega t}) \\ &\equiv \bar{g} + g' (N_1 e^{-i\Omega t} + N_1^* e^{+i\Omega t}) \end{aligned} \quad (37)$$

The quantities \bar{g} (gain with steady state carrier density) and g' (derivative of gain with respect to carriers at the steady state value) are defined by the final line of equation (37). The expression for the intensity ($|E|^2$) also contains some fluctuation terms. By expanding the expression and assuming $|E_0| \gg |E_1|, |E_2|$ the intensity fluctuations are approximately

$$\begin{aligned} |E|^2 &= \left| e^{-i\omega_0 t} (E_0 + E_1 e^{-i\Omega t} + E_2 e^{+i\Omega t}) \right|^2 \\ &\approx |E_0|^2 + (E_0^* E_1 + E_0 E_2^*) e^{-i\Omega t} + (E_0 E_1^* + E_0^* E_2) e^{+i\Omega t}. \end{aligned} \quad (38)$$

With the expressions for time-varying intensity (38) and carriers (19) in the differential equation, the terms can be grouped according to their dependence on Ω . The resulting equations can be used to solve for \bar{N} and N_1 . After considerable algebra, the results are

$$\begin{aligned}\bar{N} = & -\frac{1}{2} \left(K_2 - \frac{J\tau}{ed} + \frac{\Gamma\tau K_0}{\hbar\omega} |E_0|^2 \right) \\ & + \frac{1}{2} \sqrt{\left(K_2 - \frac{J\tau}{ed} + \frac{\Gamma\tau K_0}{\hbar\omega} |E_0|^2 \right)^2 - 4 \left(\frac{\Gamma\tau K_2(K_0 - K_1)}{\hbar\omega} |E_0|^2 - \frac{J\tau}{ed} K_0 \right)}\end{aligned}\quad (39)$$

$$N_1 = \frac{-\frac{\Gamma Q\tau}{\hbar\omega} \left(K_0 - \frac{K_1 K_2}{\bar{N} + K_2} \right)}{\frac{\Gamma\tau |E_0|^2}{\hbar\omega} \frac{K_1 K_2}{(\bar{N} + K_2)^2} + 1 - i\Omega\tau}\quad (40)$$

where $Q = E_0^* E_1 + E_0 E_2^*$ for convenience and Γ is the confinement factor derived earlier.

With these solutions for the carrier density quantities, we return to the wave equation and the relationship between the medium polarization and the fields. Substituting equations (19), (30) and (32) into equation (31), we obtain

$$P_0 + P_1 e^{-i\Omega t} + P_2 e^{+i\Omega t} = \epsilon_0 M \left[\bar{g} + g' \left(N_1 e^{-i\Omega t} + N_1^* e^{+i\Omega t} \right) \right] (E_0 + E_1 e^{-i\Omega t} + E_2 e^{+i\Omega t}) \quad (41)$$

where $M = -nc(\beta + i)/\omega$. Again, dropping terms involving the product of two small coefficients, we can solve for the polarization terms,

$$\begin{aligned}P_0 &= \epsilon_0 M (\bar{g} E_0) \\ P_1 &= \epsilon_0 M (\bar{g} E_1 + g' N_1 E_0) = \epsilon_0 M \bar{g} (E_1 - \Delta n_\Omega E_0) \\ P_2 &= \epsilon_0 M (\bar{g} E_2 + g' N_1^* E_0) = \epsilon_0 M \bar{g} (E_2 - \Delta n_\Omega^* E_0)\end{aligned}\quad (42)$$

where $\Delta n_\Omega \equiv -N_1 g'/\bar{g}$. These terms go in the differential equation (12) describing the growth and decay of the various fields.

To account for cavity effects, we write the electric field in the cavity as the sum of a forward- and backward-traveling wave, which will then be subject to the boundary conditions at the edges of the cavity. The polarization is also written with a forward and backward component. Thus we have

$$\begin{aligned} E_j(z) &= \sqrt{I_s} \left[A_j^+(z) \exp(ik_0 z) + A_j^-(z) \exp(-ik_0 z) \right] \\ P_j(z) &= P_j^+(z) \exp(ik_0 z) + P_j^-(z) \exp(-ik_0 z), \end{aligned} \quad (43)$$

where I_s is the saturation intensity and k_0 is the wavenumber for the pump field. These expressions are substituted into the wave equation (35), which is then simplified using the slowly varying envelope approximation to give a set of linear differential equations. The expressions for polarization (42) are also substituted, yielding

$$\frac{dA_0^\pm}{dz} = \pm \frac{i\omega_0 \Gamma}{2nc\epsilon_0 \sqrt{I_s}} P_0^\pm = \frac{\Gamma}{2} (1 - i\beta) \bar{g} A_0^\pm \quad (44)$$

$$\frac{dA_1^\pm}{dz} \mp \frac{in\Omega}{c} A_1^\pm = \pm \frac{i\omega_0 \Gamma}{2nc\epsilon_0 \sqrt{I_s}} P_1^\pm = \frac{\Gamma}{2} (1 - i\beta) \bar{g} (A_1^\pm - \Delta n_\Omega A_0^\pm) \quad (45)$$

$$\frac{dA_2^\pm}{dz} \pm \frac{in\Omega}{c} A_2^\pm = \pm \frac{i\omega_0 \Gamma}{2nc\epsilon_0 \sqrt{I_s}} P_2^\pm = \frac{\Gamma}{2} (1 - i\beta) \bar{g} (A_2^\pm - \Delta n_\Omega^* A_0^\pm) \quad (46)$$

These look deceptively simple. The gain coefficient \bar{g} depends on the fields and therefore on z , and Δn_Ω depends on the fields and z through Q . But if the pump is much stronger than the probe or conjugate, \bar{g} will depend only on the pump field and so equation (44) is independent of probe and conjugate. It was solved using the piecewise constant inversion population (PCIP) approximation (Middlemast, 1991; Yee, 1994a), which breaks the gain region into chunks in which the gain is assumed constant. For a

VCSEL with quantum well gain, this is obviously a good assumption! First the gain and field were set to guessed values. This gain was put into equation (44), which was integrated piecewise along the cavity in the positive direction to calculate the forward field. This new forward field was used to saturate the gain and the boundary condition set the value of the backward wave at $z=L$. Then equation (44) was integrated in the backward direction. The new backward field was then used to calculate a new saturated gain, and the forward field was set by the boundary condition at $z=0$. This iteration continued until the fields and the gain were self-consistent.

Once the pump field and gain were calculated, the probe and conjugate fields could be calculated from equations (45) and (46). The fields are broken into a forward and backward wave amplitudes for both the probe and conjugate. Since the amplitudes are complex, there are a total of eight quantities to be calculated. The system of eight coupled linear differential equations with four boundary conditions on each end is then solved using a standard finite difference approach. The $i\Omega/c$ terms in equations (44) and (45) represent the Δk phase mismatch between the probe and conjugate. For VCSELs they have little effect until Ω is near the VCSEL mode spacing, a few THz.

The boundary conditions are simply that the forward and backward electric fields at a mirror are related by the mirror reflectivity. This is easily written as

$$E_j^+(0) = \sqrt{1 - R_1} E_{inj} + \sqrt{R_1} E_j^-(0) \quad (47)$$

$$E_j^-(L) = \sqrt{1 - R_2} E_j^+(L) \quad (48)$$

where R_i is the reflection coefficient for the i th mirror and E_{inj} is the injected probe field and is set to zero when $j=2$. Using the notation introduced in equation (43), the boundary conditions can be written for the complex amplitudes (A_j) as

$$A_j^+(0) = \sqrt{1-R_1} A_{inj} + \sqrt{R_1} A_j^-(0) \quad (49)$$

$$A_j^-(L) \exp(-i\kappa L) = \sqrt{1-R_2} A_j^+(L) \exp(i\kappa L) \quad (50)$$

where κ is the wave number of the pump field in the cavity. Once these boundary conditions are met, the reflected fields are calculated from the relations

$$R_p = \left| \frac{\sqrt{1-R_1} A_1^-(0) - \sqrt{R_1} A_{inj}}{A_{inj}} \right|^2 \quad (51)$$

$$R_c = \left| \frac{\sqrt{1-R_2} A_2^-(0)}{A_{inj}} \right|^2 \quad (52)$$

The original model assumed the pump field was the self-generated lasing field. This allowed the boundary conditions for the pump field to be very simple: a round trip produced an amplitude gain of unity and a phase delay equal to a multiple of 2π . Put more directly, the self-generated lasing field obeys

$$\sqrt{R_1 R_2} \exp \left[\int_0^L (g(z) - \alpha_{loss}) dz \right] \exp \left[i \left(2\kappa L - \int_0^L \beta g(z) dz \right) \right] = 1 \quad (53)$$

where α_{loss} introduces field losses other than the mirrors and active region absorption, such as scattering losses. When a pump field is injected, the amplitude can still be solved self-consistently using the PCIP method, but equation (53) is not correct.

The model was modified to show this, and to allow injection of the pump field at a frequency different than the solitary laser mode. The objective was to find an expression for $2\kappa L$ to use in boundary condition (50). For the solitary laser, the phase obeys

$$2\kappa L - \int_0^L \beta g_0(z) dz = m2\pi + \theta = \phi_0, \quad (54)$$

where $g_0(z)$ is the gain with no injected pump and ϕ_0 represents the phase for the solitary cavity mode. When the pump is injected, it either creates a field if the laser was below threshold or locks the field if the laser was above threshold. The phase now obeys

$$2\kappa L - \int_0^L \beta g(z) dz = \phi \quad (55)$$

where $g(z)$ is the gain saturated by the injected pump field. The wave number (κ) in boundary equation (50) now obeys

$$\exp(i2\kappa L) = \exp\left[i\left(m2\pi + \theta + \int_0^L \beta g_0(z) dz\right)\right] = \exp\left[i\left(\theta + \int_0^L \beta g_0(z) dz\right)\right] \quad (56)$$

and so does not depend on the injected pump. However, if we want to know the difference in phase between the solitary laser mode and the cavity mode after gain has been saturated by a strong pump, it is simply

$$\Delta\phi = \int_0^L [g(z) - g_0(z)] dz \quad (57)$$

which may be useful for comparison to other researchers looking at injection locking.
(Simpson, 1995b; Petitbon, 1988; H. Li, 1996)

The FORTRAN computer program implementing this model is in Appendix A. This program was validated in two ways. First, output from the model was compared to results published by Yee and Shore in their original article (Yee, 1994). Figure 13 shows results from the model as written in Appendix A. Figure 14 shows the same calculation as published by Yee and Shore in their article. The two results agree very well. Model results were compared to other cases in the same article and agreed very well.

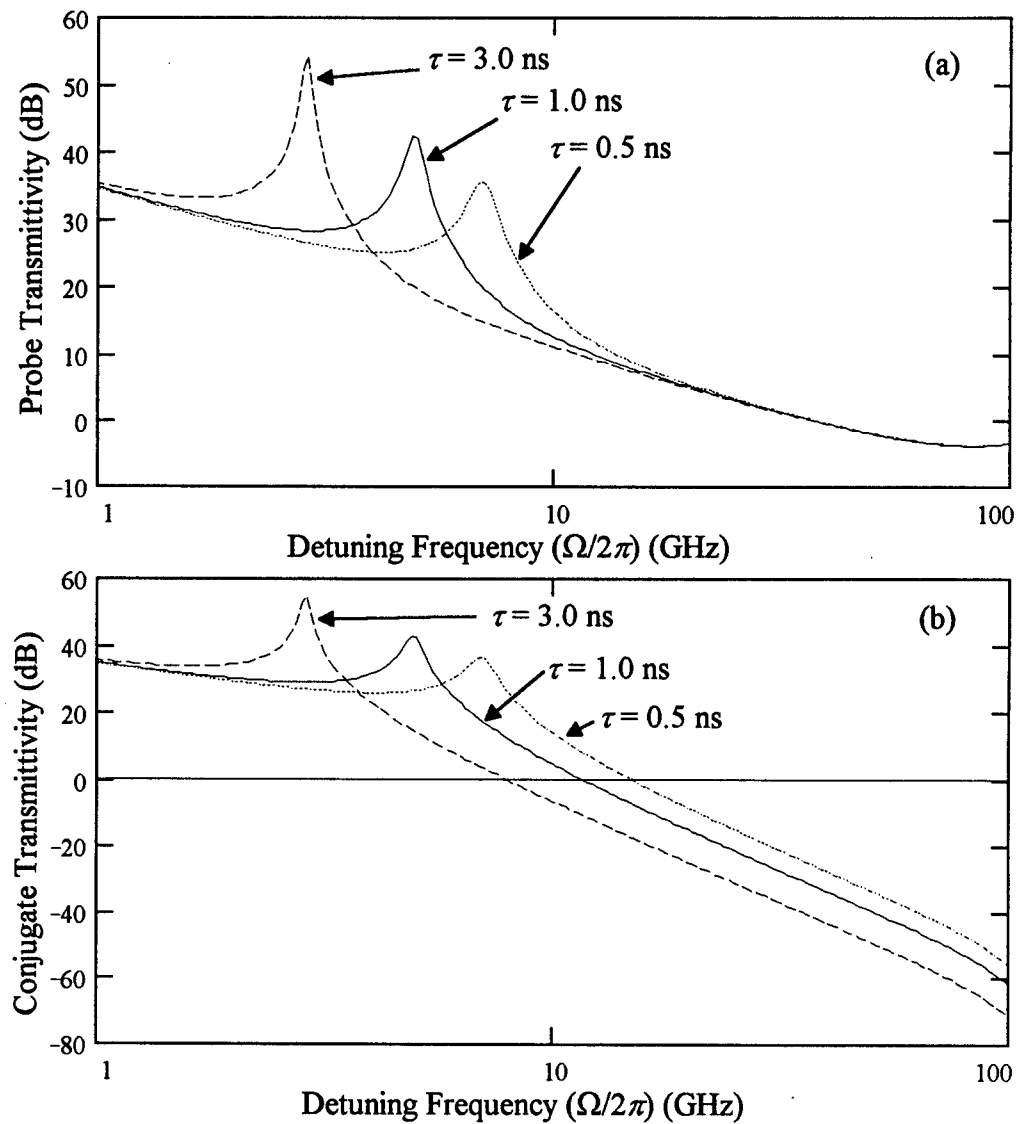


Figure 13. Calculated Probe and Conjugate Transmittivity vs. Pump-Probe Detuning for Various Lifetimes. (a) shows probe and (b) shows conjugate.

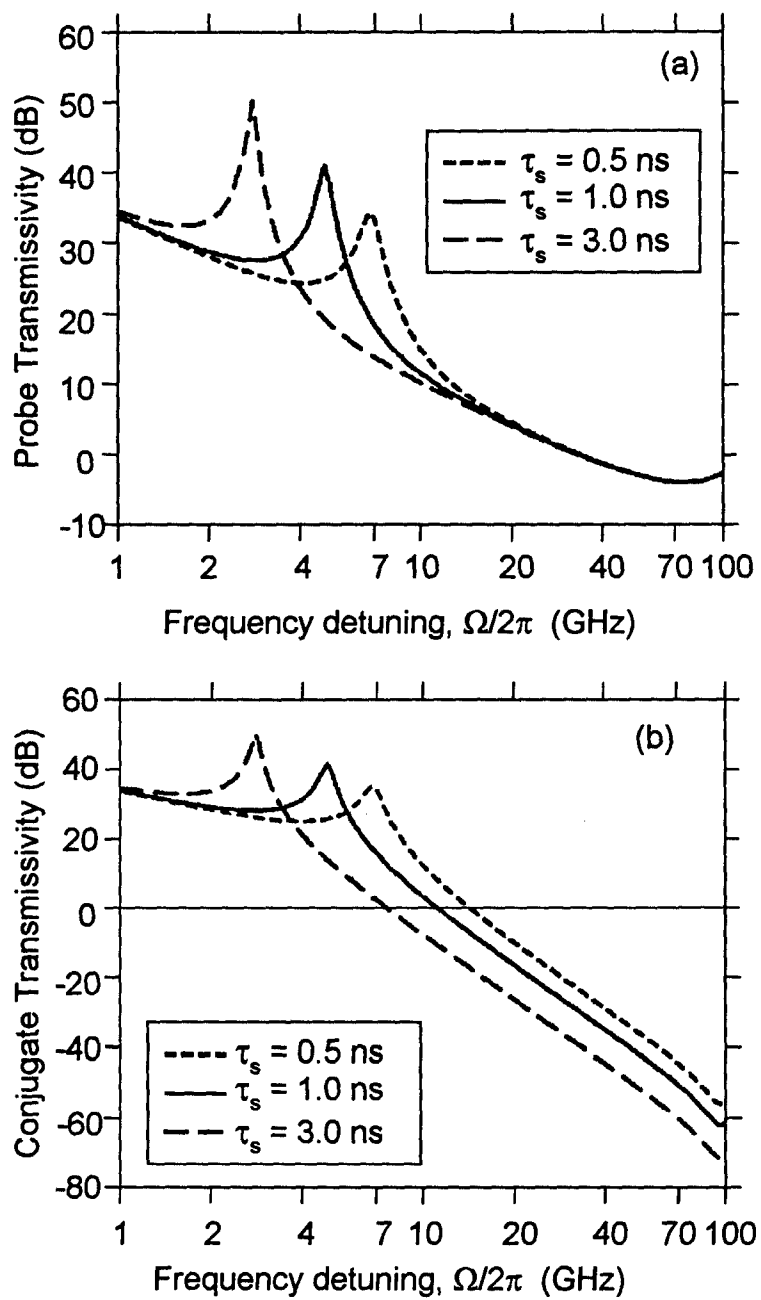


Figure 14. Published Probe and Conjugate Transmittivity vs. Pump-Probe Detuning for Various Lifetimes. (a) shows probe and (b) shows conjugate.

Second, the model was tested by contriving a test case with an analytic solution. To obtain an analytic solution, the differential equations (44-46) must have coefficients independent of z . Since the coefficients depend on z through the pump fields and

saturated gain, we seek a case with constant pump fields. For a laser cavity with highly reflective mirrors, the self-generated pump *intensity* is nearly constant throughout the cavity. By setting the linewidth enhancement factor (β) to zero, the phase change is eliminated and so the pump *field* is also constant. With nearly constant field, the pump fields can be found merely by noting that in an operating laser, gain equals loss. With the constant pump field established, the differential equations for the probe and conjugate fields can be solved analytically. The analytic solution is described in detail in Appendix B, by use of a MathCad 5.0+® worksheet. The numerical model results and analytic solution are nearly identical for the test case, as shown in Figure 15.

Further validation of the model by comparison to experiment was demonstrated by Yee and Shore in their article. (Yee, 1994a) Typical experimentally-measured features of probe and conjugate reflectivity are: a peak at the relaxation oscillation frequency which is proportional to pump power, an exponential decrease with pump-probe detuning, probe spectral asymmetry, and a dramatic enhancement when pump-probe detuning equals cavity mode spacing. All these features are shown in the asymmetric cavity model, unlike earlier variants on the Agrawal population pulsation model.

These three levels of validation boost confidence in the ability of the asymmetric cavity model to describe FWM in self-pumped semiconductor lasers. The ability of the modified model to handle a wider variety of cases (externally generated pump and below threshold operation) will be shown in the discussion of results.

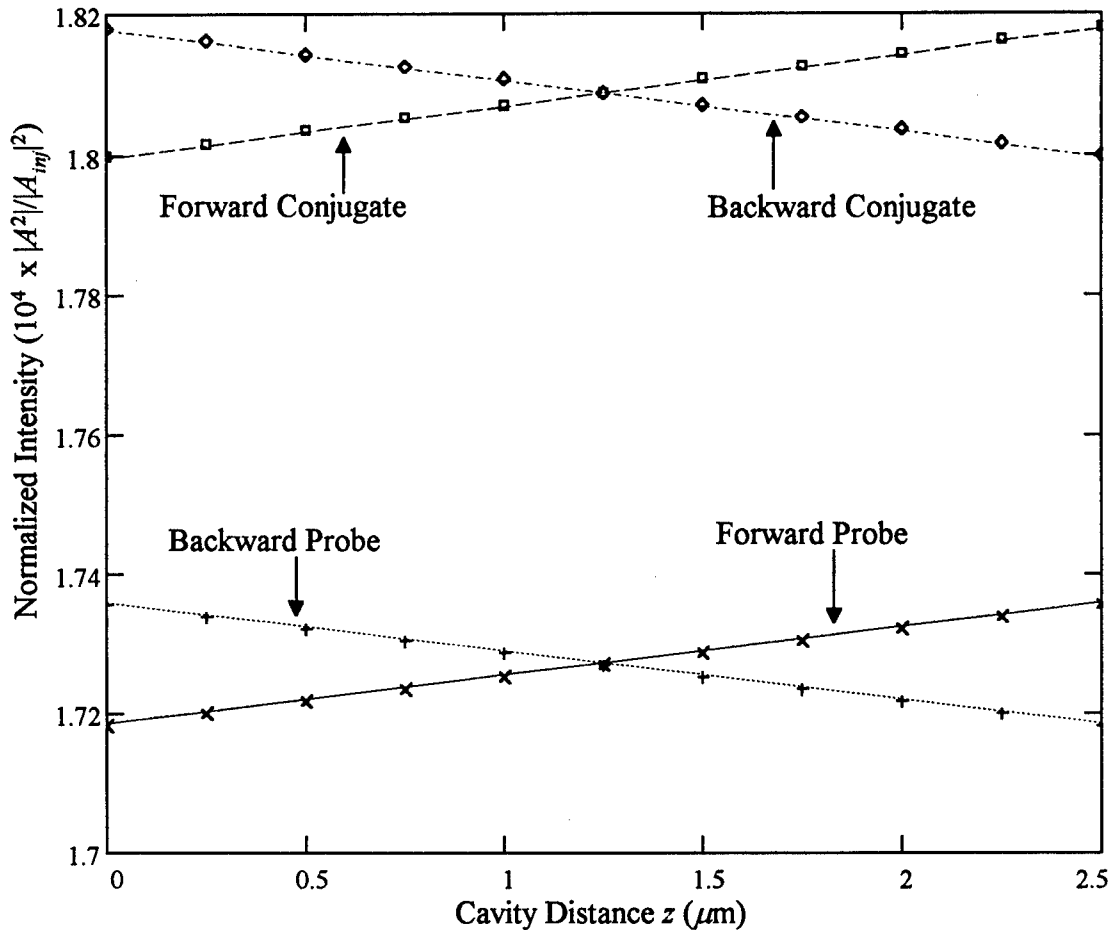


Figure 15. Probe and Conjugate Field Intensity in a Cavity. Results of the asymmetric cavity model are shown as points, while the analytic solutions are shown as lines.

3.2.2. *Lumped Oscillator Model*

Another modeling approach was developed by Simpson and Liu in a series of articles investigating nonlinear dynamics in semiconductor lasers. (Simpson, 1991; Simpson, 1995a/b; Simpson, 1996a; Liu, 1993; Liu, 1994) Although not as applicable to these experiments as the model of Yee and Shore, it has the advantage of a simple closed form solution. In one particular article (Simpson, 1996a) they adapt their model to a VCSEL with a strong injection locking pump wave, which is one part of the regime

studied in this dissertation. Their model is a time domain model, lumping all the spatial variation of the fields into one big average. For short cavity VCSELs, this is a very good assumption, and the model can explain much of the dynamics. However, it does not lend itself to the investigation of cavity balancing or behavior significantly below threshold. (Simpson, 1996b)

The lumped oscillator model assumes the VCSEL can be described by the average of the electric field amplitude in the cavity. The interaction between the gain medium and the electric field is then described by two differential equations.

$$\frac{dA}{dt} = -\frac{\gamma_c}{2}A + i(\omega_L - \omega_c)A + \frac{\Gamma}{2}(1 - i\beta)gA + \eta(A_I + A_{inj}e^{-i\Omega t}) \quad (58)$$

$$\frac{dN}{dt} = \frac{J}{ed} - \gamma_s N - \frac{2\epsilon_0 n^2}{\hbar\omega_L} g|A|^2 \quad (59)$$

where A represents the total complex field amplitude in the cavity at the locked frequency ω_L . The bare cavity frequency is ω_c , γ_c is the cavity decay rate in sec^{-1} , Γ is the field confinement factor, β is the linewidth enhancement factor, g is the gain coefficient in sec^{-1} , A_I is the amplitude of the injection locking (pump) signal and A_{inj} is the weak probe signal at $\omega_L + \Omega$. The coupling rate η is the fraction of injected signal that makes it into the cavity times the round trip time in the cavity. (van Tartwijk, 1995) The carrier density is N , J is the injection current density, e is the electronic charge, d is the active region layer thickness, γ_s is the spontaneous carrier decay rate and the inverse of carrier lifetime (τ^{-1}), and n is the refractive index of the gain medium.

The solutions for A and N are assumed to be the steady state solutions with small fluctuations at the frequency Ω , and the gain dependence on field and carrier density is assumed to be small and linearized about the operating point. These assumptions are written as

$$\begin{aligned}
A &= A_L + A_r e^{-i\Omega t} + A_f e^{i\Omega t} \\
N &= \bar{N} + N_1 e^{-i\Omega t} + N_1^* e^{i\Omega t} \\
g(N, S) &= g(\bar{N}, \bar{S}) + \frac{\partial g}{\partial N} \bigg|_{\bar{N}, \bar{S}} (N - \bar{N}) + \frac{\partial g}{\partial S} \bigg|_{\bar{N}, \bar{S}} (S - \bar{S}) \\
&= g_0 + g_n(N - \bar{N}) + g_p(S - \bar{S})
\end{aligned} \tag{60}$$

with A_1 the amplified probe, A_2 the four-wave mixing conjugate signal, A_L the locked steady state field, S the photon number (properly normalized intensity $|A|^2$), and the rest of the quantities defined as shown in equation (60).

First the equations are solved in steady state, with no injected probe, for both the bare laser and the locked laser. With no injection locking signal, this is a simple matter. With the injection locking signal, an additional equation relating the phase, frequency, and amplitude of the locking signal and locked signal must be introduced.

$$\begin{aligned}
\omega_L - \omega_0 &= \beta\delta / 2 - \beta U + V \\
U &= \eta |A_l / A_L| \cos \phi_L \\
V &= \eta |A_l / A_L| \sin \phi_L
\end{aligned} \tag{61}$$

where $\delta = \gamma_c - \Gamma g_0$, the gain deficit of the free running laser before injection and ϕ_L is the relative phase of the free running and locked fields. If the laser is above threshold before injection, $\delta=0$. By solving the equations with and without the injected term, the relationship between the injection field (A_l), bare laser field (A_0), and locked field (A_L) can be derived. In general, this involved a third order polynomial which was solved numerically. A plot of $|A_L|^2$ as a function of $|A_0|^2$ and $|A_l|^2$ for typical values of the other parameters is shown in Figure 16.

Once the steady state solution was found, the dynamic solution can be obtained. The full dynamic expressions for N and A are substituted into equations (58) and (59), and using orthogonality of the complex exponentials, terms oscillating at $+\Omega$ and $-\Omega$ are grouped separately and the equations solved. Terms oscillating at higher multiples of Ω

are ignored, as are terms involving higher order products of N_1 , A_1 , or A_2 , which are small compared to the steady state values \bar{N} and A_L .

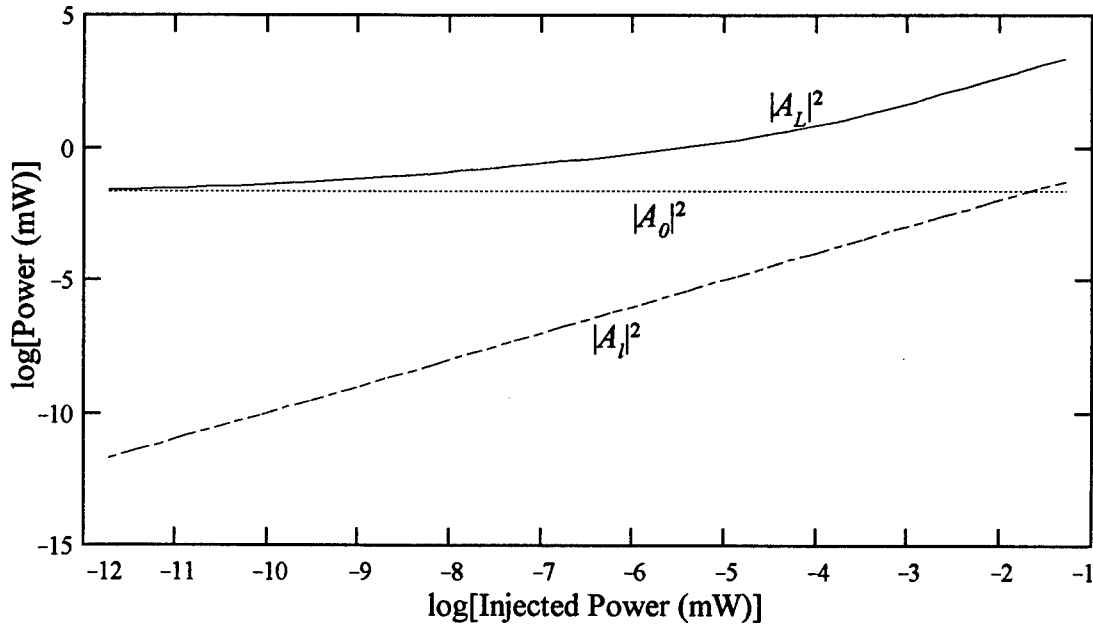


Figure 16. Injected Locked Field Intensity vs. Free Running Intensity and Injected Field Intensity.

After considerable algebra, expressions for R_c and R_p can be written in terms of the defined parameters and two new parameters,

$$\begin{aligned}\gamma_{nL} &= \frac{2n^2 \epsilon_0}{\hbar \omega_L} |A_L|^2 g_n \\ \gamma_{pL} &= -\frac{2n^2 \epsilon_0}{\hbar \omega_L} |A_L|^2 \Gamma g_p\end{aligned}\tag{62}$$

which are just scaled versions of the derivatives of gain with respect to carriers and photons at the operating point. The expressions are

$$R_p = \left| \frac{\eta}{D} \left\{ (\gamma_s + \gamma_{nL} - i\Omega) [U - i(\Omega - V)] + \frac{1}{2} (1 + i\beta) (\gamma_c \gamma_{nL} + \gamma_s \gamma_{pL} - 2U \gamma_{nL} - i\Omega \gamma_{pL}) \right\} \right|^2 \quad (63)$$

$$R_c = \left| \frac{\eta}{D^*} \left\{ \frac{1}{2} (1 - i\beta) (\gamma_c \gamma_{nL} + \gamma_s \gamma_{pL} - 2U \gamma_{nL} + i\Omega \gamma_{pL}) \right\} \right|^2 \quad (64)$$

where

$$D = (\gamma_s + \gamma_{nL} - i\Omega) [(U - i\Omega)(U + \gamma_{pL} - i\Omega) + V(V + \beta \gamma_{pL})] + (U + \beta V)(\gamma_c - 2U - \gamma_{pL}) \gamma_{nL}.$$

These have the merit of being closed-form solutions that efficiently show the detuning dependence of R_c and R_p . It is for this purpose that the model was used.

Both models suffer from one fundamental assumption which is probably good for lasers above threshold but not below threshold. The assumption is that β , the linewidth enhancement factor, is a constant. This "constant" is defined by the relative rates of change with carrier density of the real and imaginary parts of the susceptibility (see equation (17)) and typically has values of 2-6 in the experimental literature for lasers above threshold. But as pointed out in the definitive document on the linewidth enhancement factor (Osinski, 1987), for low carrier densities one can achieve $\beta=0$. In fact, β depends heavily on carrier density and optical energy relative to bandgap. This variation is not a problem in lasers above threshold, where carrier density is essentially clamped at the threshold value by the strong field, regardless of injection current. But in experiments below threshold with a wide variety of currents and injected powers, β is almost surely not a constant. Nevertheless, without good data for β , it's probably better to treat it as constant than try to guess a functional form.

4. Results and Analysis

The experiments were performed on two different types of devices: VCSELs and RCLEDs. The two device types were very similar, operating with peak emission between 840 and 850 nm, using GaAs quantum wells as a gain medium and different $\text{Al}_x\text{Ga}_{1-x}\text{As}$ layers to make the mirrors and buffers. A RCLED is simply a VCSEL with fewer DBR layers on the mirrors, making them less reflective. The mirror losses are greater than the gain, so a RCLED never lases. But it emits highly enhanced, spectrally narrow spontaneous emission, and is usually cheaper and easier to grow than a VCSEL. In the context of this work, the RCLED is a highly unbalanced cavity. Since $R_1 < R_2$, it takes absorption (negative gain) to balance the cavity, which occurs at zero or low current.

4.1. RCLED Results

4.1.1. Device Information

Before describing the results of four-wave mixing experiments, some basic description of the device is necessary. The resonant cavity light emitting diode (RCLED) used in this experiment was designed at AFIT and grown and fabricated at the University of New Mexico (UNM) in 1994 for another AFIT student, and his thesis contains a complete description of the device design. (Fitzgerald, 1994) The cavity has a lower mirror consisting of 38.5 pairs of graded quarter wave layers of AlAs and $\text{Al}_{0.15}\text{Ga}_{0.85}\text{As}$, giving a calculated reflectivity of about 0.98. The top mirror has 6 pairs of quarter wave layers with a calculated reflectivity of about 0.8. The central region contains 4 GaAs quantum wells, 8 nm wide, separated by 10 nm buffer layers of $\text{Al}_{0.15}\text{Ga}_{0.85}\text{As}$ centered in the optical cavity. The region between the wells and mirrors is linearly graded in index to reduce ohmic heating, as are the interfaces between mirror layers. Table 2 records the growth layers in the RCLED.

Table 2. Growth Layer Description for UNM RCLED.

	Layer Composition	Doping (cm ⁻³)	Thickness (nm)	Function
Top Mirror	GaAs	p ~10 ¹⁹	20.0	Cap Layer
	Al _{0.15} Ga _{0.85} As	p ~10 ¹⁸	49.8	Mirror High Index
	Al _x Ga _{1-x} As (x=0.15⇒1.0)	p ~10 ¹⁸	12.0	Graded Index
	AlAs	p ~10 ¹⁸	58.6	Mirror Low Index
	Al _x Ga _{1-x} As (x=1.0⇒0.15)	p ~10 ¹⁸	12.0	Graded Index
	Al _{0.15} Ga _{0.85} As	p ~10 ¹⁸	49.8	Mirror High Index
	Al _x Ga _{1-x} As (x=0.15⇒1.0)	p ~10 ¹⁸	12.0	Graded Index
Cavity	AlAs	p ~10 ¹⁸	58.6	Mirror Low Index
	Al _x Ga _{1-x} As (x=1.0⇒0.15)	undoped	85.8	Graded Index
	Al _{0.15} Ga _{0.85} As	undoped	10.0	Buffer
	GaAs	undoped	8.0	Quantum Well
	Al _{0.15} Ga _{0.85} As	undoped	10.0	Buffer
Bottom Mirror	Al _x Ga _{1-x} As (x=0.15⇒1.0)	undoped	85.8	Graded Index
	AlAs	n ~10 ¹⁸	58.6	Mirror Low Index
	Al _x Ga _{1-x} As (x=1.0⇒0.15)	n ~10 ¹⁸	12.0	Graded Index
	Al _{0.15} Ga _{0.85} As	n ~10 ¹⁸	49.8	Mirror High Index
	Al _x Ga _{1-x} As (x=0.15⇒1.0)	n ~10 ¹⁸	12.0	Graded Index
	AlAs	n ~10 ¹⁸	58.6	Mirror Low Index
	Al _x Ga _{1-x} As (x=1.0⇒0.15)	n ~10 ¹⁸	14.0	Graded Index
	GaAs	n ~10 ¹⁸	500.0	Smoothing Layer

The devices are defined by gold contacts on the top mirror measuring 180 μm x 90 μm , with a circular aperture to allow light out. Aperture diameter ranged from 5 μm to 50 μm . There was no mesa etching of these devices. The RCLEDs were designed to operate at 842 nm, with quantum well band edge at about 860 nm. The operating wavelengths of the devices ranged from 839 nm to 846 nm, due to nonuniform layer thickness across the wafer.

Spectral reflectivity was measured using both a broadband white light and a tunable diode laser. The white light was focused onto the sample and the reflected signal sent to the spectrometer/OMA. The tunable diode was simply tuned to a number of

wavelengths and reflectivity measured with a power meter. The results are shown in Figure 17. Both show a broad, deep dip in the reflectivity at the cavity mode. The discrepancy in the wavelength at which the minimum occurs is due to the white light being focused onto the surface at a wide variety of angles (0° to 15°). For each angle, a different wavelength is resonant, with shorter wavelengths for larger angles. Thus, the minimum measured by the white light is shifted to shorter wavelengths than the measurement by the narrow (spectrally and spatially) tunable laser.

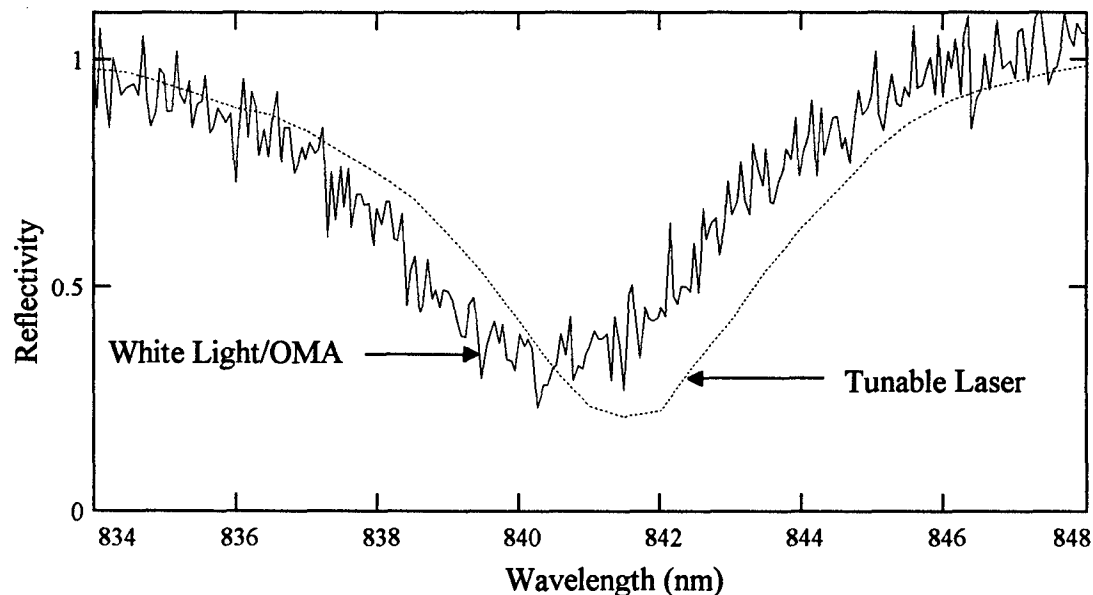


Figure 17. Spectral Reflectivity of RCLED.

Because the cavity has only a single mode in the spectral width of the gain material, there is considerable narrowing of the spontaneous emission into the cavity mode. But the cavity has fairly low finesse, making the cavity mode spectrally broad compared to most cavities. Figure 18 shows a typical spectral output of the RCLED, with a spectral full width at half maximum of about 5 nm. That is narrow compared to a conventional LED but broad compared to a laser. Note the spectral mismatch in Figure

18a between the peak of the emission and the dip in the reflectivity as measured by the tunable diode laser, for the same reason as Figure 17. Figure 18b shows as current increases, the spontaneous emission shifts to slightly shorter wavelengths at 50 mA, probably due to the blue shift of band edge with carrier density or the negative shift in index with carrier density. (Park, 1988) With higher current the peak shifts to longer wavelengths as the device heats up, which increases both index and cavity length. Beyond 150 mA, the total emission stops increasing as heat decreases the efficiency of emission.

The total optical power out of the RCLED varies linearly with the current at low currents. Figure 19 shows a typical plot of optical power versus current into the device. Note that since the light aperture is a small fraction of the total device, and there is no carrier confinement so current flows through the whole device, the currents are quite high to achieve modest output powers. These devices were built for science, not efficiency.

4.1.2. Pump-Probe Detuning

The conjugate reflectivity (R_c) as a function of pump-probe detuning should depend on the speed of mechanisms involved in the FWM. Since this type of FWM relies on interband transitions of the carriers, one would think carrier lifetime would determine the frequency/speed characteristics of FWM. Results showed that carrier lifetime is only a part of the process.

Predictions from the asymmetric cavity model show a decay of R_c with detuning which depends on the pump power. Figure 20a shows the model predictions for a carrier lifetime of 1 ns. Exponential curves are fit to the model predictions as a simple way to describe the decay behavior. There is no physical reason to choose an exponential over other forms of decay; it's just a simple descriptive tool. For low pump powers, the decay is faster than an exponential. As power increases, the decay looks more like an exponential but with a changing slope. Figure 20b shows the decay coefficients of the fitted exponentials as a function of pump power.

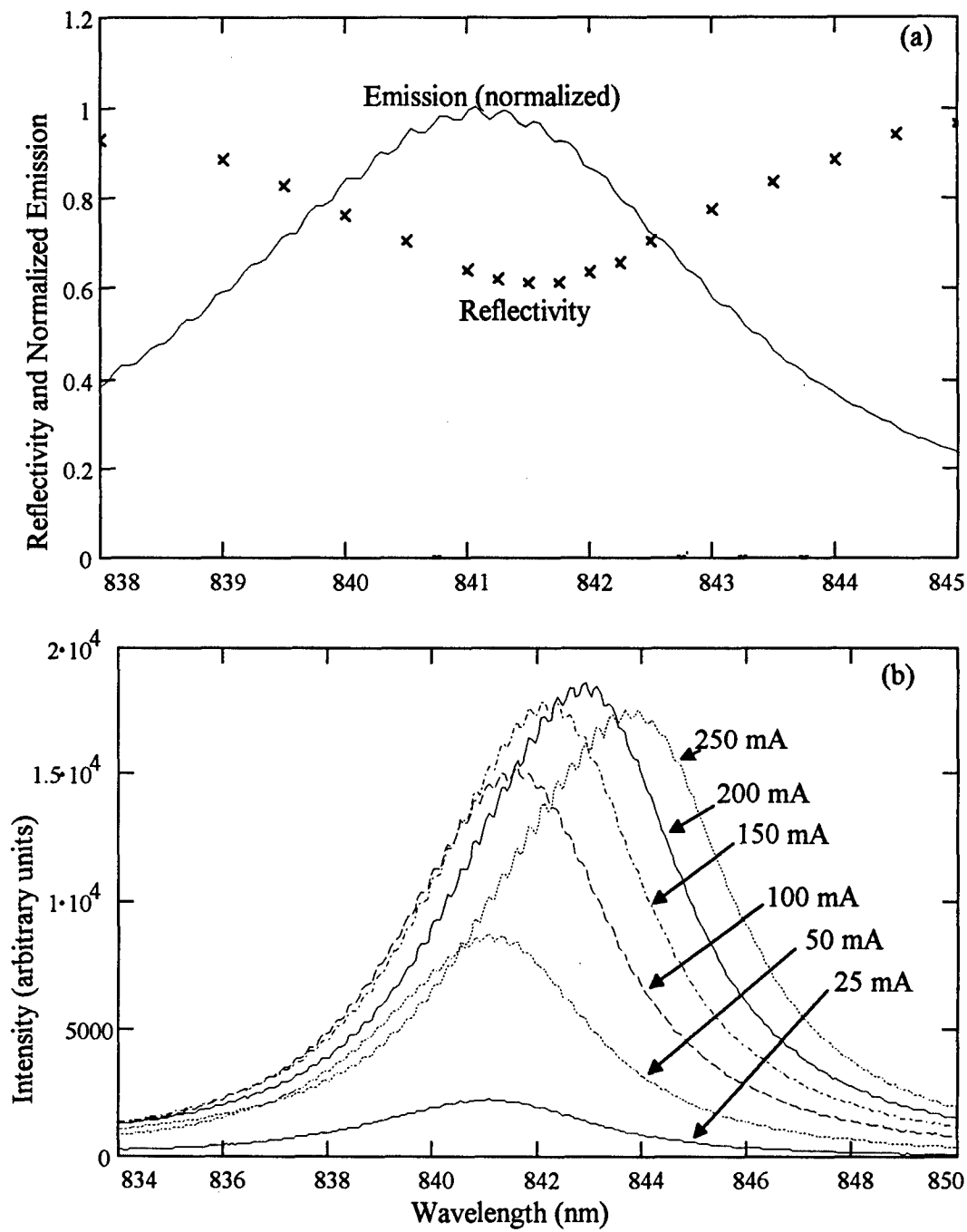


Figure 18. Spectral Measurement of Light from a RCLED. Plot (a) shows spontaneous emission and spectral reflectivity (measured with tunable laser) of the RCLED at 50 mA. Plot (b) shows spontaneous emission for a variety of currents.

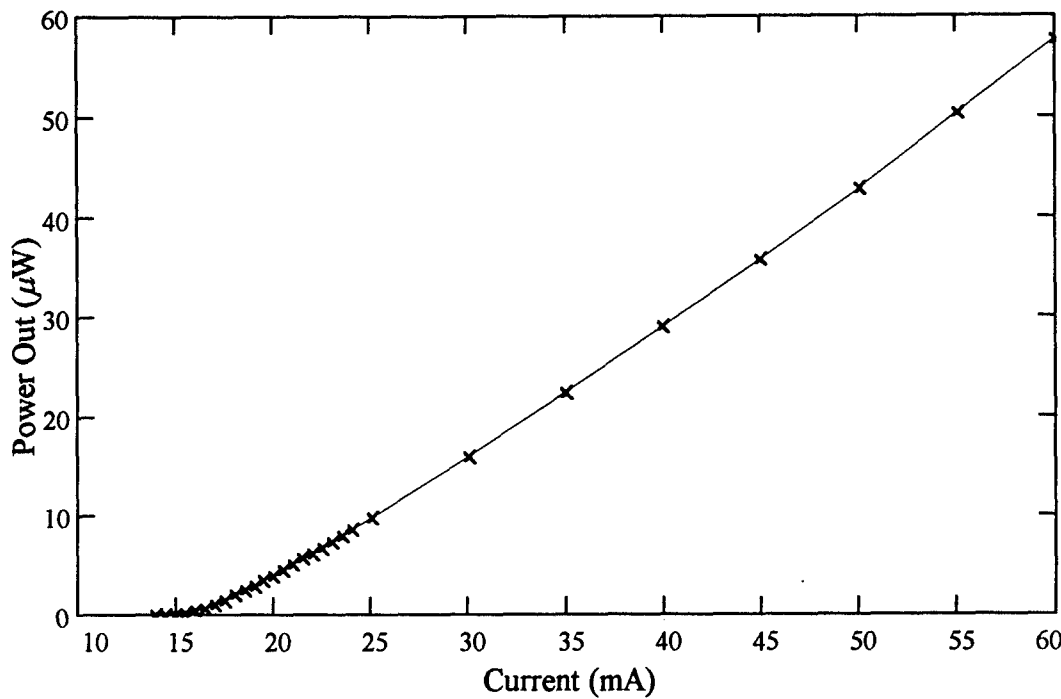


Figure 19. Light vs. Current for RCLED.

Experimental results show similar decay, depicted in Figure 21 for a variety of pump powers. The decay looks more nearly exponential than the model predictions, particularly at low pump powers.

The dependence of FWM decay rate (as estimated by the exponential decay coefficient) on pump power is shown in Figure 22. The decay coefficients are around 1 ns. But the coefficients increase with increasing pump power, the opposite to the model predictions.

The rough correlation of decay rates (1 ns) shown by model and experiment is very encouraging. The difference between model and experiment in predicting the dependence on pump power is a curious trend. The discrepancy may be due to the rate equation approximation used in the model. Equation (18) models the carrier decay as a simple N/τ dependence. Carrier recombination is due to a variety of mechanisms, radiative and non-radiative, which in general do not depend linearly on N . (Chow, 1994: 29) This

approximation is probably good for a laser above threshold with very high carrier densities, where the conduction band is quite full and the carrier density saturates at the point where gain equals loss, reducing the amount of variation in N . At low carrier densities, the nonlinear dependence of lifetime on carrier density is more pronounced, and may account for the mismatch between experiment and model.

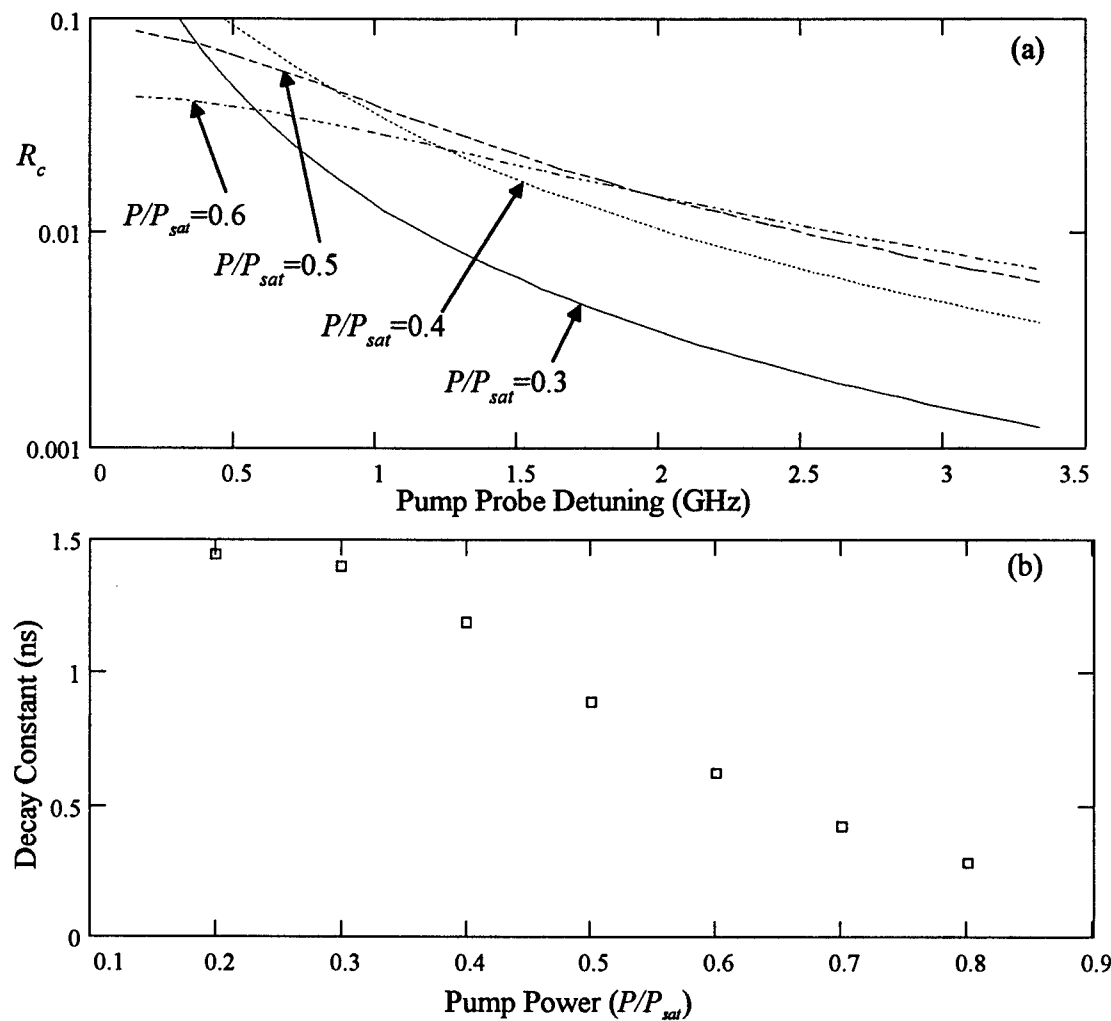


Figure 20. Model Predictions of Conjugate Reflectivity vs. Pump-Probe Detuning for Various Pump Powers. Part (a) shows the model predictions and part (b) shows the decay coefficients of exponential fits to the pump power data. Injection current is 0.

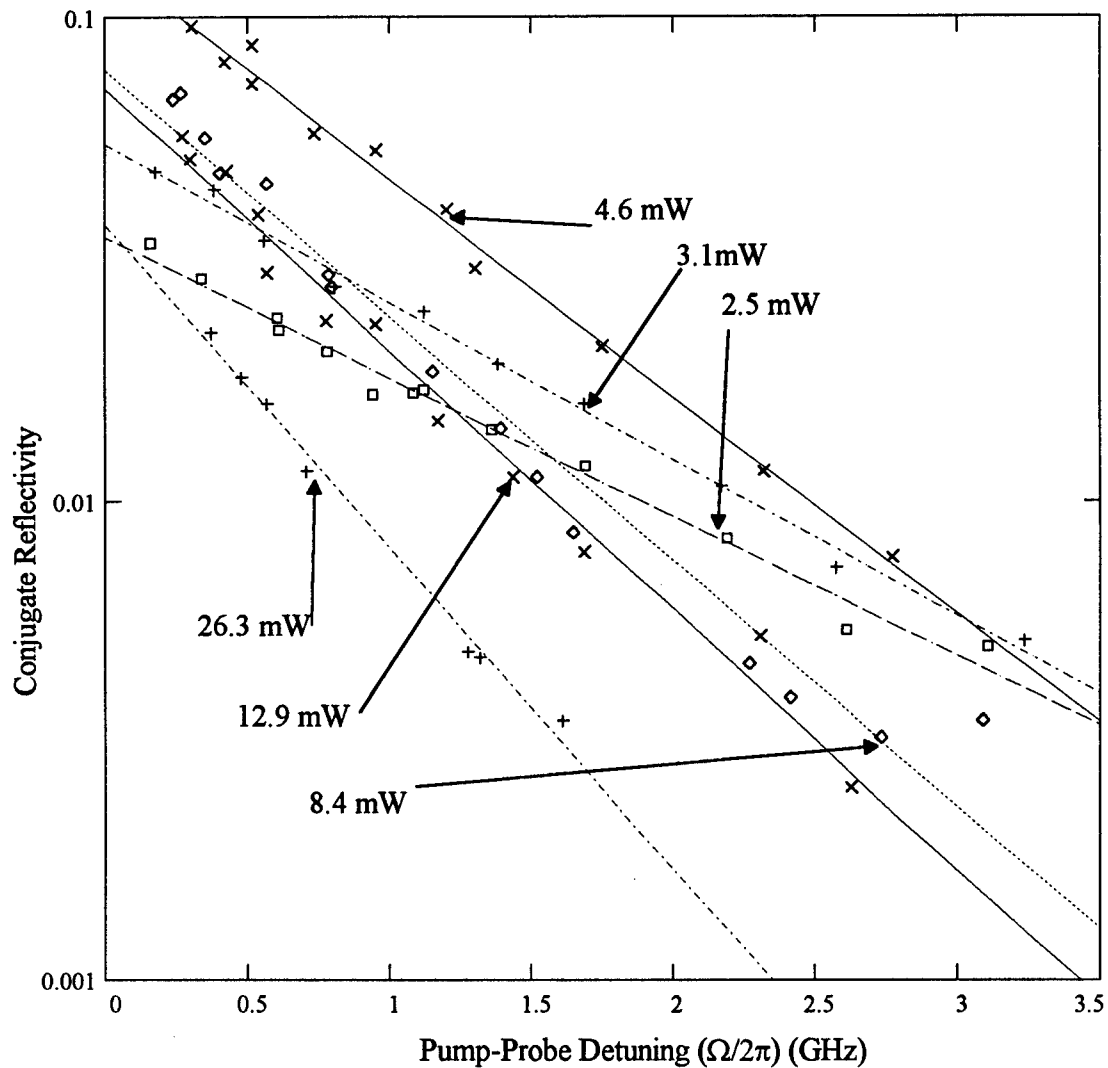


Figure 21. Measured Conjugate Reflectivity in RCLED vs. Pump-Probe Detuning for Various Pump Powers. The markers show experimental data, and lines are exponential fits to the data. Injection current is 0.

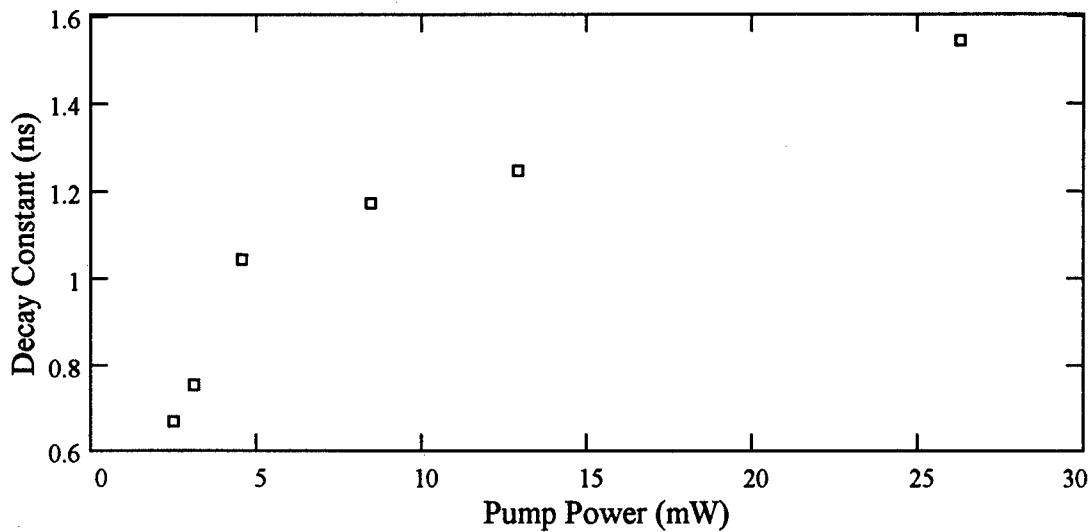


Figure 22. Decay Coefficient vs. Pump Power.

In addition, parameters other than carrier lifetime clearly play a role. The model was run with a variety of carrier lifetimes. While the FWM decay coefficient (as estimated by an exponential fit) did increase with carrier lifetime, it was not a simple linear relationship.

4.1.3. Pump Power and Bias Current

The dependence of R_c on pump power and bias current is the most complex issue in the study of FWM in RCLEDs. The effects of pump and current are interrelated. Both are sources of carriers, though very different sources. Before discussing specific RCLED results, some general trends of FWM with bias current will be discussed.

Results of model calculations for three hypothetical devices are shown in Figure 23. The three devices differ only in their mirrors. The product $R_1R_2=0.72$ is the same for all three, but the balance of the two mirrors is different. The current density (J) is normalized to the transparency current density (J_0). In all three cases R_c is minimum at the transparency point ($J/J_0=1$) because if gain is zero, χ is also zero and no mixing occurs. For negative gain ($J/J_0 < 1$) R_c has a local maximum, while for positive gain

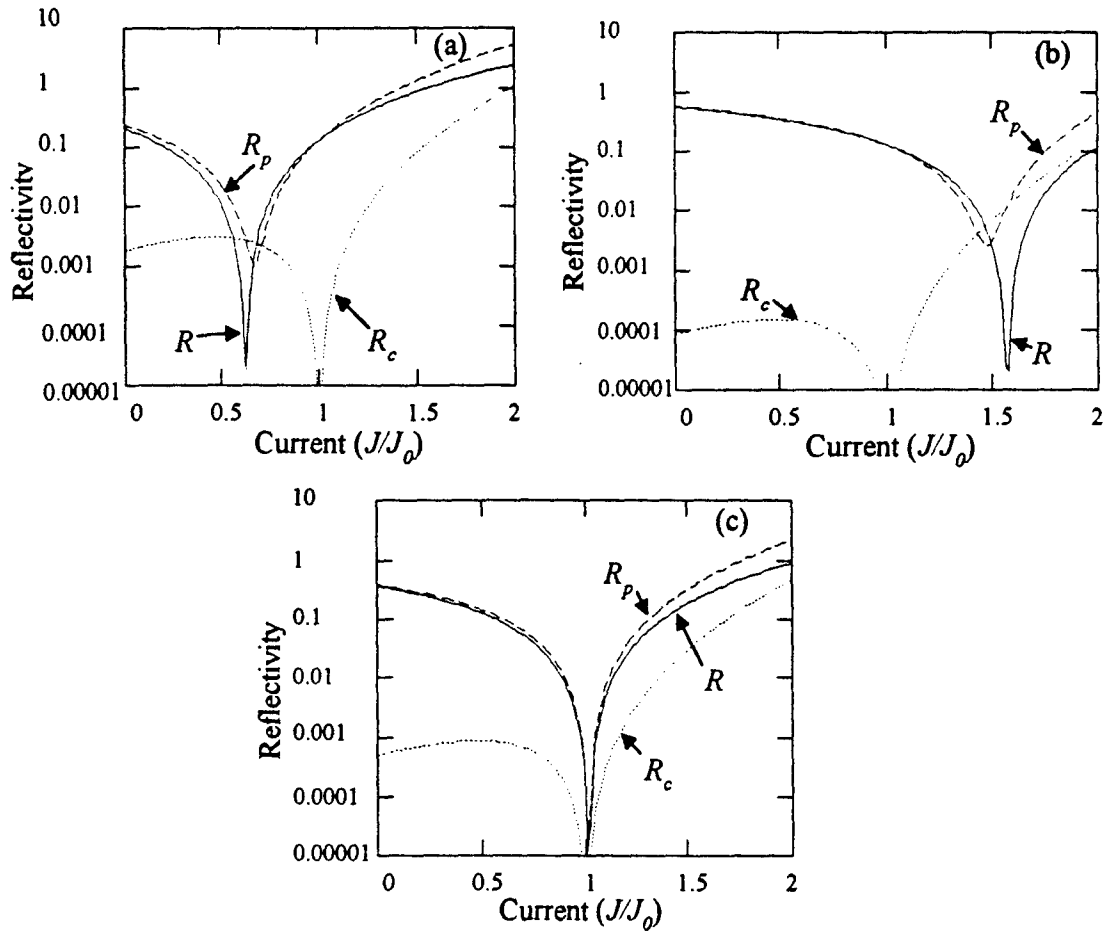


Figure 23. Calculated Pump, Probe, and Conjugate Reflectivities vs. Bias Current for Three Hypothetical Cavities. Part (a) is for $R_1=0.8$, $R_2=0.9$, (b) is for $R_1=0.9$, $R_2=0.8$, (c) is for $R_1=0.85$, $R_2=0.85$. Pump power is 0.1 of saturation power.

$(J/J_0 > 1)$, R_c simply increases with current. The local maximum in the negative gain (absorption) region is due to trade-off between wanting large absorption to maximize the value of $|\chi|$ for creating a conjugate wave, and the drawback that with large absorption the conjugate wave (and all other waves) will be re-absorbed. For positive gain, there is no trade-off: the more gain the better. Note that R_p and R behave differently than R_c , and have minima at the cavity balance point, not the transparency point. The balance point is at negative gain for case (a) and positive gain for case (b) earlier. In case (c) with two

equal mirrors, the balance point and transparency point coincide. These general trends are useful when analyzing measurements from a real device.

Returning to the RCLED, the asymmetric model predictions for conjugate reflectivity as a function of pump power and current are shown in Figure 24. Parts (a) and (b) show the same data plotted two different ways for clarity. The pump power (P) is normalized to the saturation power (P_{sat}). The region with negative gain ($J/J_0 < 1$) has a local maximum for R_c and the current at which the maximum occurs moves lower as pump power increases. The shift of the maximum is because higher pump powers saturate the negative gain, and to achieve the same saturated negative gain the initial negative gain must be larger in magnitude, which means less current. As current increases, gain moves to the transparency point and R_c goes down, reaching zero at the point where gain is zero. The model also predicts that at large pump powers, R_c is reduced by saturation of the gain/absorption.

The experimentally measured power and current dependence of R_c is shown in Figure 25. In most respects, it matches the model predictions very closely. For lower pump powers, there is an optimum current for which R_c is a maximum. As pump power increases, the optimum current decreases all the way to zero, and with further increase of pump power, R_c decreases due to saturation. As the current becomes large enough to move the absorption toward zero, R_c goes to zero.

There is one difference between the model and experiment. The model predicts that when current increases beyond transparency, R_c should increase again, as shown in Figure 23. The experimental data shows no increase. In fact, attempts were made to measure R_c at currents as high as 200 mA without success.

To explain this mismatch, the gain of the cavity was probed through a series of reflectivity (R) measurements. This is an indirect and imprecise way to measure gain, but the only way available. The reflectivity at mode center is the quantity of interest, so a single laser was injected and the reflectivity measured. The total R depends on the

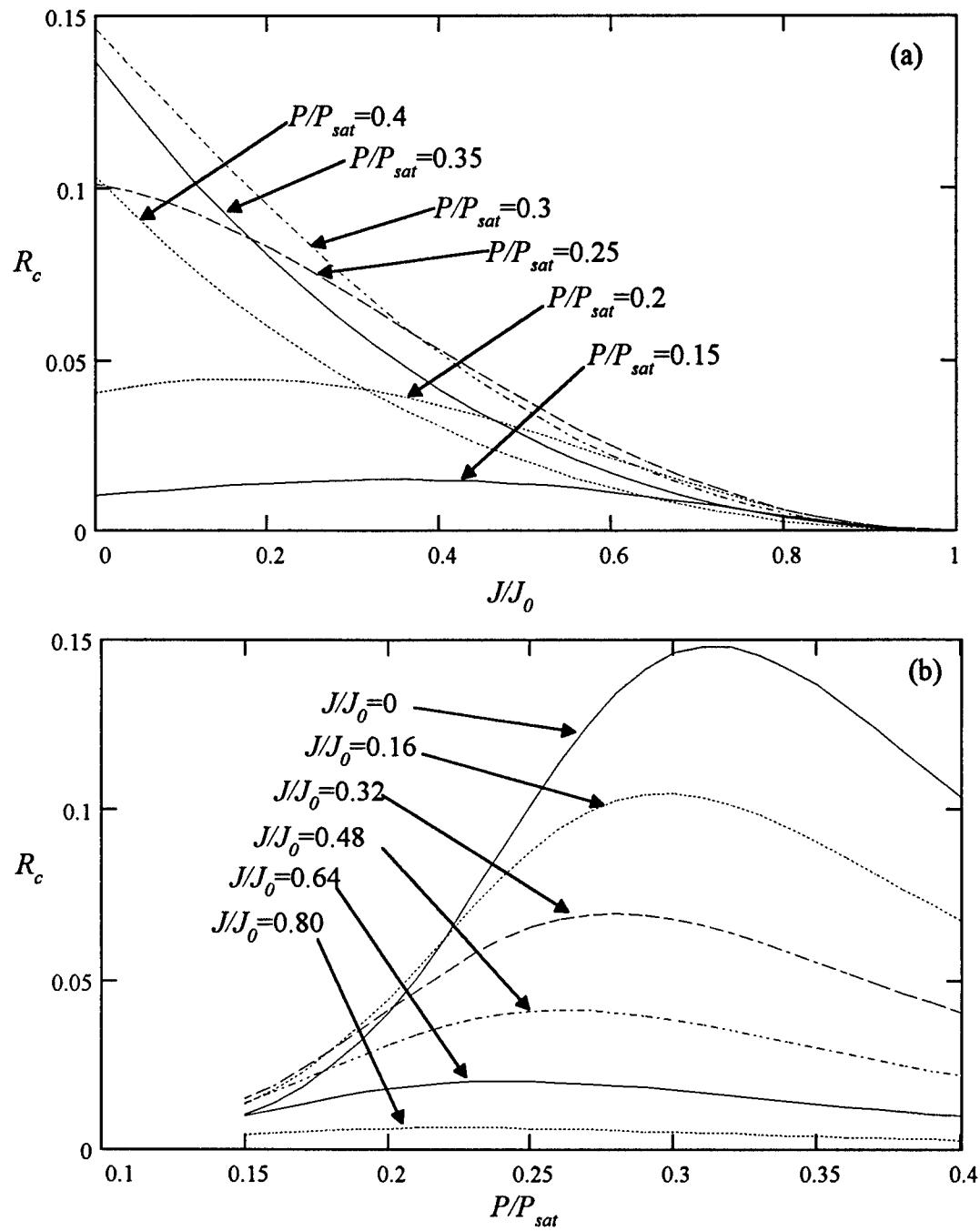


Figure 24. Model Predictions of R_c vs. Current for Different Pump Powers. Plot (a) shows current on the horizontal axis, and plot (b) shows the same data with pump power on the horizontal axis.

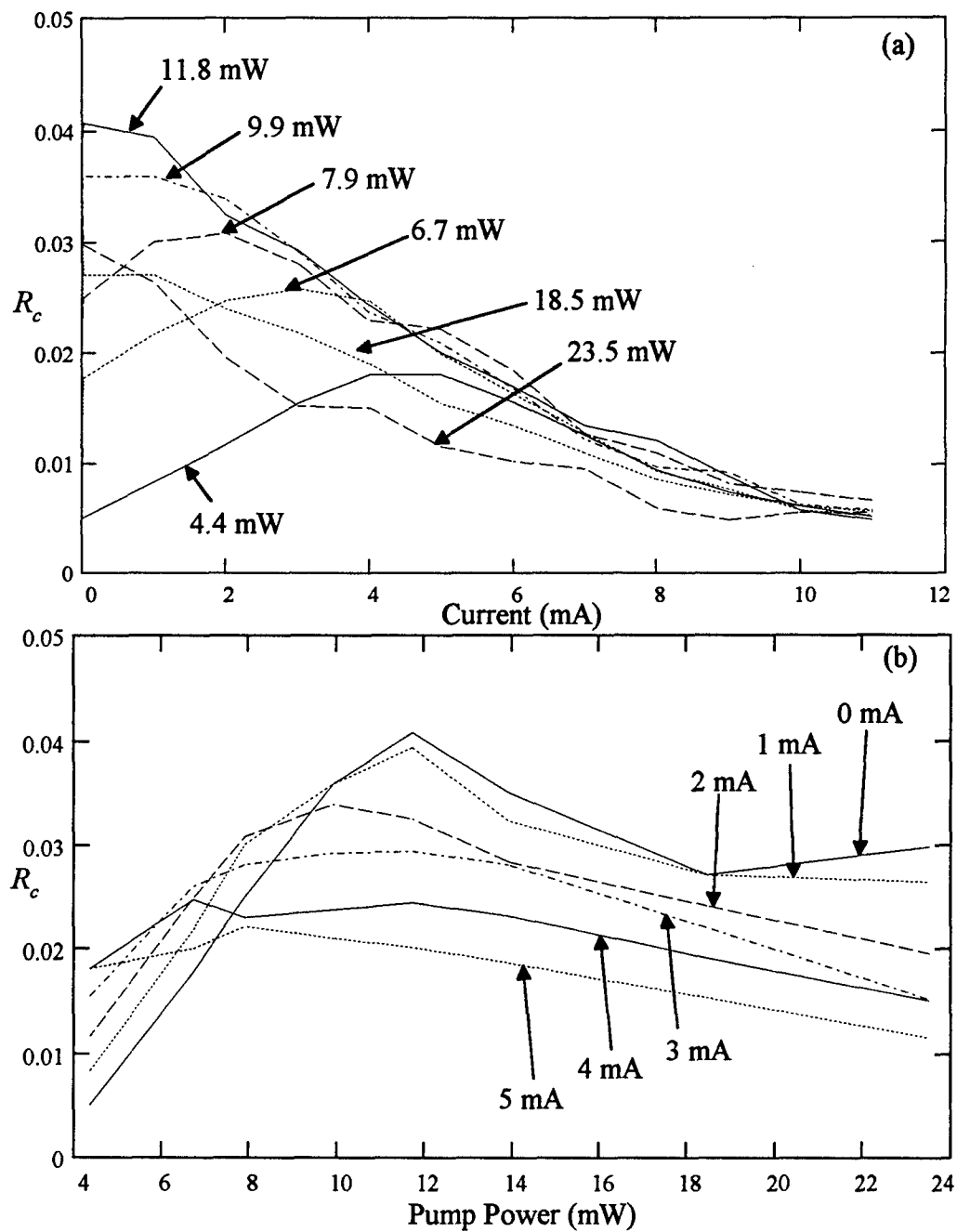


Figure 25. Conjugate Reflectivity vs. Pump Power and Injection Current. Plot (a) shows current on the horizontal axis, and plot (b) shows same data with pump power on the horizontal axis.

reflectivity of the two mirrors and value of gain/absorption, as shown in equation (22). In turn, the gain depends on current and the injected field, which can saturate the gain.

Model predictions of this reflectivity are shown in Figure 26 for the same ranges of current and pump power as the R_c data. The reflectivity reaches a minimum at the cavity balance point. This point moves with pump power because of gain saturation by the pump field. For high pump powers, the absorption is reduced and the balance point moves to a lower current, representing a larger unsaturated absorption. As current moves the absorption toward transparency, all the pump powers see the same value of reflectivity, about 0.8. Pump power becomes unimportant because a gain of zero cannot be saturated, regardless of pump power.

Experimentally, the pump laser was tuned to the mode center and used for a series of reflectivity measurements with varying pump power and current injection. As current increased the device heated, shifting the cavity resonance to longer wavelengths. Careful analysis showed that the center wavelength of the spontaneous emission was a good indicator of temperature in the cavity's active region, so as current increased the center wavelength, the thermoelectric cooler was adjusted to cool the sample until the center wavelength was back to the original wavelength. In this way, the measurements at different currents should all be for the same cavity temperature and the same absolute wavelength. The results are in Figure 27.

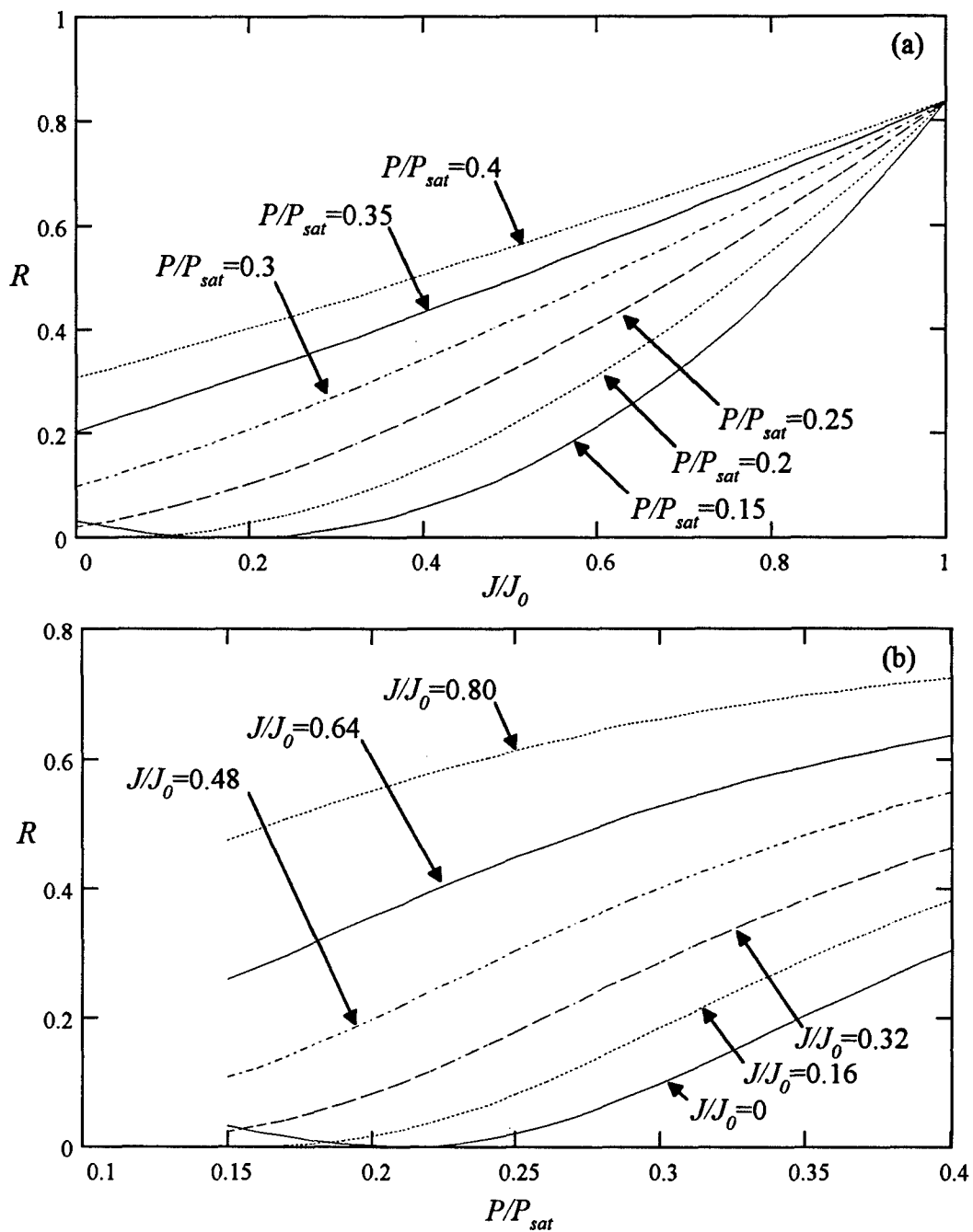


Figure 26. Model of RCLED Reflectivity vs. Current and Injected Power. Plot (a) shows current on the horizontal axis, and plot (b) shows the same data with pump power on the horizontal axis.

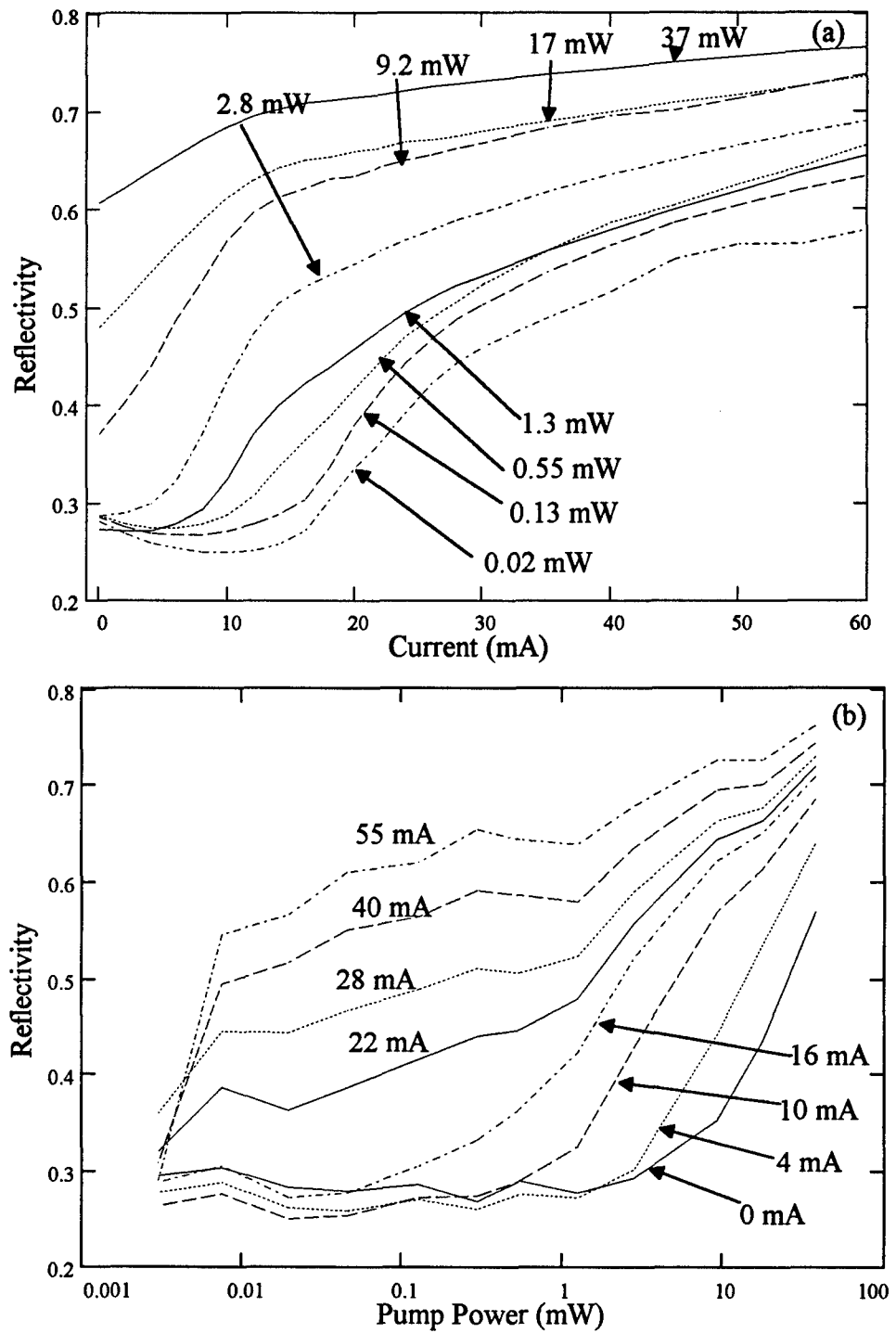


Figure 27. Measured Mode-Center Reflectivity of RCLED vs. Current and Pump Power. Plot (a) shows current on the horizontal axis, and plot (b) shows the same data with pump power on the horizontal axis. Cavity temperature was maintained at $T=23^{\circ}\text{C}$.

The experimental results and model match in many fundamental ways. The current producing minimum reflectivity (cavity balance point) moves to smaller currents as the injected power increases, just as the model predicts. The experimental minimum reflectivity is about 0.2, not zero. There are a number of possible reasons for this. First, the cavity is not perfect. Scattering can occur from the top surface of the device as well as defects within the multi-layered growth. Unlike the model assumption, the injected beam is not a perfect plane wave, but a focused Gaussian beam. A fraction of the field may not be well coupled to the cavity and get reflected. The carriers are not injected uniformly in the RCLED aperture, either, and so different parts of the beam may see different carrier densities and therefore, different gain. One could describe all these effects and others under the umbrella term of mode-matching. In short, the model assumes perfect mode-matching, which is impossible to achieve in these experiments.

Still, these measurements of R and R_c move together as the model predicts. As current increases, $R \rightarrow 0.8$ and $R_c \rightarrow 0$, as predicted if the gain/absorption is approaching zero. Experimentally, this point was never reached. The fact that the same pattern occurs as pump power increases, saturating the absorption, adds more credence to the theory. The biggest question is why increasing the current doesn't move the quantum wells past the transparency point. The answer is in the size of the RCLED. A quick calculation shows if one assumes a transparency carrier density of $2 \times 10^{18} \text{ cm}^{-3}$ and a carrier lifetime of 2 ns, and no additional carrier losses, the current to produce transparency is 83 mA! Attempts were made to do four-wave mixing with currents as high as 200 mA, with no sign of a conjugate signal. All the data indicates the quantum well gain never increases to positive values large enough to produce a measurable conjugate signal.

Full spectral reflectivities were measured as the RCLED current was increased to further check for transition to gain. The measurements are shown in Figure 28. A clear indicator of gain would be an on-resonance reflectivity greater than 1. A weaker indicator

would be an on-resonance reflectivity greater than 0.8, the calculated reflectivity when the quantum wells are transparent. There is no indication of gain, even at 200 mA.

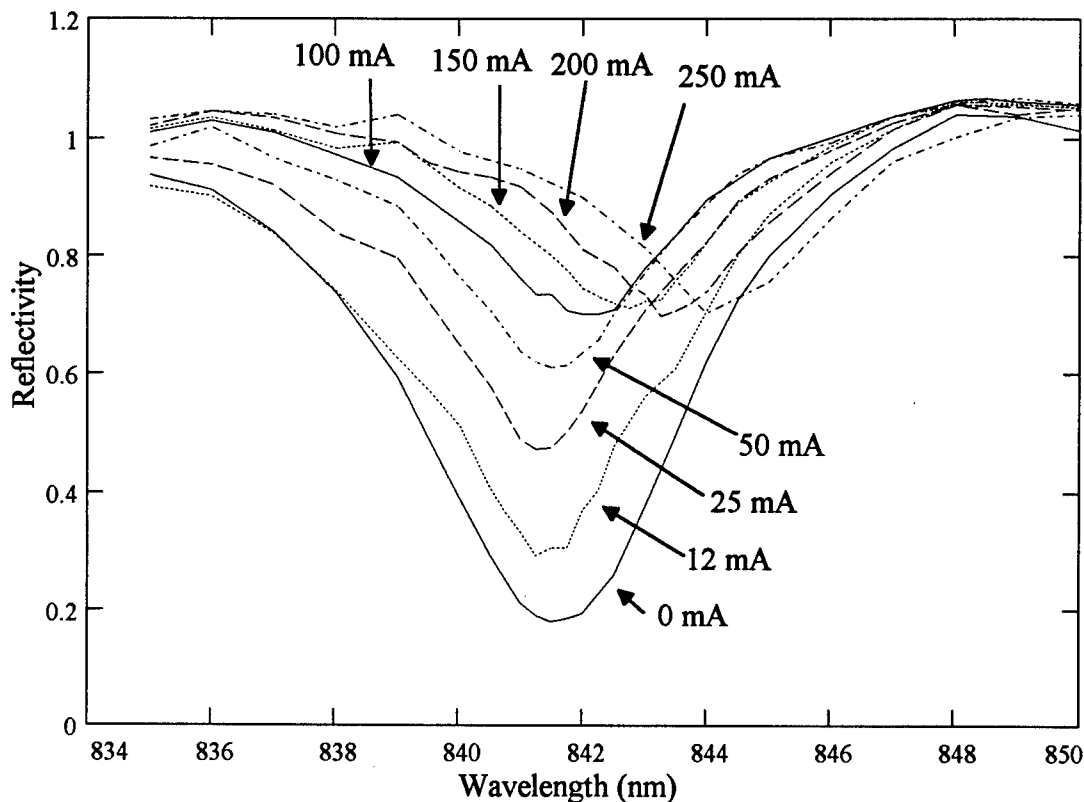


Figure 28. Measured Spectral Reflectivity of RCLED vs. Current. No temperature compensation is made for these measurements, so the reflectivity spectrum red-shifts.

Another bothersome issue is the presence of RCLED spontaneous emission at currents as low as 10 mA, yet the claim is that positive gain is never achieved. Actually, this is not too surprising, once one gets used to the current scale being so high. It is certainly possible to have spontaneous emission with negative gain material. Figure 29, generated from Fitzgerald's model of a quantum well, shows that spontaneous emission is produced before gain is achieved.

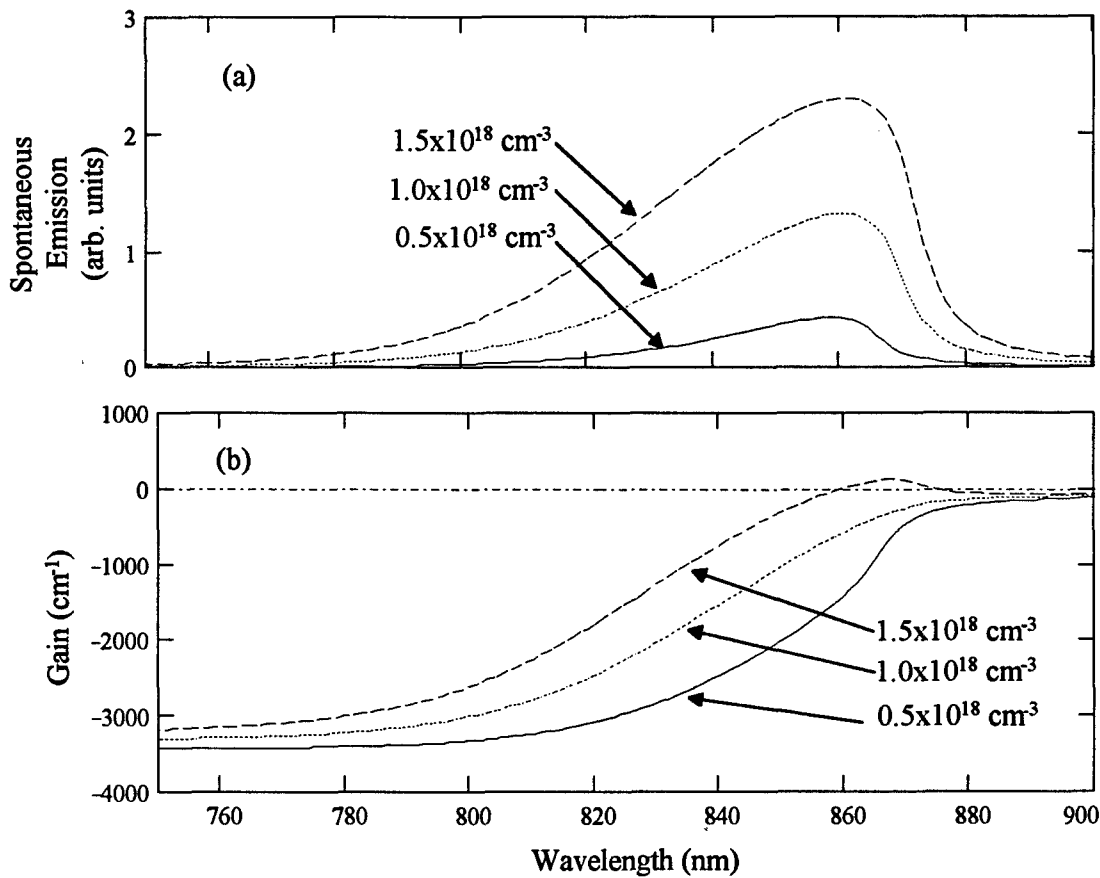


Figure 29. Spontaneous Emission and Spectral Gain for a GaAs Quantum Well. Plot (a) shows spontaneous emission and plot (b) shows spectral gain.

In the end, the experimental results match reasonably well to the model predictions. Experimental limitations prevented a complete mapping of the current/pump power space, but when experiment and model were compared, there was good qualitative agreement. Most importantly, the key features show up in both model and experiment: a minimum in R when the cavity is balanced, a maximum in R_c at the right combination of pump power and current, and a convergence of both R and R_c to the right values (0.8 and 0) as the transparency point was approached.

4.1.4. Probe Beam Offset

In order to investigate whether non-collinear FWM was feasible in short cavities, the probe was offset spatially relative to the pump. The technique used was similar to that used by Awaji. (Awaji, 1993) An optical flat was inserted into the probe beam before it combined with the pump. The result was a probe beam parallel to, but slightly offset from the pump beam. See Figure 30 for a demonstration of the technique.

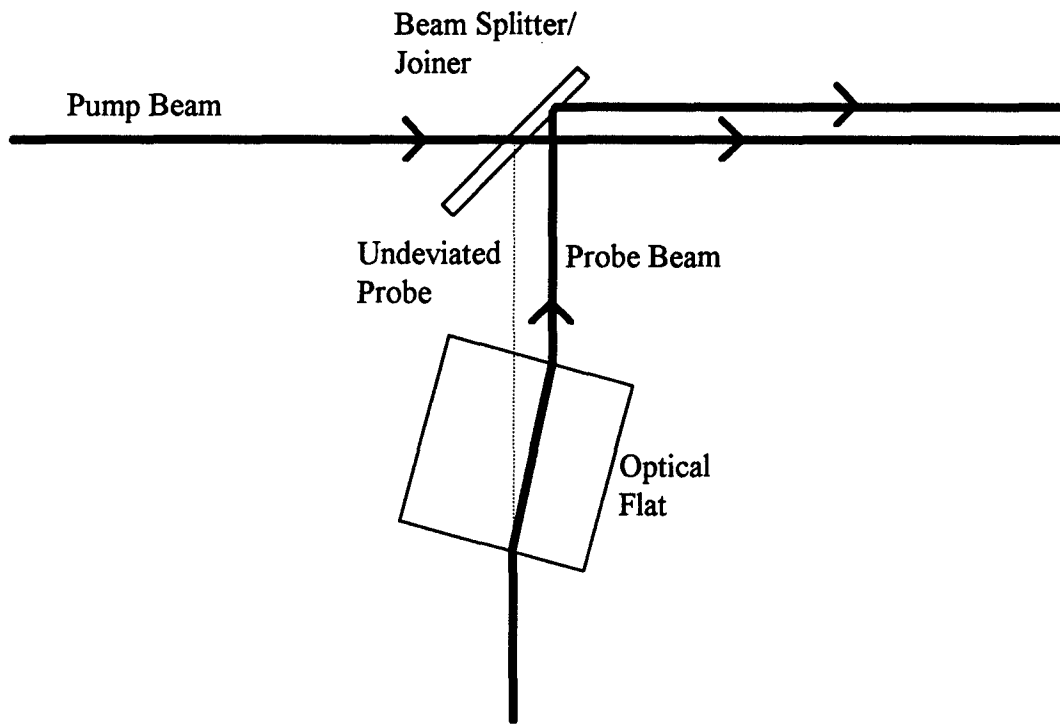


Figure 30. Optical Flat Creating Parallel Offset Beams.

When these parallel beams enter the focusing lens for the VCSEL, they are focused to the same spot, but at different angles. According to phase conjugate theory, the conjugate beam should retrace the path of the injected probe beam, while the conventionally reflected probe should come out on the opposite side of the pump. As the offset d increases, the angle between the pump and probe increases as $\theta = \tan^{-1}(d/f)$, where f is the focal length of the lens (14.5 mm). See Figure 31 for a diagram of this idea.

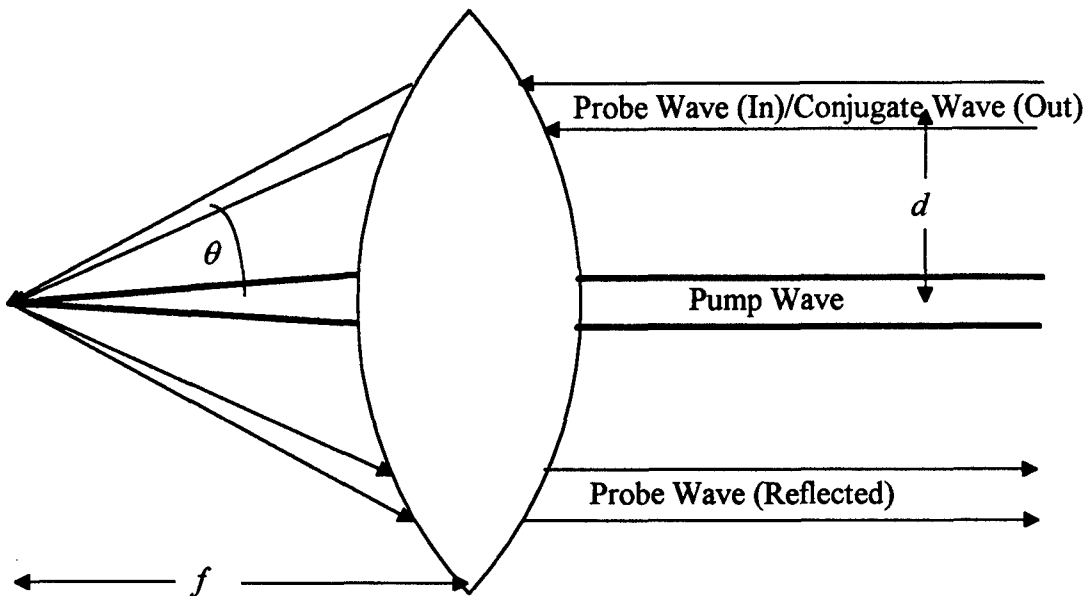


Figure 31. Angular Discrimination of Conjugate Beam Through a Lens.

The strength of the conjugate signal was measured on the FPI as the probe offset was changed. Conjugate reflectivity decreased with increasing angle, as shown in Figure 32. Beyond a few degrees, the conjugate signal was no longer detectable. The rate of decrease of R_c with angle is much less than claimed by Awaji, who fit an exponential decrease with angle to his data.

To spatially discriminate the conjugate from the pump and probe, the probe was offset enough to see a spot on the camera distinct from the bright pump beam, while still producing a conjugate field on the FPI. A razor blade was used to block the conventionally reflected probe and the pump, leaving only the conjugate signal. Unfortunately, the pump and probe were bright enough that their diffraction off the razor edge was brighter than the conjugate beam, preventing a direct observation of the conjugate beam.

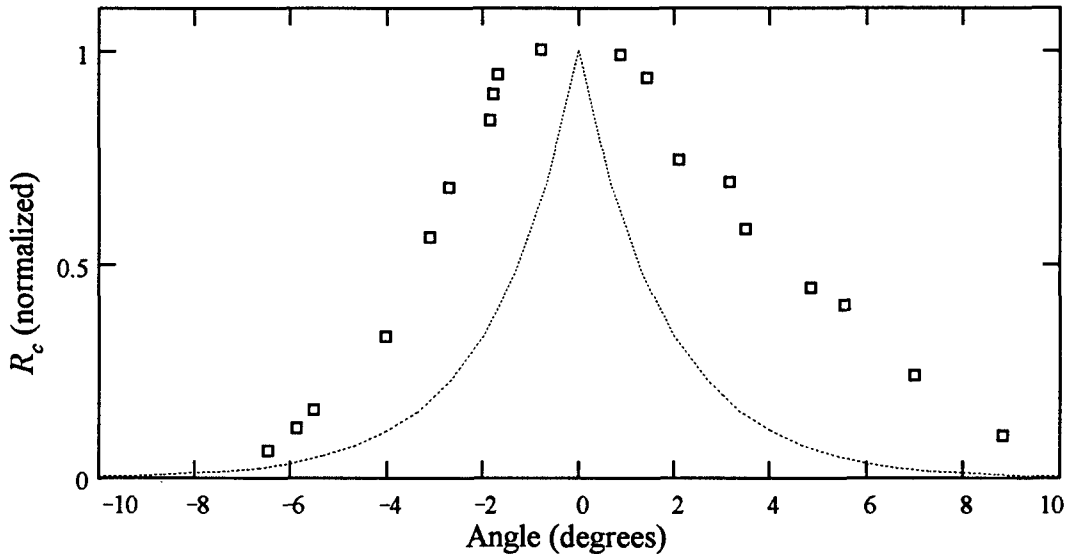


Figure 32. Conjugate Reflectivity vs. Pump-Probe Angle. Squares indicate RCLED data; dotted line are results from Awaji. Data are self-normalized. At $\theta=0$, $R_c \approx 0.01$ for RCLED and $R_c \approx 50$ for Awaji.

Since the camera was not able to discern a spatially separate conjugate beam, an alternate method was used. The razor blade was placed in front of the FPI and scanned across it. The relative strengths of the three fields were measured on the FPI as the blade moved, giving an idea of the location of the beams. The results are shown in Figure 33. The conjugate is clearly spatially discriminated from the pump, and is located opposite to the conventionally reflected probe. This is the first reported spatial separation of a conjugate wave in a vertical cavity device.

Retracing of the probe input path by the conjugate wave is a strong indicator that true phase front conjugation is occurring. This implies these devices could actually be used to correct mild aberrations on probe beams. Unfortunately, the inability to image the conjugate beam prevents checking for phase conjugation by the usual means of aberration correction.

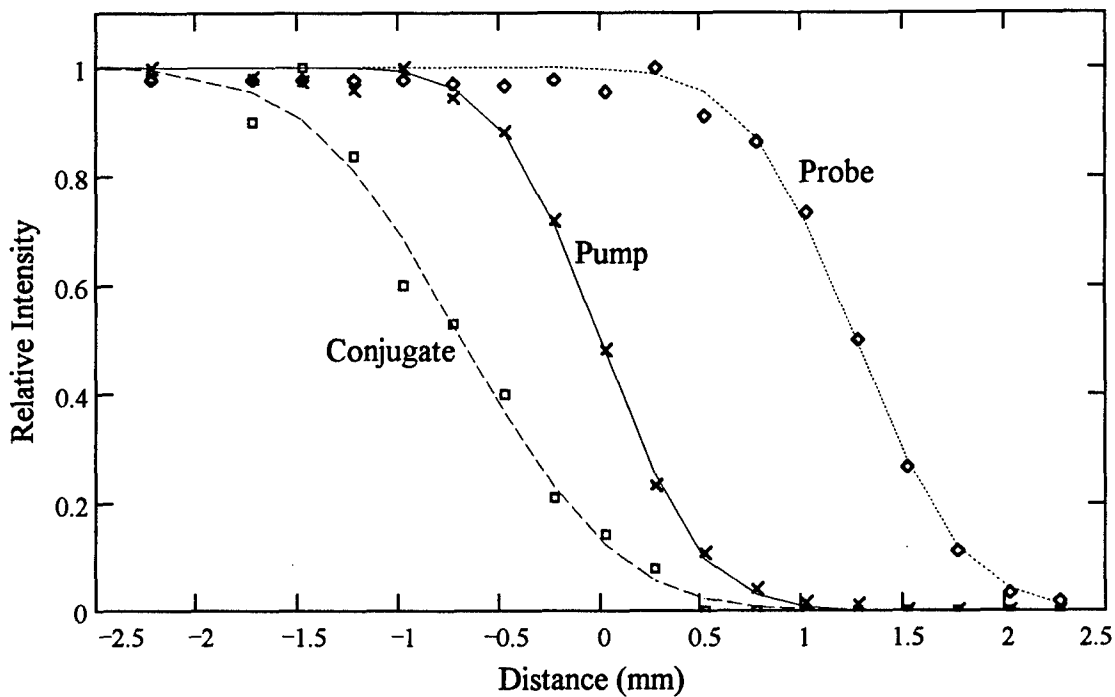


Figure 33. Spatial Separation of Conjugate from Pump and Probe. Experimental measurements are shown as points. The lines are a fit of the data to the theoretical function for a sharp edge scanning across a Gaussian beam. Injection current was zero, pump-probe detuning was 350 MHz, and pump power was about 12 mW.

4.2. VCSEL Results

To complement the investigation of FWM in the RCLED, similar experiments were performed in a VCSEL strongly resembling the RCLED.

4.2.1. Device Information

The VCSEL was also grown by UNM for other purposes, and generously donated for use in this experiment. Its design is very similar to the RCLED, except for the additional layers in the top mirror. Details are in Table 3.

Table 3. Growth Layer Description for UNM VCSEL.

	Layer Composition	Doping (cm ⁻³)	Depth (nm)	Function
Top Mirror	GaAs	p ~10 ¹⁹	40.0	Cap Layer
	Al _{0.15} Ga _{0.85} As	p ~10 ¹⁸	49.8	Mirror High Index
	Al _x Ga _{1-x} As (x=0.15⇒1.0)	p ~10 ¹⁸	12.0	Graded Index
	AlAs	p ~10 ¹⁸	58.6	Mirror Low Index
	Al _x Ga _{1-x} As (x=1.0⇒0.15)	p ~10 ¹⁸	12.0	Graded Index
	Al _{0.15} Ga _{0.85} As	p ~10 ¹⁸	49.8	Mirror High Index
	Al _x Ga _{1-x} As (x=0.15⇒1.0)	p ~10 ¹⁸	12.0	Graded Index
Cavity	Al _x Ga _{1-x} As (x=1.0⇒0.15)	undoped	87.9	Graded Index
	Al _{0.15} Ga _{0.85} As	undoped	10.0	Buffer
	GaAs	undoped	8.0	Quantum Well
	Al _{0.15} Ga _{0.85} As	undoped	10.0	Buffer
	Al _x Ga _{1-x} As (x=0.15⇒1.0)	undoped	87.9	Graded Index
Bottom Mirror	AlAs	n ~10 ¹⁸	58.6	Mirror Low Index
	Al _x Ga _{1-x} As (x=1.0⇒0.15)	n ~10 ¹⁸	12.0	Graded Index
	Al _{0.15} Ga _{0.85} As	n ~10 ¹⁸	49.8	Mirror High Index
	Al _x Ga _{1-x} As (x=0.15⇒1.0)	n ~10 ¹⁸	12.0	Graded Index
	AlAs	n ~10 ¹⁸	58.6	Mirror Low Index
	Al _x Ga _{1-x} As (x=1.0⇒0.15)	n ~10 ¹⁸	14.0	Graded Index
	GaAs	n ~10 ¹⁸	500.0	Smoothing Layer

Fabrication included a conventional ion implanted structure and metal contacts on top and bottom. The top mirror reflectivity was calculated as 0.988 and the bottom mirror reflectivity was 0.987. The threshold current is about 7-9 mA, depending on the particular device, the temperature of operation, and one's definition of threshold. The wavelength of operation is about 841-845 nm. Figure 34 shows a typical family of current/output power curves. They show the laser with different threshold currents for different TEC temperatures, as expected.

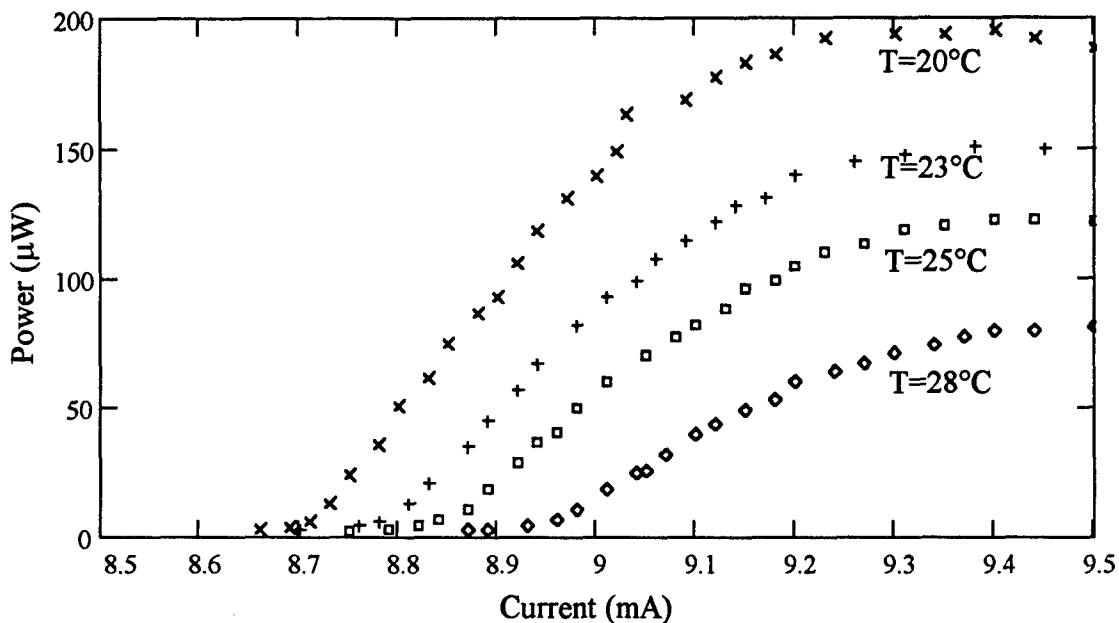


Figure 34. Output Power vs. Current for UNM VCSEL.

The spontaneous emission from the VCSEL below threshold is shown in Figure 35 for a series of different currents. The emission is spectrally much narrower than the RCLED because the cavity has a much higher finesse, reducing the spectral width of the cavity mode. The spontaneous emission is spectrally asymmetric for simple geometric reasons. The light emitted exactly normal to the VCSEL surface ($\theta=0$) comes out at a certain wavelength (λ_0) matched to the cavity length. But light can be emitted at other angles, too. As the angle increases, the mode of the cavity shifts to shorter wavelengths, as demonstrated by measurements performed on the RCLEDs. (Fitzgerald, 1994) But the larger the angle, the weaker the emission, especially out of the high finesse VCSEL. Since the lens in front of the VCSEL collects light emitted at angles up to about 15° , the spectrometer shows the strong $\theta=0$ emission at the longest wavelength, with weaker off-axis radiation at shorter wavelengths. One can also see at the highest current (6 mA) the VCSEL about to start lasing, as the emission strengthens at the long $\theta=0$ wavelength.

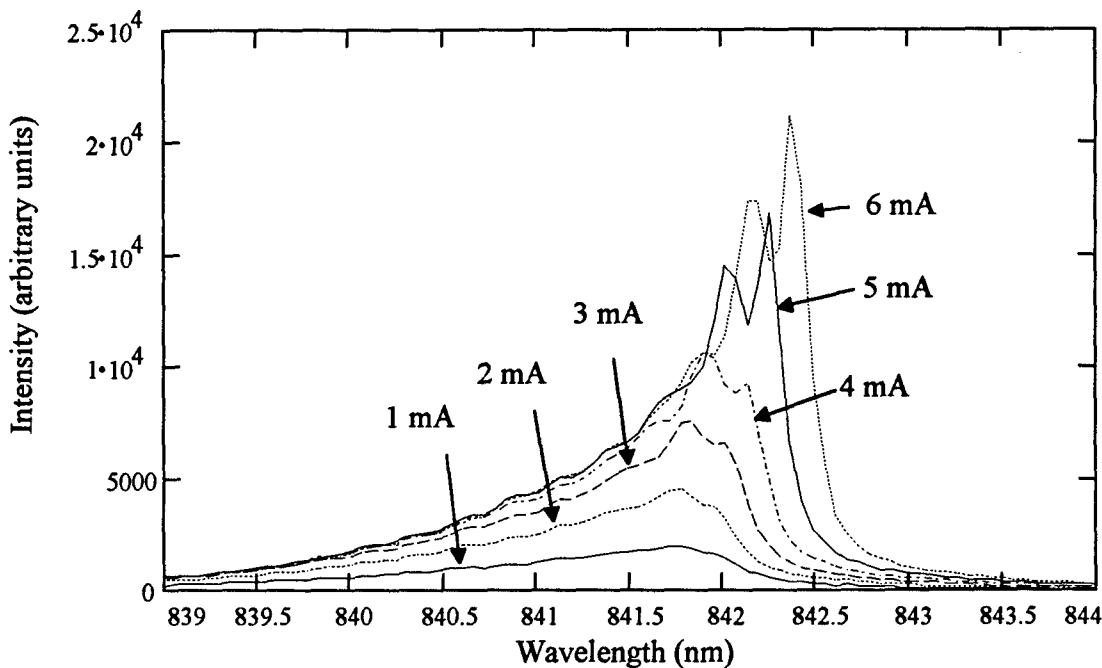


Figure 35. Spontaneous Emission From UNM VCSEL for Various Currents.

This shift with angle became important when tuning the injected signals to the VCSEL's cavity mode when below threshold. Since there was no lasing from the VCSEL itself, the VCSEL mode had to be discerned from the broad spontaneous emission. For matching the VCSEL $\theta=0$ cavity mode, the injected signals were placed on the long wavelength side of the spontaneous emission, contrary to early intuition.

Fortunately, the tunable diode laser could be used to map out a spectral reflectivity curve with great accuracy, allowing better determination of the cavity mode wavelength. Figure 36 shows a series of these spectral reflectivity plots for a VCSEL at different currents. As current increases, the cavity mode shifts first to shorter, then to longer wavelengths. The reason for the initial shift is probably the GaAs quantum wells index change with carrier density, which is negative just above band gap. (Park, 1988) The shift to longer wavelength at higher currents is probably due to heating. Although the copper block and VCSEL substrate were kept at a constant 26 °C, the current creates

considerable local resistive heating in the device. The refractive index of AlGaAs increases with temperature (Bagnell, 1995), making the optical length of the VCSEL cavity increase, shifting the emission to longer wavelengths.

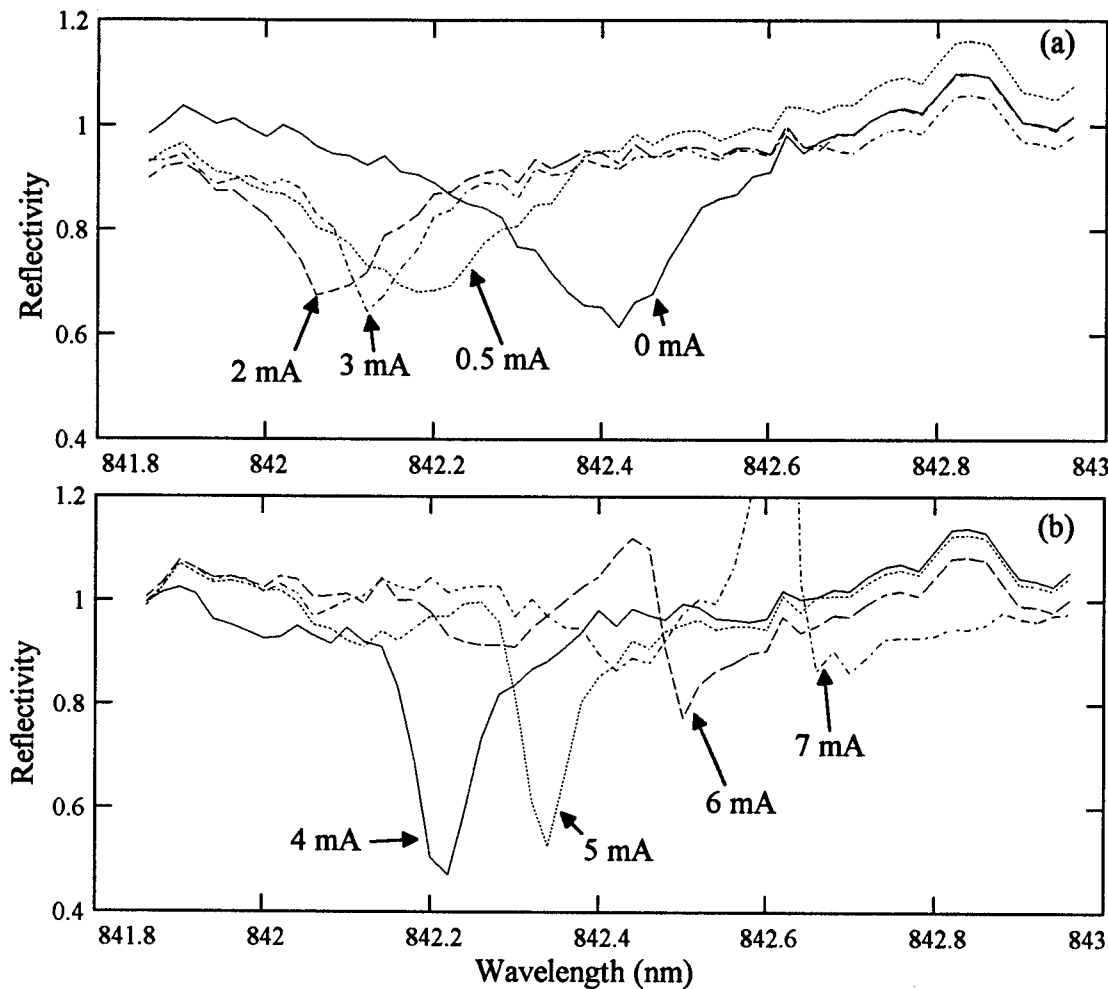


Figure 36. Spectral Reflectivity of UNM VCSEL for Various Currents. Part (a) shows low currents and part (b) shows high currents.

Also seen in Figure 36, the minimum of the reflectivity dip generally decreases with current until about 4-5 mA and then increases with current. This behavior is predicted by the simple Fabry-Perot cavity model with adjustable gain/loss in the cavity.

(See Figure 8) As the current increases, the absorption is reduced and the cavity becomes more nearly balanced. At the cavity balance point, reflectivity is a minimum, theoretically zero. Then, after the absorption turns to gain, the reflectivity of the cavity mode is greater than one. Note that the VCSEL is not lasing yet; there is optical gain in the quantum wells, but the optical gain is less than the optical loss of the cavity until currents exceeds threshold of about 8.5 mA.

4.2.2. Pump-Probe Detuning

Conjugate reflectivity should vary with detuning in the VCSEL much as it did in the RCLED. Model predictions are shown in Figure 37. As with the RCLED, an exponential fit can be made to the results. Both model results and exponential fit are shown. The model predicts a curve that falls off faster than an exponential for small detunings.

The conjugate reflectivity was measured in the VCSEL below threshold as a function of pump-probe detuning. Figure 38 shows results for the VCSEL with no current injection. The data differ from the exponential fit much as the model results did.

For the VCSEL around threshold, in addition to this decay in R_c as detuning increased, there was a peak in R_c at detunings between 10 and 35 GHz. These peaks occurred at values of Ω that depended directly on the amount of pump power being injected. By changing to the FPI with large free spectral range, one could clearly observe the well documented asymmetric gain induced by strong pump power. (Simpson, 1995b; Lowry, 1993) Figure 39 shows the spectrum of the VCSEL and pump with various amounts of pump power. As the amount of pump power injected at the original VCSEL frequency increases, the modified VCSEL mode moves to lower frequencies. The pump-induced asymmetric gain has modified the refractive index of the quantum wells, shifting the VCSEL mode resonance to smaller frequencies as the pump increases.

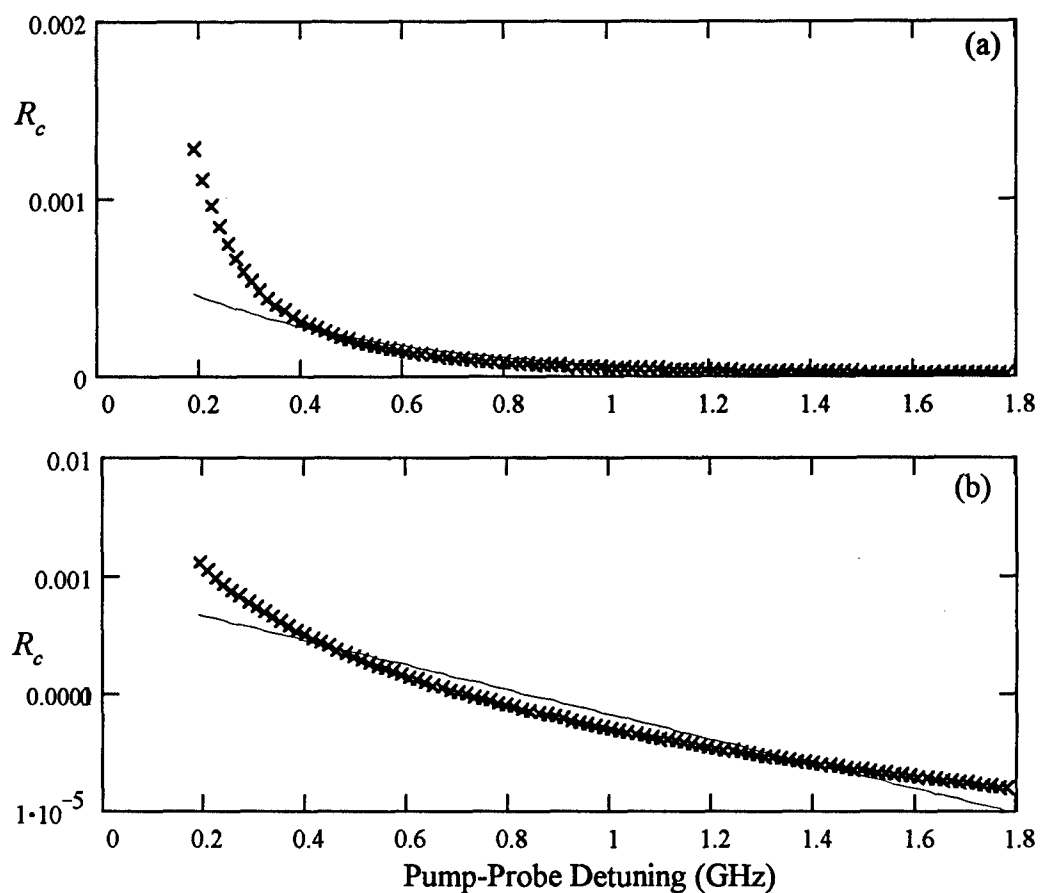


Figure 37. Calculated Conjugate Reflectivity vs. Pump-Probe Detuning in VCSEL. Data points show output from model, while the line shows an exponential fit to the data. Plot (a) is a log plot, (b) is a linear plot. Current was 0 and pump power was 0.5 of saturation power.

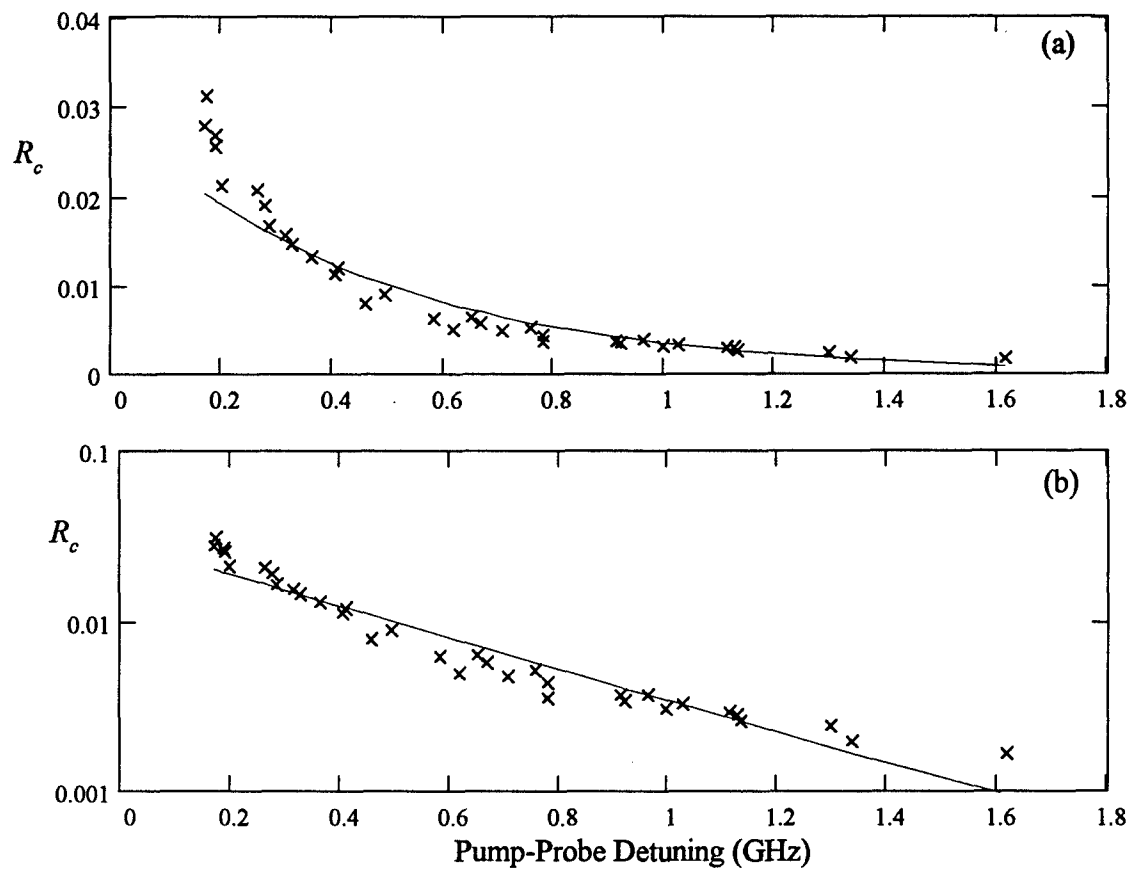


Figure 38. Measured Conjugate Reflectivity vs. Pump-Probe Detuning. Data points show measurements, while the line shows an exponential fit to the data. Plot (a) is a log plot, (b) is a linear plot. Current was 0 and pump power was 12 mW.

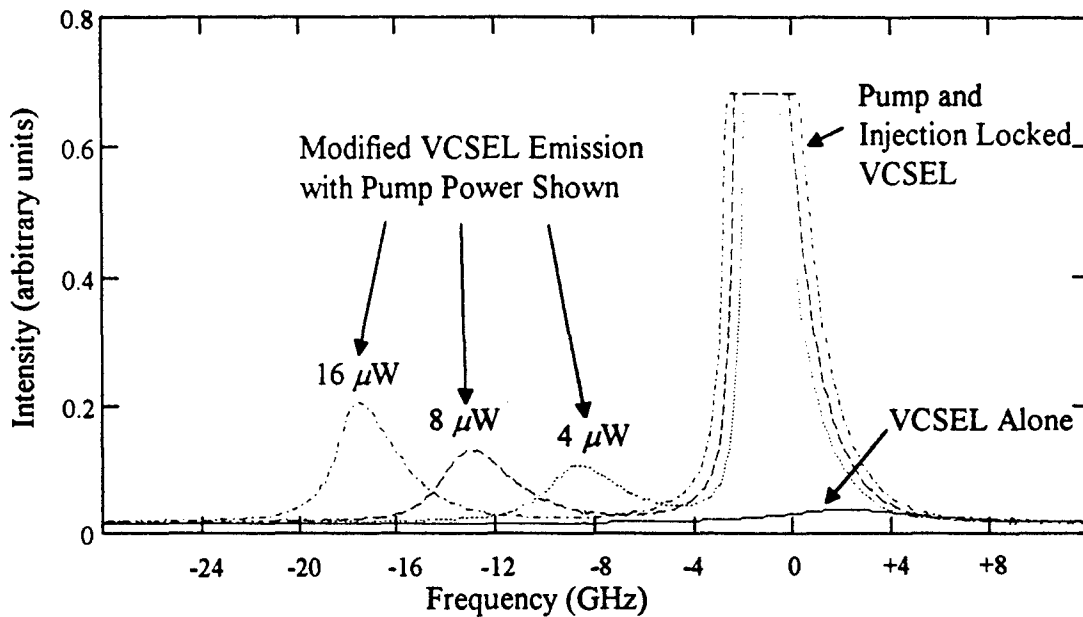


Figure 39. Spectrum of VCSEL with Injected Pump. The three modified peaks indicate new VCSEL cavity modes caused by a power-dependent index change in the quantum wells.

The detuning between the original VCSEL frequency and the modified frequency is plotted versus injected pump power in Figure 40. For the case examined, the relationship was fairly linear. Then, for the same pump powers, a measurement of FWM was made and the value of Ω when R_c reached its peak (call it Ω_R) was noted. The frequencies were identical, confirming the link between the theory of gain modification by coherent transfer of energy (CTE) in semiconductors (Lowry, 1993) and the relaxation oscillations in a lumped oscillator modified by injection locking (Simpson, 1995). While CTE predicts that the relationship between detuning and injected power is always linear, the lumped oscillator model shows a large variability in the relationship, depending on VCSEL power, pump power, and initial pump-VCSEL detuning.

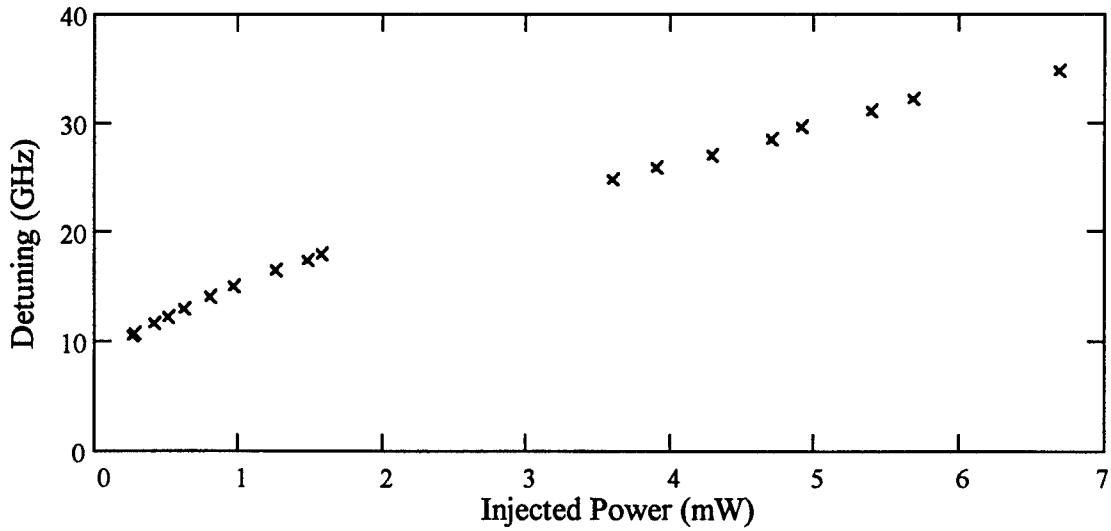


Figure 40. Detuned VCSEL and Ω_R vs. Injected Pump Power. The FPI mode spacing was about 20 GHz, causing a gap in the detuning data at this point.

4.2.3. Pump Power and Bias Current

Model predictions for the VCSEL are much the same as for the RCLED. The VCSEL definitely crosses the transparency point and attains gain, as shown in Figure 36. The conjugate reflectivity and probe reflectivity are shown in Figure 41 as a function of pump power for a few currents. As in the RCLED, the optimum point moves to lower currents for higher powers, and vice versa. The probe reflectivity is included in Figure 41b to show correlation between a maximum in R_c and a local minimum in R_p .

Experimental data for low currents, where the FWM was occurring in absorbing quantum wells, is shown in Figure 42a. The results are very similar to the RCLED. Compare to Figure 25b in the earlier section. The peak of R_c moves with power and current much as the model predicts. Also shown in Figure 42b is the probe reflectivity, which has a minimum that tracks well with the maximum of the conjugate reflectivity.

The data in Figure 42 stop at 1.0 mA because the conjugate signal gets too small to measure. As current is further increased beyond 1.0 mA, the conjugate becomes

detectable again. Figure 43 shows the same data as the current changes in the 4-6 mA region. Again, the point at which R_c is maximum moves to lower pump power as current increases. Note the pump powers are an order of magnitude lower than the data in Figure 42 and the values of R_c are much higher, on the same order of magnitude as R_p . For absorption, R_c is below R_p ; for gain, they are approximately the same. Again, the minimum in R_p tracks the maximum of R_c over most of the region.

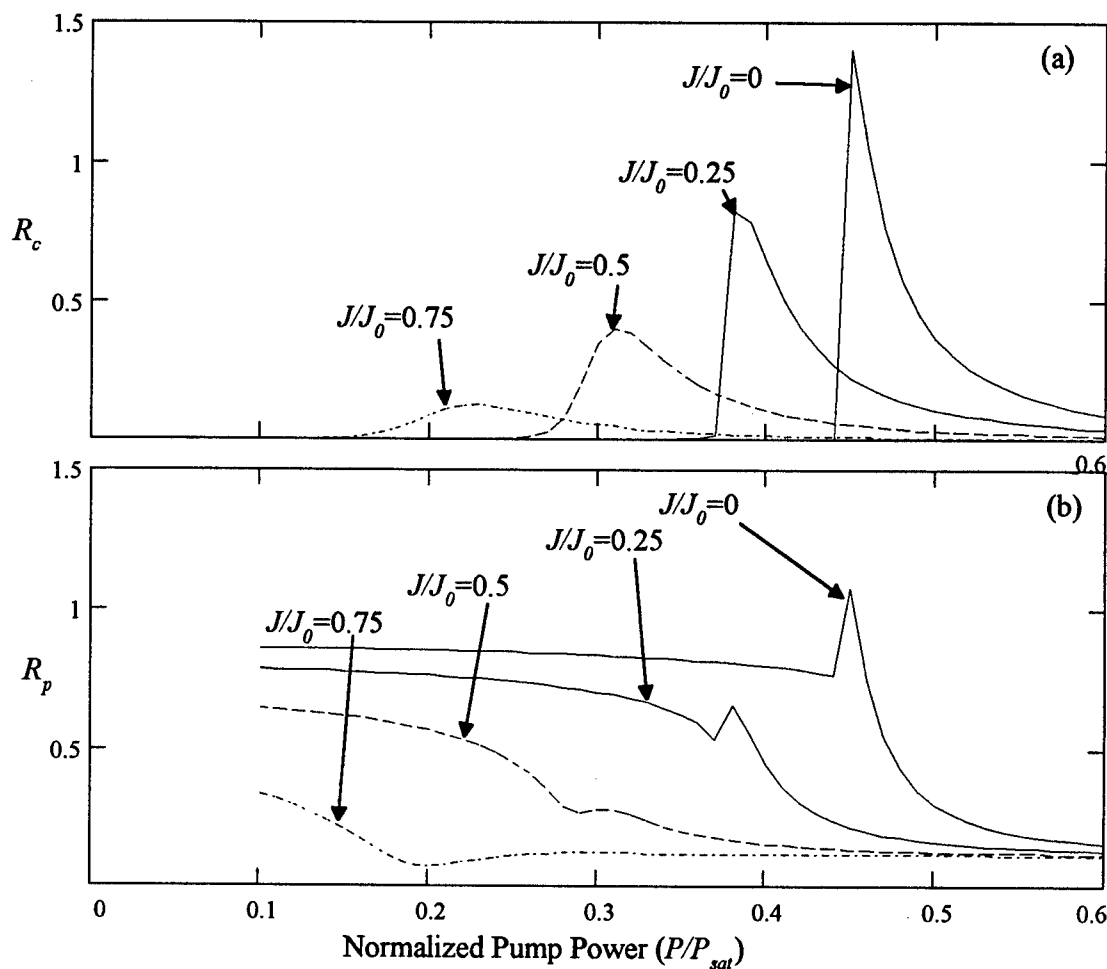


Figure 41. Calculated Probe and Conjugate Reflectivity vs. Pump Power for Various Currents. Plot (a) shows conjugate and (b) shows probe.

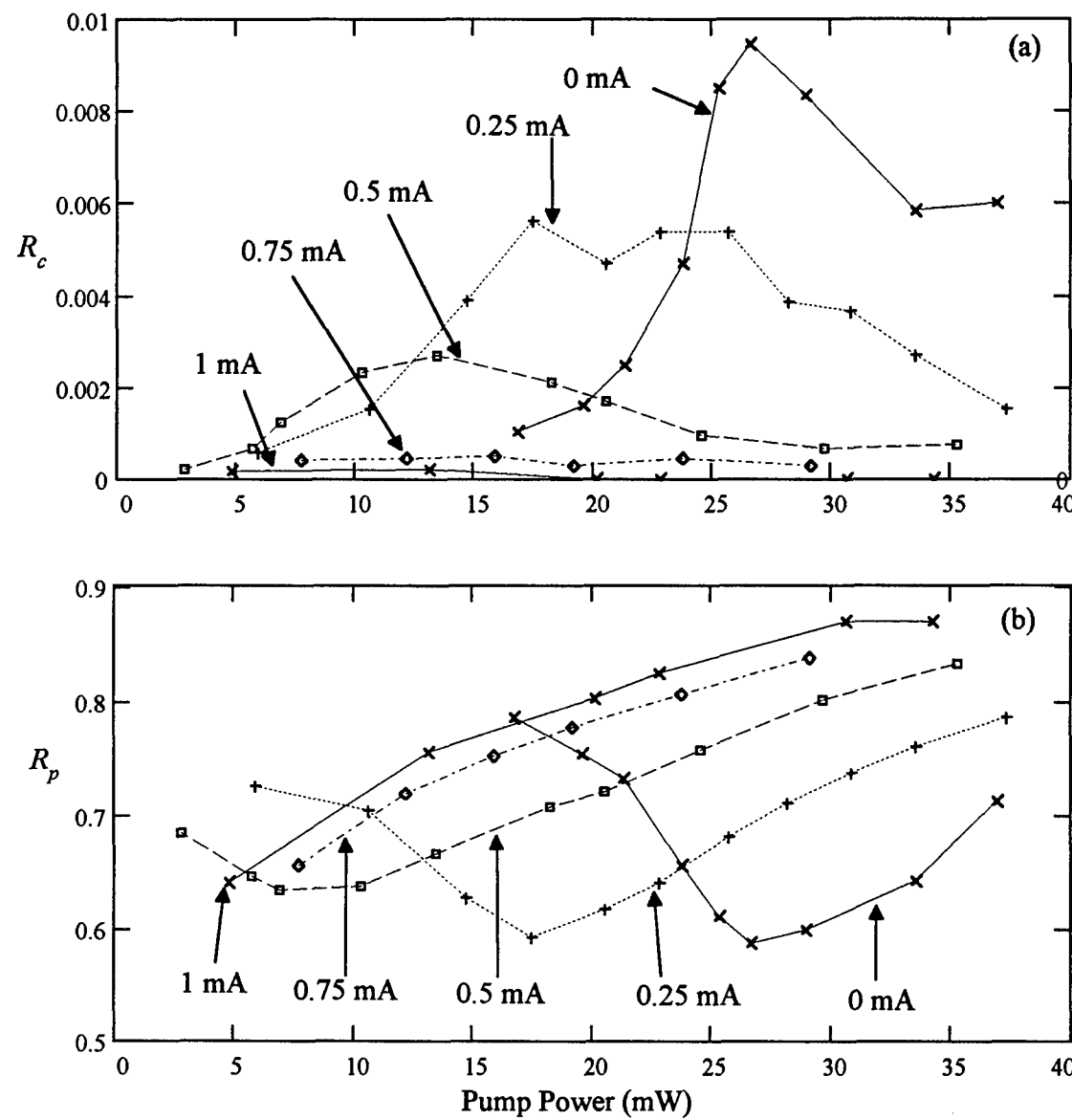


Figure 42. Measured Conjugate and Probe Reflectivity vs. Pump Power and Current. Plot (a) shows R_c and (b) shows R_p . Pump-probe detuning was $\Omega/2\pi=350$ MHz.

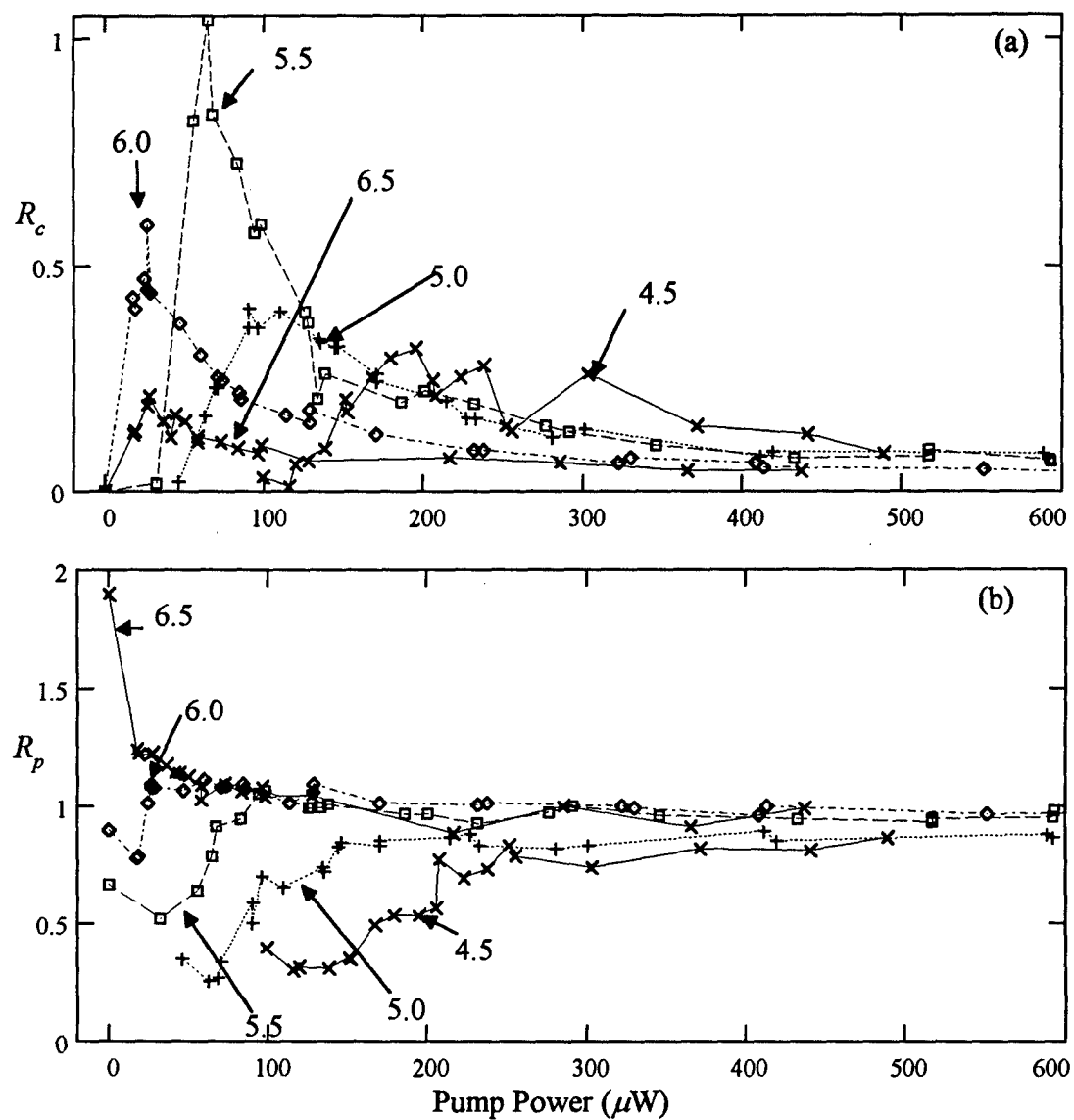


Figure 43. Conjugate and Probe Reflectivity vs. Pump Power for Various Currents. Plot (a) shows R_c and (b) shows R_p . Data were taken with a fixed pump-probe detuning of $\Omega=350$ MHz. Indicated currents are in mA.

The trend for the peak in R_c to move to lower powers with higher currents seems to be a consistent one over a large range of current and power. From the disappearance of FWM between 1 and 4 mA, it would seem that would correspond to the transparency region. A simple calculation predicts that the transparency current is on the order of a few

mA. Looking at Figure 36, it would seem the cavity balance point is around 4-5 mA, where the reflectivity dips the lowest. Unfortunately, there is not a more precise way to measure the gain vs. current or to more accurately determine the mirror reflectivities. The mirror reflectivities calculated earlier show the two mirrors are nearly identical. But from simple balanced cavity analysis, it seems the bottom mirror may be slightly less reflective than the top, since the balance point seems to occur at higher current (and higher gain) than transparency.

4.2.4. Pump-Cavity Detuning

For the VCSEL, detuning of the cavity mode from the pump frequency has a large effect on the FWM. This was less true for the RCLED, since the cavity mode was many nanometers wide. For the VCSEL, the cavity mode was no more than 0.2 nm wide. The effects of detuning were investigated by slightly changing the TEC temperature and measuring R , R_c , and R_p . Figure 44 shows the spectral reflectivity of the VCSEL measured by the tunable diode laser at three temperatures, along with the wavelength of the pump laser. The shape of the spectral reflectivity is strange and has not been explained. It is neither a dip nor a peak, but one of each, in a dispersion-like curve.

The power of the pump was varied and the various reflectivities measured. Results are shown in Figure 45. The pump power at which R_c peaked changed radically with temperature tuning, from 1 mW at $T=31^\circ\text{C}$ to 100 μW at $T=33^\circ\text{C}$. From the spectral plot, it seems the cavity was best matched to the pump laser wavelength at $T=33^\circ\text{C}$, where the dip occurred. So one would expect for a pump laser wavelength of 842.8 nm, $T=32^\circ\text{C}$ would provide the best cavity match.

Note the uncertainty of the data reported in Figure 45 is about 10-15%, except at the lowest powers for each temperature. In these areas, uncertainty is large because there is a bistability point in VCSEL reflectivity which affects all three reflectivities. Figure 46 shows the spectral reflectivity at $T=33^\circ\text{C}$ for various levels of pump power. At the

highest power level, the reflectivity jumps radically. This jump occurs throughout the operating regime of the VCSEL, and seems to be the temperature-based reflective bistability investigated in VCSELs at AFIT in earlier years. (Peters, K. M., 1994; Bagnell, 1995) Measurements of pump reflectivity vs. pump power showed identical results to those reported by Peters for other VCSELs; a clear bistable region that shifted to different powers for different pump-VCSEL detunings.

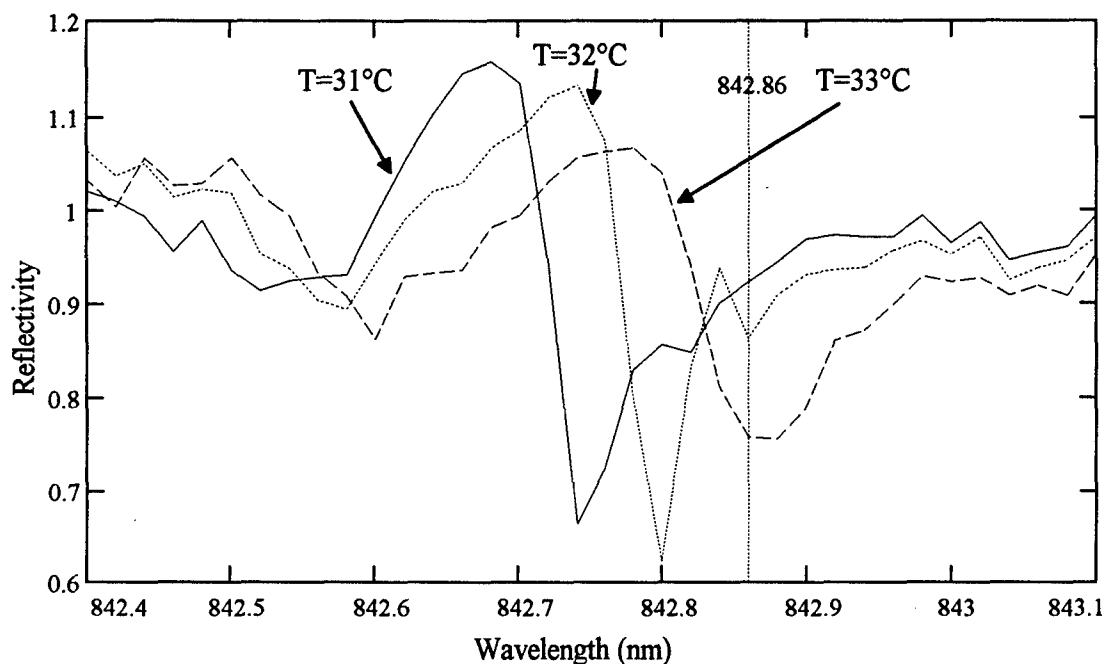


Figure 44. Spectral Reflectivity of VCSEL at 5.5 mA for Three Temperatures. The wavelength of the pump laser for FWM experiment is shown at 842.86 nm.

The jump manifested itself in FWM data. A careful examination of Figure 45 shows the values for R_c and R_p jumping between two levels at low pump powers for each of the three temperature data sets.

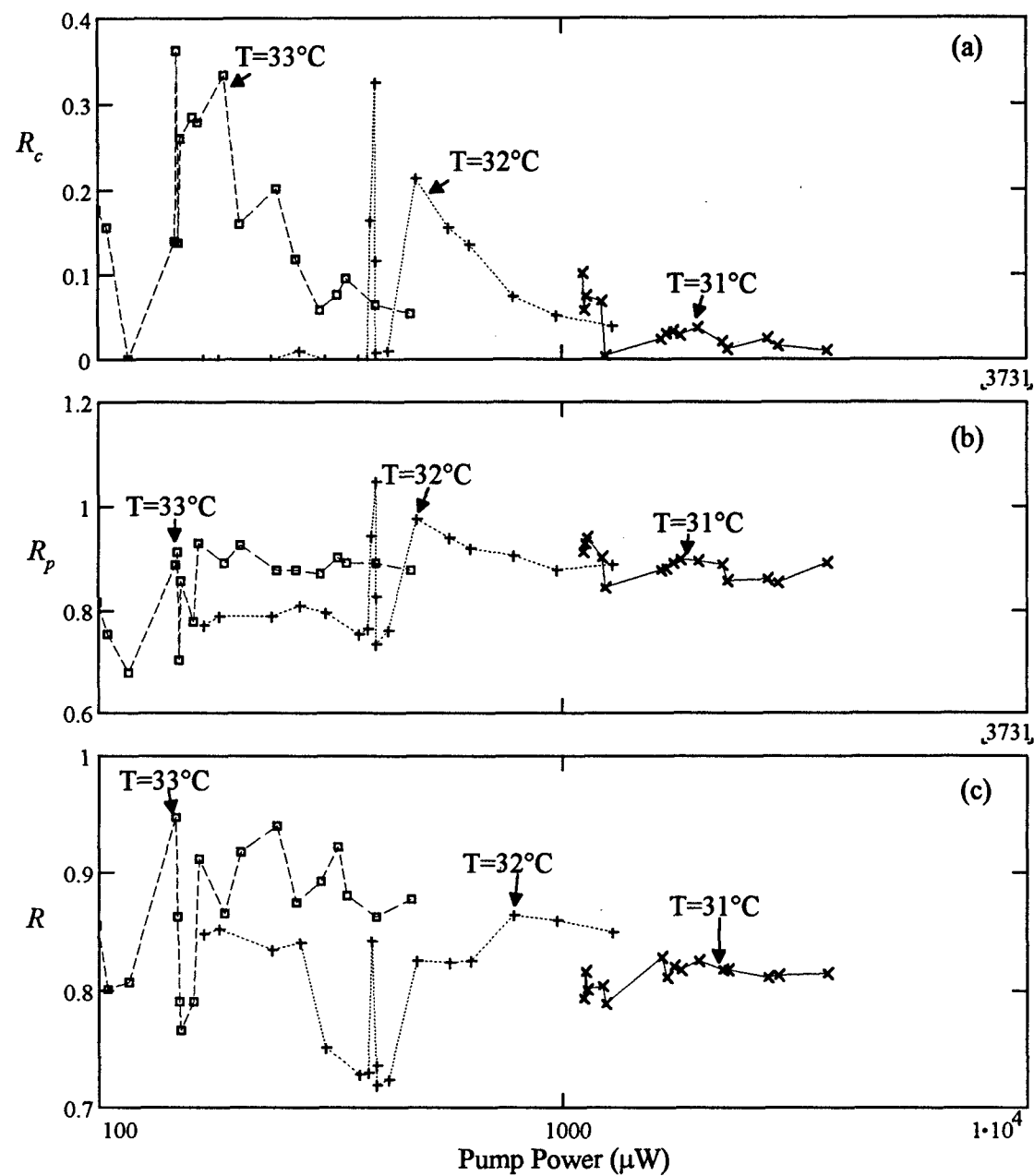


Figure 45. Conjugate, Probe, and Pump Reflectivity vs. Pump Power and Temperature Tuning. Plot (a) shows conjugate, (b) shows probe, and (c) shows pump. Pump-probe detuning was 350 MHz and current was 5.5 mA.

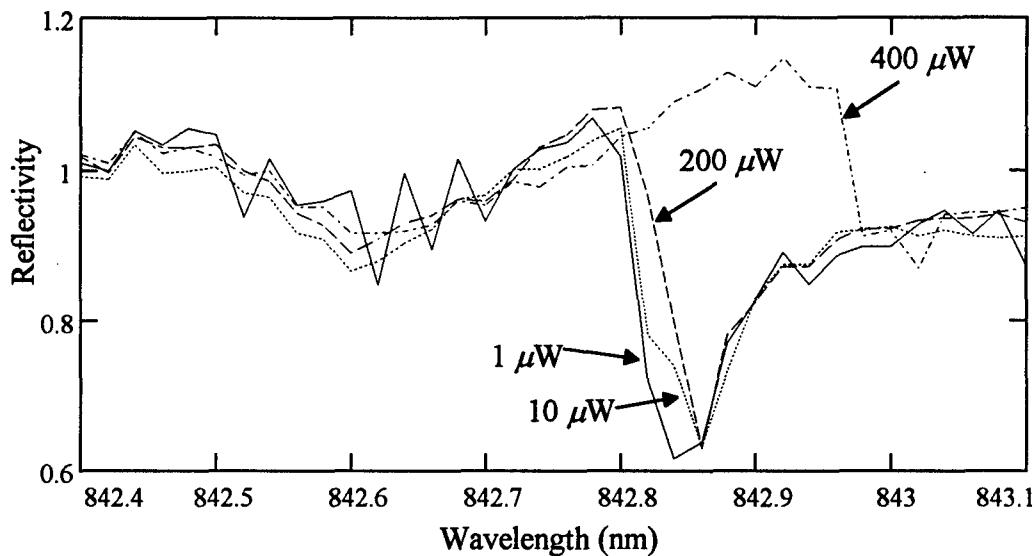


Figure 46. Spectral Reflectivity of VCSEL for Four Power Levels.

4.2.5. *Probe Beam Offset*

The dependence of R_c on pump-probe angle was similar to the RCLED's. Results of the measurement are shown in Figure 47, along with the earlier RCLED angle data. Despite the similarity of angle data to the RCLED results, the razor blade measurements of the location of the conjugate beam showed very different results. As seen in Figure 48, the conjugate beam appears to be collinear with the pump, or slightly smeared in the direction opposite to the probe. Similar measurements were made many times for both devices, and the results were consistent with what is reported here. The VCSEL seems to be acting like a much stronger spatial filter than the RCLED, as predicted in the background section.

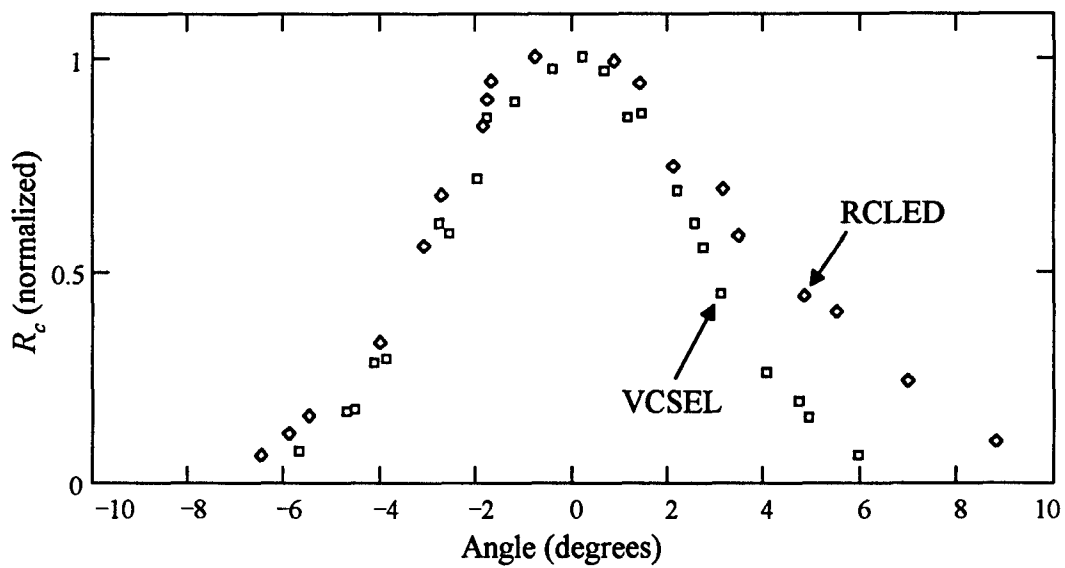


Figure 47. Conjugate Reflectivity vs. Pump-Probe Angle. Results are compared to the RCLED data previous seen in Figure 32. Pump power was 12 mW, detuning was 350 MHz.

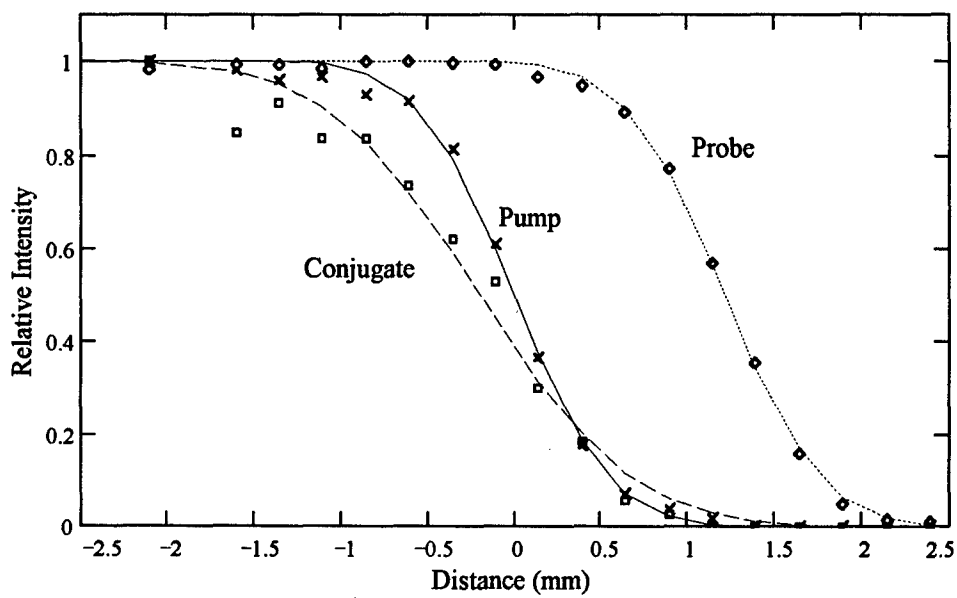


Figure 48. Relative Intensity of Three Beams vs. Razor Blade Position. Experimental measurements are shown as points. The lines are a fit of the data to the theoretical function for a sharp edge scanning across a Gaussian beam.

4.3. Additional Modeling Results

The good qualitative fit between model and experiment indicates the model has captured the essential features of FWM in VCSELs both below and above threshold. The model will be used to explore a unique possibility in the use of these devices to do FWM: discrimination of the conjugate from the pump and probe via cavity balancing.

The idea, proposed earlier, is simple: find a combination of mirror reflectivities and active region gain/absorption that produces near-zero reflectivity for the pump and probe fields, but non-zero reflectivity for the conjugate. This may seem impossible. After all, conservation of energy requires that for every two pump photons annihilated, one probe photon and one conjugate photon are created. So the probe field must be at least as strong as the conjugate.

For example, if a single field is injected into a cavity mode at the cavity balance point, the reflectivity is zero. This does not mean there is no field in the cavity, just that the field in the cavity that comes out the top mirror exactly cancels the portion of the injected field reflected from the top mirrors. This phase match creates the balance point.

When FWM occurs, the pump and probe may see $R=0$ at the balance point, when their intra-cavity fields exactly cancel the reflection of the injected field from the top mirror. But since the conjugate field *has no injected component*, the cancellation doesn't occur.

Mathematically, this is represented in the asymmetric cavity model. Figure 23 showed three types of devices, and cases (a) and (b) both showed a possible operating point where R was a minimum and R_c was not. For case (b), where the balance point occurred with positive gain, the value of R_c was larger than in case (a). This is the key optimization step: attain cavity balance when the active region is amplifying, not absorbing. This will maximize the conjugate field. To do this, we need the top mirror to be more reflective than the bottom mirror.

The devices used in the experiments did not have this characteristic. The RCLED had $R_1=0.8$ and $R_2=0.98$, which is similar to case (a). The VCSEL had two nearly equal mirrors, $R_1=R_2=0.998$, which is similar to case (c). There was no device similar to case (b) with $R_1>R_2$, since the experiments used off-the-shelf, not customized, devices. A logical follow-up effort would be to grow an optimum device similar to case (b).

The optimum design can be studied through modeling. Figure 49 shows the various reflectivities for a cavity with $R_1=0.9$ and $R_2=0.8$ as a function of current for the quantum wells modeled earlier. Results are calculated for three different values of β . At the balance point the pump reflectivity (R) drops below R_c and R_p .

However, R_p does not generally fall below R_c . The reason is simple. In a cavity without nonlinear mixing, the weak probe field would be balanced at the same point as the pump field, and their reflectivities should be the same everywhere. With FWM occurring, the probe field is amplified, as is the conjugate field. The extra probe photons unbalance the probe field and result in $R_p > R$ and $R_p = R_c$ at the balance point.

Pump power has a similarly strong effect on behavior at the balance point. Figure 50 shows a sequence of the same plots for various pump powers. For some pump powers it is possible for R_c to exceed R_p , but not at the cavity balance point.

Nonetheless, by operating at the balance point, we still get rid of most reflected pump power, which is the major source of unwanted reflected photons. If angle discrimination is used in conjunction with cavity balance techniques, it may offer a way to select the conjugate beam and reject the unwanted pump and probe.

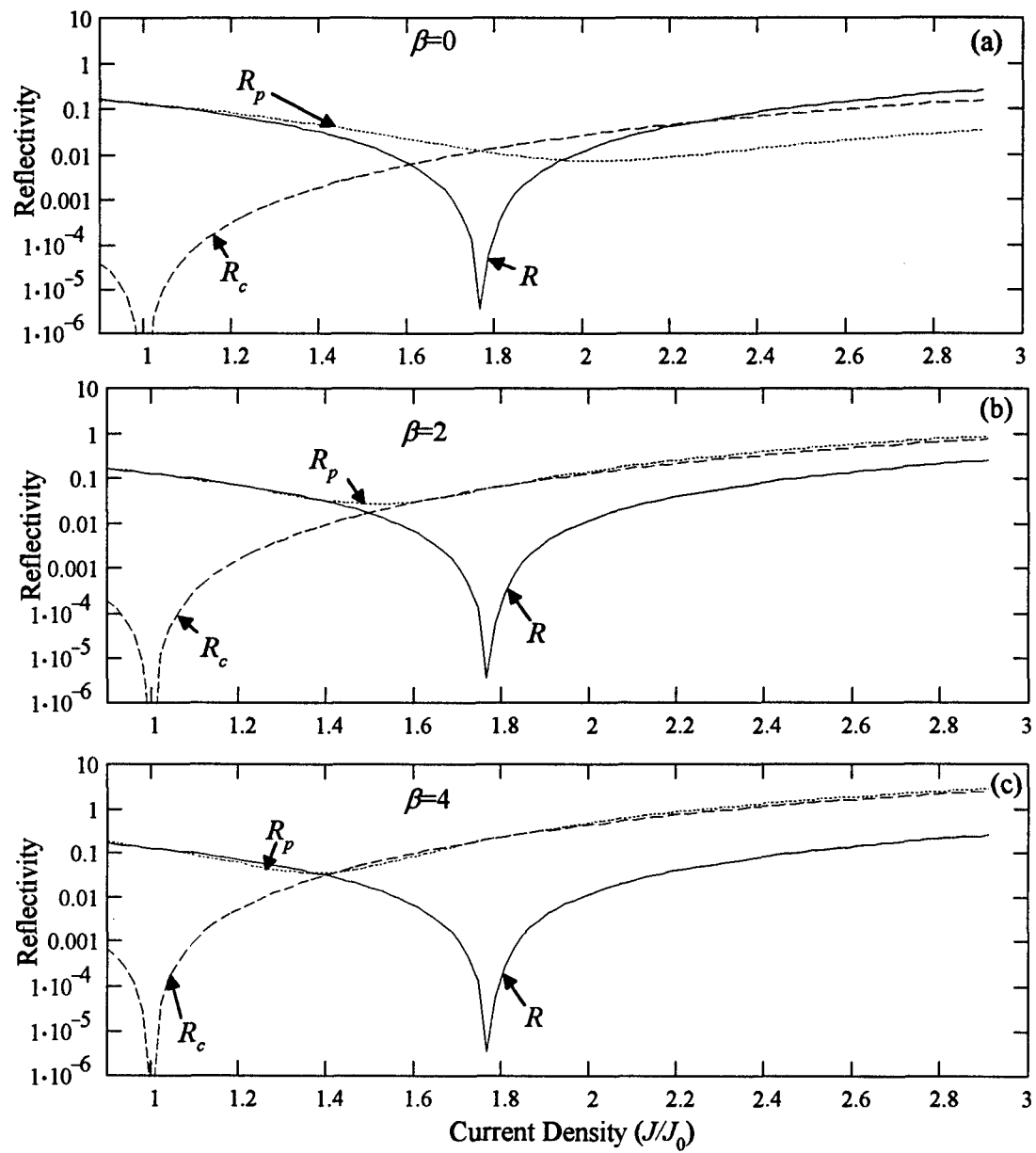


Figure 49. Calculated Pump, Probe, and Conjugate Reflectivity vs. Current for Three Values of Linewidth Enhancement Factor. Plot (a) is $\beta=0$, (b) is $\beta=2$, (c) is $\beta=4$. Pump power was $P=0.19P_{sat}$.

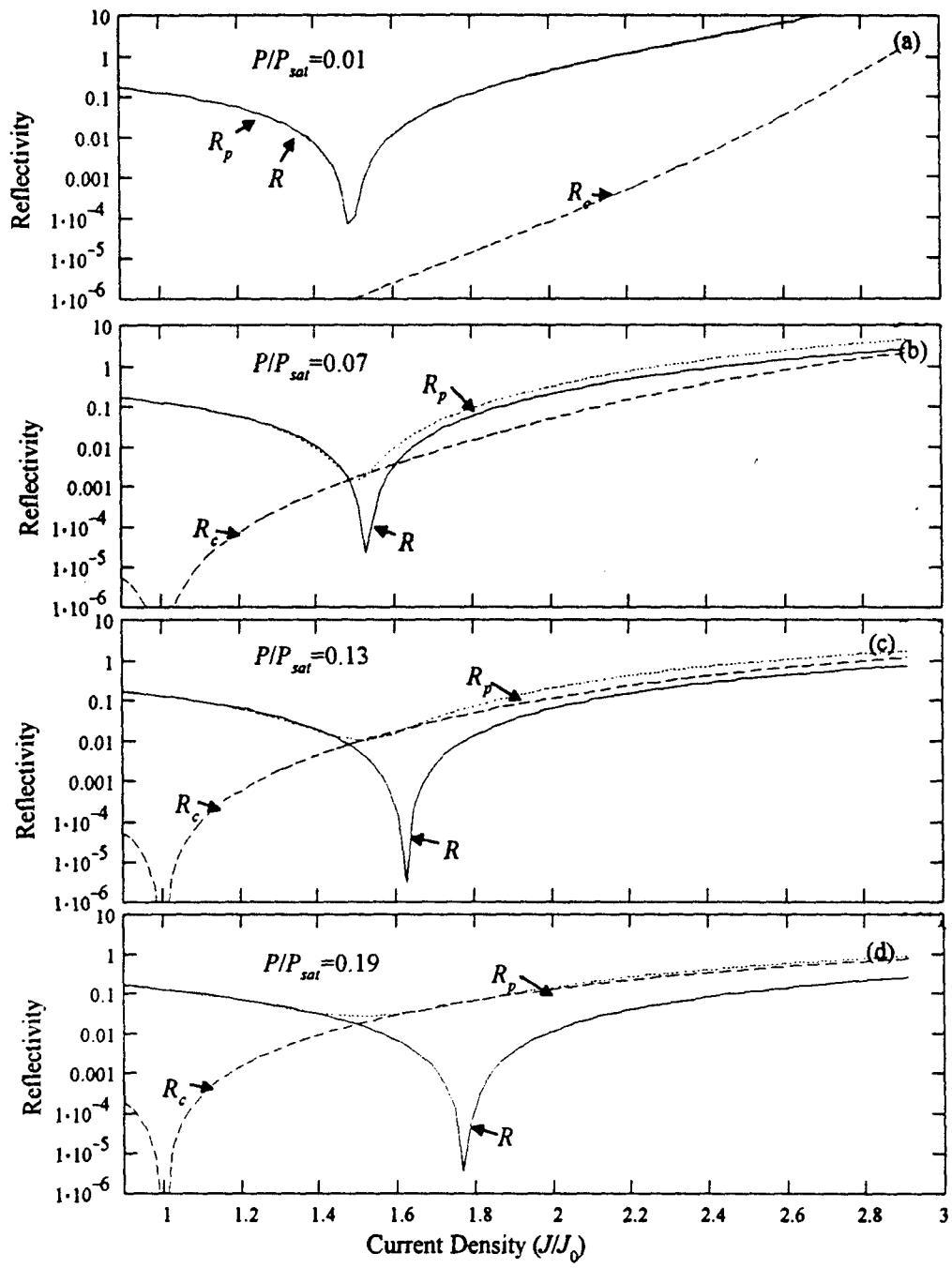


Figure 50. Calculated Pump, Probe, and Conjugate Reflectivity vs. Current for Various Pump Powers. Linewidth enhancement factor was $\beta=4$.

5. *Conclusions*

Four-wave mixing in vertical cavity semiconductor devices operating below threshold has been thoroughly explored. The effects of pump power, pump-probe detuning, current and gain, probe injection angle, and cavity-pump detuning have been investigated and agree qualitatively with results from a model based on asymmetric cavities and carrier population pulsations.

Conjugate reflectivity decreased as pump-probe detuning increased. Measurable FWM occurred for detunings up to 1-2 GHz in RCLEDs and VCSELs below threshold. In VCSELs near threshold, a peak in FWM occurred at large detunings ranging from 10-30 GHz, depending on the pump power.

Conjugate reflectivity depended on pump power and current in a complex manner, as predicted by modeling. Minimum conjugate reflectivity occurred at the quantum well transparency current. Below the transparency current, when the quantum wells had negative gain, certain pump power and current combinations produced a local maximum of $R_c=0.01$ for both RCLED and VCSEL. When the VCSEL quantum wells had positive gain, $R_c=1$ was measured for certain combinations of current and pump power. This high reflectivity in a device not optimized for FWM indicates that practical applications are possible.

Noncollinear FWM was characterized for the first time in a vertical cavity device. Conjugate reflectivity decreased with increasing pump-probe angle. Reasonable conjugate reflectivities were obtained for pump-probe angles up to 10° in both VCSEL and RCLED. Experiments with the RCLED showed the conjugate beam retraced the path of the input probe. This indicates phase front conjugation, which can be used to correct aberrations on optical signals.

Two new techniques have been demonstrated for discriminating a conjugate wave from the strong pump and weaker probe. A geometrical technique based on injecting the

probe beam at an angle to the pump beam worked in the low finesse RCLED but not in the high finesse VCSEL. The cavity balance technique has been demonstrated in the model and experiment. This technique maximizes conjugate reflectivity while minimizing pump reflectivity, making it easier to discriminate the conjugate wave from the strong pump wave. This is the first time such a technique has been reported, because it is a unique feature of externally pumped active cavities.

There are a number of possibilities for future work. Vertical cavity devices optimized for cavity balancing should be grown and tested experimentally. A variety of devices with top mirror reflectivity larger than the bottom mirror reflectivity could be grown to find the optimum combination. The asymmetric cavity model developed here could be used to help design such devices.

The asymmetric cavity model could be improved in a number of ways. The biggest improvement would be a better description of susceptibility (χ) for semiconductor quantum wells. The use of a gain curve with constant linewidth enhancement factor (β) is a simplification that works well for lasers above threshold, but not as well below threshold. Additional theory and experiment to describe χ as a function of carrier density and pump power would make the model more accurate.

Bibliography

Abrams, R. L., and R. C. Lind. "Degenerate Four-Wave Mixing in Absorbing Media," *Optics Letters*, 2(4): 94-96 (April 1978).

Agrawal, Govind P. and N. K. Dutta. *Long-Wavelength Semiconductor Lasers*. New York: Van Nostrand Reinhold, 1986.

Agrawal, Govind P. "Four-wave Mixing and Phase Conjugation in Semiconductor Laser Media," *Optics Letters* 12(4): 260-262 (April 1987).

Agrawal, Govind P. "Population Pulsations and Nondegenerate Four-wave Mixing in Semiconductor Lasers and Amplifiers," *Journal of the Optical Society of America B*, 5(1): 147-158 (January 1988).

Agrawal, Govind P. "Spectral Hole Burning and Gain Saturation in Semiconductor Lasers: Strong Signal Theory," *Journal of Applied Physics*, 63(4): 1232-1234 (15 February 1988).

Awaji, Yoshinari, Shuji Sayama, Hiromasa Suzuki, Motoichi Ohtsu, Yasumasa Teramachi. "Generation of Phase Conjugate Wave from a Visible InGaAlP Laser," *Japanese Journal of Applied Physics, Part 1*, 32(3A): 1107-1111 (March 1993).

Bagnell, Richard J. *Experimental Investigation and Computer Modeling of Optical Switching in Distributed Bragg Reflector and Vertical Cavity Surface Emitting Laser Structures*. Ph.D. Dissertation, AFIT/DS/ENP/95-04, School of Engineering, Air Force Institute of Technology, Wright-Patterson AFB, OH, December 1995.

Bogatov, A. P., P. G. Eliseev, and B. N. Sverdlov. "Anomalous Interaction of Spectral Modes in a Semiconductor Laser," *IEEE Journal of Quantum Electronics*, QE-11(7): 510-515 (July 1975).

Boggavarapu, D., R. Jin, J. Grantham, Y. Z. Hu, F. Brown de Colstoun, C. W. Lowry, G. Khitrova, S. W. Koch, M. Sargent III, H. M. Gibbs, and W. Chow. "Instabilities of a Microcavity Laser with a Weak Injected Signal," *Optics Letters*, 18(21): 1846-1848 (November 1993).

Brown, Scott. *Characterization of Nonlinear Effects of Optically Pumped Vertical Cavity Surface Emitting Lasers*. MS thesis, AFIT/GEO/ENP/93D-01, School of Engineering, Air Force Institute of Technology, Wright-Patterson AFB, OH, December 1993.

Brown, W. P. "Absorption and Depletion Effects on Degenerate Four-wave Mixing in Homogeneously Broadened Absorbers," *Journal of the Optical Society of America B*, 73(5): 629-634 (May 1983).

Butcher, P. N. and D. Cotter. *The Elements of Nonlinear Optics*. New York: Cambridge University Press, 1990.

Chinn, S. R. "Measurement of Nonlinear Gain Suppression and Four-wave Mixing in Quantum Well Lasers," *Applied Physics Letters*, 59(14): 1673-1675 (30 September 1991).

Choquette, Kent D. and R. E. Leibenguth. "Control of Vertical Cavity Laser Polarization with Anisotropic Transverse Cavity Geometries," *IEEE Photonics Technology Letters* 6(1): 40-42 (January 1994).

Chow, Weng W., Stephan Koch, and Murray Sargent III. *Semiconductor Laser Physics*. Berlin: Springer-Verlag, 1994.

Fisher, Robert A. *Optical Phase Conjugation*. Orlando, FL: Academic Press, Inc., 1983.

Fitzgerald, T. M. *Design and Characterization of Resonant Cavity Light Emitting Diodes*. MS thesis, AFIT/GEO/ENG/94D-02, School of Engineering, Air Force Institute of Technology, Wright-Patterson AFB, OH, December 1994.

Frey, R. and B. Thedrez. "Two-level Description of Instabilities in Nonlinear Fabry-Perot Cavities," *Journal of the Optical Society of America B*, 5(5): 1176-1180 (May 1988).

Gallion, Philippe B. and Guy Debarge. "Quantum Phase Noise and Field Correlations in Single Frequency Semiconductor Laser Systems," *IEEE Journal of Quantum Electronics* QE-20(4): 343-349 (April 1984).

Gallion, P., G. Debarge, and C. Chabran. "Output Spectrum of an Unlocked Optically Driven Semiconductor Laser," *Optics Letters*, 11(5): 294-296 (May 1986).

Harris, M., R. Loudon, G. L. Mander, and J. M. Vaughan. "Above-Threshold Laser Amplifier," *Physical Review Letters*, 67(13): 1743-1746 (23 September 1991).

Haug, H., and Stephan W. Koch. *Quantum Theory of the Optical and Electronic Properties of Semiconductors*. Singapore: World Scientific Publishing Co, 1990.

Hui, Rongqing and Antonio Mecozzi. "Phase Noise of Four-wave Mixing in Semiconductor Lasers," *Applied Physics Letters*, 60(20): 2454-2457 (18 May 1992).

Iannone, Patrick P., Alan H. Gnauck, and Paul R. Prucnal. "Dispersion-Compensated 333-km 10-Gb/s Transmission Using Mid-Span Spectral Inversion in an Injection-Locked

InGaAsP V-Groove Laser," *IEEE Photonics Technology Letters* 6(8): 1046-1049 (August 1994)

Iannone, Patrick P., Paul R. Prucnal, Gregory Raybon, Uziel Koren, and Charles A. Burrus. "Nanometer Wavelength Conversion of Picosecond Optical Pulses Using Cavity-Enhanced Highly Nondegenerate Four-Wave Mixing in Semiconductor Lasers," *Journal of Quantum Electronics*, 31(7): 1285-1291 (July 1995).

Jiang, Shijun and Mario Dagenais. "Observation of Nearly Degenerate and Cavity-enhanced Highly Nondegenerate Four-wave Mixing in Semiconductor Lasers," *Applied Physics Letters*, 62(22): 2757-2759 (31 May 1993).

Jiang, Shijun and Mario Dagenais. "Nearly Degenerate Four-wave Mixing in Fabry-Perot Semiconductor Lasers," *Optics Letters*, 18(16): 1337-1339 (15 August 1993).

Jiang, Shijun, Mario Dagenais, and Robert A. Morgan. "Nearly Degenerate Four-wave Mixing in a Vertical Cavity Surface-Emitting Laser," *Applied Physics Letters*, 65(11): 1334-1336 (12 September 1994).

Jin, R., G. Khitrova, D. Boggavarapu, H. M. Gibbs, S. W. Koch, M. S. Tobin, and R. P. Leavitt. "Physics of Semiconductor Vertical-Cavity Surface-Emitting Lasers," *Journal of Nonlinear Optical Physics and Materials* 4(1): 41-161 (1995).

Koch, S. W., N. Peyghambarian, and H. M. Gibbs. "Band-Edge Nonlinearities in Direct-Gap Semiconductors and their Application to Optical Bistability and Optical Computing," *Journal of Applied Physics* 63(2): R1-R11 (15 January 1988).

Kukhtarev, N. V. and G. V. Kovalenko. "Wavefront Reversal in Interband Absorption in Semiconductors," *Soviet Journal of Quantum Electronics* 10(4): 446-449 (April 1980).

Le, H. Q. and S. Di Cecca. "Ultrafast, Multi-THz-Detuning, Third-Order Frequency Conversion in Semiconductor Quantum-Well Waveguides," *IEEE Photonics Technology Letters*, 4(8): 878-880 (August 1992).

Lee, Wun-Shung, Sien Chi, Pochi Yeh, and Ragini Saxena. "Theory of Phase-Conjugate Oscillators. I," *Journal of the Optical Society of America B*, 7(8): 1411-1419 (August 1990).

Li, Hua, Tim L. Lucas, John G. McInerney, Malcolm W. Wright, and Robert A. Morgan. "Injection Locking Dynamics of Vertical Cavity Semiconductor Lasers Under Conventional and Phase Conjugate Injection," *IEEE Journal of Quantum Electronics*, 32(2): 227-235 (February 1996).

Liu, J. M. and T. B. Simpson. "Characterization of Fundamental Parameters of a Semiconductor Laser with an Injected Optical Probe," *IEEE Photonics Technology Letters*, 4(4): 380-382 (April 1993).

Liu, Jia-Ming and T. B. Simpson. "Four-Wave Mixing and Optical Modulation in a Semiconductor Laser," *IEEE Journal of Quantum Electronics*, 30(4): 957-965 (April 1994).

Lowry, C. W., F. Brown de Colstoun, A. E. Paul, G. Khitrova, H. M. Gibbs, J. W. Grantham, R. Jin, D. Boggavarapu, S. W. Koch, M. Sargent III, T. M. Brennan, and B. E. Hammons. "Acceleration of Coherent Transfer of Energy by Stimulated Emission and Absorption," *Physical Review Letters*, 71(10): 1534-1537 (6 September 1993).

Ludvigsen, Hanne and Erik Bødtker. "New Method for Self-Homodyne Laser Linewidth Measurements with a Short Delay Fiber," *Optics Communications* 110: 595-598 (1 September 1994).

MacLeod, H. A. *Thin Film Optical Filters* (2nd edition). New York: MacMillan Publishing Company, 1986.

Mecozzi, Antonio, Alessandro D'Ottavi, and Rongqing Hui. "Nearly Degenerate Four-Wave Mixing in Distributed Feedback Semiconductor Lasers Operating Above Threshold," *IEEE Journal of Quantum Electronics*, 29(6): 1477-1487 (June 1993).

Mecozzi, A., A. D'Ottavi, F. Cara Romeo, P. Spano, R. Dall'Ara, G. Guekos, and J. Eckner. "High Saturation Behavior of the Four-wave Mixing Signal in Semiconductor Amplifiers," *Applied Physics Letters* 66(10): 1184-1186 (6 March 1995).

Mecozzi, A., S. Scotti, A. D'Ottavi, E. Iannone, and P. Spano. "Four-Wave Mixing in Traveling-Wave Semiconductor Amplifiers," *IEEE Journal of Quantum Electronics*, 31(4): 689-699 (April 1995).

Middlemast, I., J. Sarma, K. A. Shore, A. I. Kucharska, E. D. Fletcher, and P. Blood. "Absorptive Bistability in Inhomogeneously Pumped Quantum Well Laser Diodes," *IEE Proceedings-J*, 38(5): 301-308 (October 1991).

Miller, D. A. B., D. S. Chemla, D. J. Eilenberger, P. W. Smith, A. C. Gossard, and W. T. Tsang. "Large Room-Temperature Optical Nonlinearity in GaAs/Ga_{1-x}Al_xAs Multiple Quantum Well Structure," *Applied Physics Letters* 41(8): 679-681 (15 October 1982).

Nakajima, Hisao, and Robert Frey. "Observation of Bistable Reflectivity of a Phase-Conjugated Signal Through Intracavity Nearly Degenerate Four-Wave Mixing," *Physical Review Letters*, 54(16): 1798-1801 (22 April 1985).

Nakajima, Hisao, and Robert Frey. "Intracavity Nearly Degenerate Four-wave Mixing in a (GaAl)As Semiconductor Laser," *Applied Physics Letters*, 47(8): 769-771 (15 October 1985).

Nakajima, Hisao, and Robert Frey. "Collinear Nearly Degenerate Four-Wave Mixing in Intracavity Amplifying Media," *IEEE Journal of Quantum Electronics*, QE-22(8): 1349-1354 (August 1986).

Nietzke, Rainer, Peter Panknin, Wolfgang Elsässer, and Ernst O. Göbel. "Four-Wave Mixing in GaAs/AlGaAs Semiconductor Lasers," *IEEE Journal of Quantum Electronics*, 25(6): 1399-1406 (June 1989).

Ohtsu, Motoichi, Isao Koshiishi, and Yasuaki Teramachi. "A Semiconductor Laser as a Stable Phase Conjugate Mirror for Linewidth Reduction of Another Semiconductor Laser," *Japanese Journal of Applied Physics* 29(11): L2060-L2062 (November 1990).

Osinski, Marek and Jens Buus. "Linewidth Broadening Factor in Semiconductor Lasers-An Overview," *IEEE Journal of Quantum Electronics* QE-23(1): 9-29 (January 1987).

Park, S. H., J. F. Morhange, A. D. Jeffery, R. A. Morgan, A. Chavez-Pirson, H. M. Gibbs, S. W. Koch, N. Peyghambarian, M. Derstine, A. C. Gossard, J. H. English, and W. Weigmann. "Measurements of Room-Temperature Band-Gap Resonant Optical Nonlinearities of GaAs/AlGaAs Multiple Quantum Wells and Bulk GaAs," *Applied Physics Letters* 52(15): 1201-1203 (11 April 1988).

Patterson, F. G. and J. C. Brock. "Correction of Optical Path Differences Using Phase Conjugation in Single-Mode Diode Lasers," *Optics Letters* 16(17): 1322-1324 (1 September 1991).

Paul, A. E., M. Lindberg, S. An, M. Sargent III, and S. W. Koch. "Quantum Theory of Nondegenerate Four-Wave Mixing in Semiconductors," *Physical Review A*, 42(3): 1725-1736 (1 August 1990).

Pepper, David M., Dan Fekete, and Amnon Yariv. "Observation of Amplified Phase-Conjugate Reflection and Optical Parametric Oscillation by Degenerate Four-wave Mixing in a Transparent Medium," *Applied Physics Letters* 33(1): 41-44 (1 July 1978).

Peters, Kurt M. *Design and Characterization of a Nonlinear Optical Switch*. MS thesis, AFIT/GEO/ENP/94D-05, School of Engineering, Air Force Institute of Technology, Wright-Patterson AFB, OH, December 1994.

Petitbon, Isabelle, Philippe Gallion, Guy Debarge, and Claude Chabran. "Locking Bandwidth and Relaxation Oscillations of an Injection-Locked Semiconductor Laser," *IEEE Journal of Quantum Electronics* 24(2): 148-154 (February 1988).

Provost, J. G. and R. Frey. "Cavity-Enhanced Highly Nondegenerate Four-Wave Mixing in GaAlAs Semiconductor Lasers," *Applied Physics Letters*, 55(6): 519-521 (7 August 1989).

Simpson, T. B. and J. M. Liu. "Phase and Amplitude Characteristics of Nearly-Degenerate Four-Wave Mixing in Fabry-Perot Semiconductor Lasers," *Journal of Applied Physics*, 73 (5): 2587-2589 (1 March 1993).

Simpson, T. B., J. M. Liu. "Spontaneous Emission, Nonlinear Optical Coupling, and Noise in Laser Diodes," *Optics Communications*, 112: 44-47 (1 November 1994).

Simpson, T. B., J. M. Liu, A. Gavrielides, V. Kovanis, and P. M. Alsing. "Period-Doubling Cascades and Chaos in a Semiconductor Laser with Optical Injection," *Physical Review A*, 51(5): 4181-4185 (May 1995).

Simpson, T. B., J. M. Liu, K. F. Huang, K. Tai, C. M. Clayton, A. Gavrielides, and V. Kovanis. "Cavity Enhancement of Resonant Frequencies in Semiconductor Lasers Subject to Optical Injection," *Physical Review A*, 52(6): R4348-R4351 (December 1995).

Simpson, T. B., J. M. Liu, and A. Gavrielides. "Small-Signal Analysis of Modulation Characteristics in a Semiconductor Laser Subject to Strong Optical Injection," *IEEE Journal of Quantum Electronics*, 32(8): 1456-1468 (August 1996).

Simpson, T. B. Personal Communication, June 1996 - September 1996.

Tiemeijer, L. F. "Effects of Nonlinear Gain on Four-Wave Mixing and Asymmetric Gain Saturation in a Semiconductor Laser Amplifier," *Applied Physics Letters*, 59(5): 499-501 (29 July 1991).

Turner, M. D. *Degenerate Four-Wave Mixing of Cr, Tm, Ho: YAG Laser Output at 2.1 mm in Semiconductor Compounds*. Ph.D. Dissertation, AFIT/DS/ENP/96-06, School of Engineering, Air Force Institute of Technology, Wright-Patterson AFB, OH, September 1996.

Vahala, Kerry J. and Michael A. Newkirk. "Parasitic-Free Modulation of Semiconductor Lasers," *IEEE Journal of Quantum Electronics*, 25(6): 1393-1398 (June 1989).

van Tartwijk, G. H. M., and D. Lenstra. "Semiconductor Lasers with Optical Injection and Feedback," *Quantum Semiclassical Optics* 7: 87-143 (1995).

Vinetskii, V. L., N. V. Kukharev, S. G. Odulov, and M. S. Soskin. "Dynamic Conversion of Light Beams by Phase-Shifted Free-Carrier Holograms," *Soviet Physics Technical Physics* 22(6): 729-732 (June 1977).

Westbrook, L. D. and M. J. Adams. "Linewidth Enhancement in Quantum Well Lasers," *Electronics Letters 23(23)*: 1223-1225 (5 November 1987).

Yariv, Amnon and David M. Pepper. "Amplified Reflection, Phase Conjugation, and Oscillation in Degenerate Four-Wave Mixing," *Optics Letters 1(1)*: 16-18 (July 1977).

Yee, W. M. and K. A. Shore. "Nearly Degenerate Four-Wave Mixing in Laser Diodes with Nonuniform Longitudinal Gain Distribution," *Journal of the Optical Society of America B 11(7)*: 1221-1228 (July 1994).

Yee, W. M. and K. A. Shore. "Enhanced Uniform Phase Conjugation in Two-Section Asymmetric Laser Diodes," *Optics Letters 19(24)*: 2128-2130 (15 December 1994).

Yee, W. M. and K. A. Shore. "Enhanced Wavelength Tunability in Asymmetric Gain-Levered Quantum-Well Semiconductor Lasers," *Journal of Lightwave Technology 13(4)*: 588-591 (April 1995).

Yu, S. F. "Dynamic Behavior of Vertical-Cavity Surface-Emitting Lasers," *IEEE Journal of Quantum Electronics 32(7)*: 1168-1179 (July 1996).

Zhao, Yang, Cunkai Wu, Pankaj Shah, M. K. Kim, L. Ralph Dawson. "Optical Phase Conjugation in InGaAs/GaAs Multiple Quantum Wells at 1.06 μm Wavelength," *Applied Physics Letters 63(3)*: 281-281 (19 July 1993).

Appendix A: FORTRAN Code for Asymmetric Cavity Model

```

PROGRAM FWMFDV
C*****
C This program solves the four-wave mixing problem in a semiconductor
C laser. The starting point are the first order differential equations
C from an article by Yee and Shore, "Nearly degenerate four-wave mixing
C in laser diodes with nonuniform longitudinal gain distribution,"
C JOSA B, vol. 11, no. 7, July 1994, p. 1221. The equation are 19,20,21.
C Converting to the real and imaginary parts, we then solve for the
C strong pump field using the PCIP approach mentioned in the article,
C and then solve for probe and conjugate using a finite difference
C approximation for the differential equations. This works as long as
C the equations are linear. If nonlinear (weak pump would cause this)
C then a relaxation approach to the finite difference equations can be
C used.
C*****
INTEGER M,ITER,N,NM
INTEGER V1,V2,V3,V4,V5
INTEGER OMEGAN,RATN,INJN,R1N,R2N
INTEGER SPUMP1,SPUMP2,SFIELD,SREFL,SSHOW,SLOG,SPHAS
PARAMETER (N=8,M=22,NM=176)
DOUBLE PRECISION L,R1,R2,ALPHA,N0,RAT,A,GAMMA,BETA,PHAS0,
+TAU,DEL,G0,OMEGA,C,INDEX,xl,xr,PHASET,INTIN,PI,AIN,TOL
DOUBLE PRECISION MX(N,N,M),MR(NM,NM),AA(23,NM)
DOUBLE PRECISION X(NM),Y(N,M),B(NM)
DOUBLE PRECISION A0RR(M),A0RI(M),A0FR(M),A0FI(M)
DOUBLE PRECISION OMEGA1,OMEGAD,RAT1,RATD,INJ1,INJD
DOUBLE PRECISION R11,R1D,R21,R2D
DOUBLE PRECISION Y1,Y2,Y3,Y4,Y5,Y6,Y7,Y8
DOUBLE PRECISION INJ
DOUBLE PRECISION KK0,KK1,KK2
DOUBLE PRECISION NBAR(M-1),GBAR(M-1)

c  COMMON /parms/L, R1,R2,ALPHA,N0,RAT,A,GAMMA,BETA,PHAS0,
c  +TAU,DEL,G0,OMEGA,C,INDEX,xl,xr,PHASET,INTIN,PI,AIN,TOL
COMMON /parms/ L,R1,R2,ALPHA,N0,RAT,A,GAMMA,BETA,PHAS0,
+TAU,DEL,G0,OMEGA,C,INDEX,xl,xr,PHASET,INTIN,PI,AIN,TOL
COMMON /parmx/KK0,KK1,KK2
COMMON /SWITCH/SPUMP1,SPUMP2,SFIELD,SREFL,SSHOW,SLOG,SPHAS

OPEN (UNIT=1,FILE='fwm.in',STATUS='UNKNOWN')
OPEN (UNIT=2,FILE='fwmfd.out',STATUS='NEW')
OPEN (UNIT=3,FILE='reflfd.out',STATUS='NEW')
OPEN (UNIT=4,FILE='pumpfd.out',STATUS='NEW')
OPEN (UNIT=6,FILE='reflfdp.out',STATUS='NEW')
OPEN (UNIT=7,FILE='reflfdi.out',STATUS='NEW')

C*** Read parameter data from external file *****
READ (1,17) ITER

```

```

READ (1,18) L
READ (1,19) R11,R1D,R1N
READ (1,19) R21,R2D,R2N
READ (1,18) ALPHA
READ (1,18) N0
READ (1,19) RAT1,RATD,RATN
READ (1,18) A
READ (1,18) GAMMA
READ (1,18) BETA
READ (1,18) TAU
READ (1,18) INTIN
READ (1,18) TOL
READ (1,18) BTOL
READ (1,18) AIN
READ (1,19) OMEGA1,OMEGAD,OMEGAN
READ (1,19) INJ1,INJD,INJN
READ (1,17) SPUMP1
READ (1,17) SPUMP2
READ (1,17) SFIELD
READ (1,17) SREFL
READ (1,17) SSHOW
READ (1,17) SLOG
READ (1,17) SPHAS
READ (1,18) KK0
READ (1,18) KK1
READ (1,18) KK2
16  FORMAT (4(D9.3))
17  FORMAT (24X,I5)
18  FORMAT (24X,D9.3)
19  FORMAT (24X,2(D10.4),I5)
CLOSE(1)

```

C***** Set Universal Constants *****

```

C=2.9979D+10
PI=3.1415926D+00
INDEX=3.6D+00

```

N0 = KK2*(KK1/KK0 - 1.0D0)

C*****Begin the big loop*****

```

DO 11115 V5=0,R2N
DO 11114 V4=0,R1N
DO 11113 V3=0,INJN
DO 11112 V2=0,RATN
DO 11111 V1=0,OMEGAN

```

C***** Establish parameter values for this loop*****

```

IF (SLOG.EQ.0) THEN
  OMEGA = OMEGA1 + DBLE(V1)*OMEGAD
ELSE
  QQ = (OMEGAD/OMEGA1)**(1.0d0/DBLE(OMEGAN))
  OMEGA = OMEGA1*(QQ**V1)
ENDIF
RAT=RAT1+DBLE(V2)*RATD

```

```

INJ = INJ1+DBLE(V3)*INJD
R1 = R11 + DBLE(V4)*R1D
R2 = R21 + DBLE(V5)*R2D
c   R2 = (0.9d0)*(0.8d0)/R1
C***** Print loop control and parameter data *****
IF (SSHOW.EQ.1) THEN
  WRITE (5,296) V1,OMEGAN,V2,RATN,V3,INJN,V4,R1N,V5,R2N
  WRITE (7,296) V1,OMEGAN,V2,RATN,V3,INJN,V4,R1N,V5,R2N
296  FORMAT (5(I4,I4))
ENDIF
C*** Calculate Constants for this Loop*****
c   G0=GAMMA*A*N0*(Rat-1.0d0)
C*** New way to calculate gain as function of RAT*****
G0 = KK0 - (KK1*KK2)/(KK2+RAT*N0)
C*****
DEL=L/DBLE(M-1)
xl=0.0d0
xr=L
C*****
PHASET=0.0d0
PHAS0=0.0d0
IF (SPHAS.EQ.1) THEN
  CALL pcip0(M,ITER,A0FR,A0FI,A0RR,A0RI,0.0d0,GBAR,NBAR)
  PHAS0=PHASET
  PHASET=0.0d0
  CALL pcip(M,ITER,A0FR,A0FI,A0RR,A0RI,INJ,GBAR,NBAR)
c   WRITE (5,6859) (PHASET-PHAS0)/(2.0d0*PI)
c 6859  FORMAT (D9.3)
  PHASET=PHAS0
  ELSE
    CALL pcip0(M,ITER,A0FR,A0FI,A0RR,A0RI,INJ,GBAR,NBAR)
  ENDIF
C*** Call MATRIX to create coefficient matrix for the diffeq **
  CALL matrix(N,M,MX,A0FR,A0FI,A0RR,A0RI,GBAR,NBAR)
C*** Convert matrix to the finite difference equations*****
  CALL convrt(N,M,NM,MX,MR)
C*** Convert finite difference matrix (MR) to band format (AA)**
  CALL DCRGRB(NM,MR,NM,11,11,AA,23)
  B(1) = SQRT(1.0D0-R1)
C*** Solve Ax=b *****
  CALL DLSLRB(NM,AA,23,11,11,B,1,X)
C   CALL DLSARG(NM,MR,NM,B,1,X)
C*** Convert x vector to y values *****
  CALL CONVY(X,Y,N,M,NM)
C*** Calculate reflectivities *****
  Y1=Y(1,M)
  Y2=Y(2,M)
  Y3=Y(3,1)
  Y4=Y(4,1)
  Y5=Y(5,M)
  Y6=Y(6,M)
  Y7=Y(7,1)
  Y8=Y(8,1)
  RP=(1.0d0-R1)*(Y3*Y3+Y4*Y4) + R1 - 2.0d0*SQRT(R1*(1.0d0-R1))*Y3

```

```

RC=(1.0d0-R1)*(Y7*Y7+Y8*Y8)
TP=(1.0d0-R2)*(Y1*Y1+Y2*Y2)
TC=(1.0d0-R2)*(Y5*Y5+Y6*Y6)

IF (INJ.NE.0.0d0) THEN
  RPUMP = ((A0RR(1)**2+A0RI(1)**2)*(1.0d0-R1) + INJ*INJ*R1 -
+ 2.0d0*INJ*A0RR(1)*SQRT(R1*(1.0d0-R1)))/(INJ**2)
  TPUMP = (1.0d0-R2)*(A0FR(M)**2 + A0FI(M)**2)/(INJ**2)
ENDIF

C*** Output results, depending on which switches are ****
C*** Print internal probe and conjugate field distribution ****
IF (SFIELD.EQ.1) THEN
c89  FORMAT (/,E11.4)
c  write (2,89) OMEGA
  DO 475 J=1,M
    write (2,487) dble(j-1)*DEL,(Y(I,J),I=1,N)
487  format (9(E12.5))
475  continue
ENDIF

C*** Print reflectivities and the varying parameters ****
IF (SREFL.EQ.1) THEN
  WRITE (3,787) RP,RC,TP,TC
  WRITE (6,788) OMEGA,RAT,INJ,R1,R2
787  FORMAT (4(E12.4))
788  FORMAT (5(E12.4))
ENDIF

C*** Print pump information, with or without internal fields ****
IF (SPUMP1.EQ.1) THEN
87  FORMAT (9(E13.5))
  write (4,87) OMEGA,RAT,INJ,R1,R2,RPUMP,TPUMP,A0FR(M),A0FI(M)
ENDIF
IF (SPUMP2.EQ.1) THEN
  DO 375 J=1,M
    write (4,387) dble(j-1)*DEL,a0fr(j),a0fi(j),a0rr(j),a0ri(j)
387  format (5(E13.5))
375  continue
ENDIF

11111 continue
11112 continue
11113 continue
11114 continue
11115 continue
  STOP
END

```

```
C*****  
C SUBROUTINE convy(X,Y,N,M,NM)  
C*****  
C Converts a vector of length N*M to a matrix of size N x M,  
C given both N and M.  
C*****  
DOUBLE PRECISION X(NM),Y(N,M)  
INTEGER I,K  
  
DO 401 I=1,N  
  DO 402 K=1,M  
    Y(I,K) = X((K-1)*N + I)  
402  CONTINUE  
401  CONTINUE  
  
RETURN  
END
```

```

C*****SUBROUTINE convert(N,M,NM,MX,MR)
C*****C This converts the 3D tensor MX (N x N x M) to the
C 2D matrix MR (N*M x N*M) in preparation for the
C finite difference technique. See handwritten documents
C for description of intermediate matrix T and the role
C of each counting index I,J,K,LL,P,Q.
C*****
INTEGER I,J,K,LL,P,Q,BEG,END,M,N,NM
INTEGER t1,t2,t3,t4
DOUBLE PRECISION MX(N,N,M),MR(NM,NM),T(NM,NM),H
DOUBLE PRECISION L, R1,R2,ALPHA,N0,RAT,A,GAMMA,BETA,PHAS0,
+TAU,DEL,G0,OMEGA,C,INDEX,xl,xr,PHASET,INTIN,PI,AIN,TOL

c  COMMON /parms/L, R1,R2,ALPHA,N0,RAT,A,GAMMA,BETA,
c  +TAU,DEL,G0,OMEGA,C,INDEX,xl,xr,PHASET,INTIN,PI,AIN,TOL
COMMON /parms/ L,R1,R2,ALPHA,N0,RAT,A,GAMMA,BETA,PHAS0,
+TAU,DEL,G0,OMEGA,C,INDEX,xl,xr,PHASET,INTIN,PI,AIN,TOL

c  OPEN (UNIT=55,FILE='tst.in',STATUS='UNKNOWN')
c  READ (55,545) t1,t2,t3,t4
c545 FORMAT (4(i5))

C*** Set up counting variables to put the elements in matrix***
H=DEL
BEG=N/2+1
END=NM-N/2
C*** Loop through elements of matrix T *****
DO 501 P=1,NM
  DO 502 Q=1,NM

C*** Zero the elements of the matrices T and MR *****
T(P,Q)=0.0d0
MR(P,Q)=0.0d0

C*** Formulas for the counting variable, based on P, Q, N *****
I=P-N*INT(REAL(P-1)/REAL(N))
J=Q-N*INT(REAL(Q-1)/REAL(N))
K=INT(REAL(P-1)/REAL(N))+1
LL=INT(REAL(Q-1)/REAL(N))+1

C*** Matrix is sparse, so only if LL=K or LL+1=K is there data.
C*** First the K = LL+1 case *****
IF (K.EQ.(LL+1)) THEN
  IF (I.EQ.J) THEN
    T(P,Q) = (-H/2.0d0)*MX(I,J,LL)-1.0d0
  ELSE
    T(P,Q) = (-H/2.0d0)*MX(I,J,LL)
  ENDIF
ENDIF

C*** Now the K = LL case *****

```

```

IF (K.EQ.LL) THEN
  IF (I.EQ.J) THEN
    T(P,Q) = (-H/2.0d0)*MX(I,J,LL)+1.0d0
  ELSE
    T(P,Q) = (-H/2.0d0)*MX(I,J,LL)
  ENDIF
ENDIF

502  CONTINUE
501  CONTINUE

C*** Now convert temporary matrix T to real matrix MR by a shift***
DO 601 P=BEG,END
  DO 602 Q=1,NM
    MR(P,Q)=T(P+4,Q)
602  CONTINUE
601  CONTINUE

C*** Fill in MR with boundary conditions at beginning and end *****
MR(1,1) = 1.0D0
MR(2,2) = 1.0D0
MR(3,5) = 1.0D0
MR(4,6) = 1.0D0
MR(1,3) = -SQRT(R1)
MR(2,4) = -SQRT(R1)
MR(3,7) = -SQRT(R1)
MR(4,8) = -SQRT(R1)

MR(NM-(N/2)+1,NM-N+1) = -SQRT(R2)*COS(PHASET)
MR(NM-(N/2)+1,NM-N+2) = SQRT(R2)*SIN(PHASET)
MR(NM-(N/2)+1,NM-N+3) = 1.0D0

MR(NM-(N/2)+2,NM-N+1) = -SQRT(R2)*SIN(PHASET)
MR(NM-(N/2)+2,NM-N+2) = -SQRT(R2)*COS(PHASET)
MR(NM-(N/2)+2,NM-N+4) = 1.0D0

MR(NM-(N/2)+3,NM-N+5) = -SQRT(R2)*COS(PHASET)
MR(NM-(N/2)+3,NM-N+6) = SQRT(R2)*SIN(PHASET)
MR(NM-(N/2)+3,NM-N+7) = 1.0D0

MR(NM-(N/2)+4,NM-N+5) = -SQRT(R2)*SIN(PHASET)
MR(NM-(N/2)+4,NM-N+6) = -SQRT(R2)*COS(PHASET)
MR(NM-(N/2)+4,NM-N+8) = 1.0D0

```

```

RETURN
END

```

```

C*****
C SUBROUTINE matrix (N,M,MX,A0FR,A0FI,A0RR,A0RI,GBAR,NBAR)
C*****
C Calculates the tensor MX describing the original
C differential equations. The first two indices, both with
C length N, describe the N variables. The third index of
C length M describes position along the cavity. The pumps
C change throughout the cavity, so the matrix does, too.
C*****
C
C INTEGER N,M,I,J,K
C DOUBLE PRECISION MX(N,N,M),X
C DOUBLE PRECISION B1,C1,B2,C2,PT,U,V,G,DETUN
C DOUBLE PRECISION K1,K2,K3,K4,K5,K6,K7,K8
C DOUBLE PRECISION Z1,Z2,Z3,Z4,Q1,Q2,Q3,Q4
C DOUBLE PRECISION A0RR(M),A0RI(M),A0FR(M),A0FI(M)
C DOUBLE PRECISION F1,F2,NB,GB,KK0,KK1,KK2,KKQ
C DOUBLE PRECISION L, R1,R2,ALPHA,N0,RAT,A,GAMMA,BETA,PHAS0,
C +TAU,DEL,G0,OMEGA,C,INDEX,xl,xr,PHASET,INTIN,PI,AIN,TOL
C DOUBLE PRECISION NBAR(M-1),GBAR(M-1)

c  COMMON /parms/ L, R1,R2,ALPHA,N0,RAT,A,GAMMA,BETA,
c  +TAU,DEL,G0,OMEGA,C,INDEX,xl,xr,PHASET,INTIN,PI,AIN,TOL
COMMON /parms/ L,R1,R2,ALPHA,N0,RAT,A,GAMMA,BETA,PHAS0,
+TAU,DEL,G0,OMEGA,C,INDEX,xl,xr,PHASET,INTIN,PI,AIN,TOL
COMMON /parmx/KK0,KK1,KK2

C*** Calculate pump field at position K in the cavity *****
DO 101 K = 1,M
  X=DBLE(K-1)*DEL
  B1=A0FR(K)
  C1=A0FI(K)
  B2=A0RR(K)
  C2=A0RI(K)

C*** Shorthand notation for various complicated quantities *****
PT = B1**2 + C1**2 + B2**2 + C2**2
C*****
C      F1 = RAT*N0-KK2*(1.0d0+PT)
C      F2 = 4*KK2*N0*(RAT+PT)
C      NB = (F1+SQRT(F1*F1+F2))/2.0D0
C      GB = KK0-(KK1*KK2)/(NB+KK2)
C*****
IF (K.NE.M) THEN
  NB = NBAR(K)
  GB = GBAR(K)
ELSE
  NB = NBAR(K-1)
  GB = GBAR(K-1)
ENDIF

KKQ = (KK1*KK2/(KK0*(KK2+NB)))**2
U = KKQ*(KKQ*PT+1.0d0)/((KKQ*PT+1.0d0)**2 + (TAU*OMEGA)**2)

```

```
V = KKQ*(TAU*OMEGA)/((KKQ*PT+1.0d0)**2 + (TAU*OMEGA)**2)
G = (GAMMA/2.0D0)*GB
DETUN=INDEX*OMEGA/C
```

```
K1 = B1*U+C1*V
K2 = C1*U-B1*V
K3 = B2*U+C2*V
K4 = C2*U-B2*V
K5 = B1*U-C1*V
K6 = C1*U+B1*V
K7 = B2*U-C2*V
K8 = C2*U+B2*V
```

```
Q1 = (B1+BETA*C1)*G
Q2 = (C1-BETA*B1)*G
Q3 = (B2+BETA*C2)*G
Q4 = (C2-BETA*B2)*G
```

```
Z1 = G - ALPHA/2.0d0
Z2 = G*BETA - DETUN
Z3 = G + ALPHA/2.0d0
Z4 = G*BETA + DETUN
```

C*** These are the differential equations, using the Jacobean form *****

```
MX(1,1,K) = -K1*Q1 - K2*Q2 + Z1
MX(1,2,K) = -K2*Q1 + K1*Q2 + Z2
MX(1,3,K) = -K3*Q1 - K4*Q2
MX(1,4,K) = -K4*Q1 + K3*Q2
MX(1,5,K) = -K5*Q1 + K6*Q2
MX(1,6,K) = -K6*Q1 - K5*Q2
MX(1,7,K) = -K7*Q1 + K8*Q2
MX(1,8,K) = -K8*Q1 - K7*Q2
```

```
MX(2,1,K) = -K1*Q2 + K2*Q1 - Z2
MX(2,2,K) = -K2*Q2 - K1*Q1 + Z1
MX(2,3,K) = -K3*Q2 + K4*Q1
MX(2,4,K) = -K4*Q2 - K3*Q1
MX(2,5,K) = -K5*Q2 - K6*Q1
MX(2,6,K) = -K6*Q2 + K5*Q1
MX(2,7,K) = -K7*Q2 - K8*Q1
MX(2,8,K) = -K8*Q2 + K7*Q1
```

```
MX(3,1,K) = K1*Q3 + K2*Q4
MX(3,2,K) = K2*Q3 - K1*Q4
MX(3,3,K) = K3*Q3 + K4*Q4 - Z1
MX(3,4,K) = K4*Q3 - K3*Q4 - Z2
MX(3,5,K) = K5*Q3 - K6*Q4
MX(3,6,K) = K6*Q3 + K5*Q4
MX(3,7,K) = K7*Q3 - K8*Q4
MX(3,8,K) = K8*Q3 + K7*Q4
```

```
MX(4,1,K) = K1*Q4 - K2*Q3
MX(4,2,K) = K2*Q4 + K1*Q3
MX(4,3,K) = K3*Q4 - K4*Q3 + Z2
```

$$MX(4,4,K) = K4*Q4 + K3*Q3 - Z1$$

$$MX(4,5,K) = K5*Q4 + K6*Q3$$

$$MX(4,6,K) = K6*Q4 - K5*Q3$$

$$MX(4,7,K) = K7*Q4 + K8*Q3$$

$$MX(4,8,K) = K8*Q4 - K7*Q3$$

$$MX(5,1,K) = -K1*Q1 + K2*Q2$$

$$MX(5,2,K) = -K2*Q1 - K1*Q2$$

$$MX(5,3,K) = -K3*Q1 + K4*Q2$$

$$MX(5,4,K) = -K4*Q1 - K3*Q2$$

$$MX(5,5,K) = -K5*Q1 - K6*Q2 + Z1$$

$$MX(5,6,K) = -K6*Q1 + K5*Q2 + Z4$$

$$MX(5,7,K) = -K7*Q1 - K8*Q2$$

$$MX(5,8,K) = -K8*Q1 + K7*Q2$$

$$MX(6,1,K) = -K1*Q2 - K2*Q1$$

$$MX(6,2,K) = -K2*Q2 + K1*Q1$$

$$MX(6,3,K) = -K3*Q2 - K4*Q1$$

$$MX(6,4,K) = -K4*Q2 + K3*Q1$$

$$MX(6,5,K) = -K5*Q2 + K6*Q1 - Z4$$

$$MX(6,6,K) = -K6*Q2 - K5*Q1 + Z1$$

$$MX(6,7,K) = -K7*Q2 + K8*Q1$$

$$MX(6,8,K) = -K8*Q2 - K7*Q1$$

$$MX(7,1,K) = K1*Q3 - K2*Q4$$

$$MX(7,2,K) = K2*Q3 + K1*Q4$$

$$MX(7,3,K) = K3*Q3 - K4*Q4$$

$$MX(7,4,K) = K4*Q3 + K3*Q4$$

$$MX(7,5,K) = K5*Q3 + K6*Q4$$

$$MX(7,6,K) = K6*Q3 - K5*Q4$$

$$MX(7,7,K) = K7*Q3 + K8*Q4 - Z1$$

$$MX(7,8,K) = K8*Q3 - K7*Q4 - Z4$$

$$MX(8,1,K) = K1*Q4 + K2*Q3$$

$$MX(8,2,K) = K2*Q4 - K1*Q3$$

$$MX(8,3,K) = K3*Q4 + K4*Q3$$

$$MX(8,4,K) = K4*Q4 - K3*Q3$$

$$MX(8,5,K) = K5*Q4 - K6*Q3$$

$$MX(8,6,K) = K6*Q4 + K5*Q3$$

$$MX(8,7,K) = K7*Q4 - K8*Q3 + Z4$$

$$MX(8,8,K) = K8*Q4 + K7*Q3 - Z1$$

101 CONTINUE

return

END

```

C*****
C SUBROUTINE pcip(M,ITER,A0FR,A0FI,A0RR,A0RI,INJ,GBAR,NBAR)
C*****
C This program implements the Piecewise Continuous Inversion
C Population (PCIP) solution to the internal pump field in a
C semiconductor laser. See Yee and Shore, JOSA B, vol. 11,
C no. 7, p 1221 for a description. The Middleast reference
C in the article is even more enlightening.
C*****

```

```

INTEGER M
DOUBLE PRECISION BR(M),CR(M),BF(M),CF(M)
DOUBLE PRECISION A0RR(M),A0RI(M),A0FR(M),A0FI(M)
DOUBLE PRECISION INR(M),INF(M)
DOUBLE PRECISION AIF(M-1),AIR(M-1),P(M-1),Q(M-1)
DOUBLE PRECISION NBAR(M-1),GBAR(M-1)
DOUBLE PRECISION x1,x2
DOUBLE PRECISION BC1A,BC1B,BC2A,BC2B,THETA
DOUBLE PRECISION F1,F2,KK0,KK1,KK2
INTEGER I,J,II,ITER,M1,M2
INTEGER SPUMP1,SPUMP2,SFIELD,SREFL,SSHOW
DOUBLE PRECISION L,R1,R2,ALPHA,N0,RAT,A,GAMMA,BETA,PHAS0,
+TAU,DEL,G0,OMEGA,C,INDEX,xl,xr,PHASET,INTIN,PI,AIN,TOL
DOUBLE PRECISION INJ,RPUMP,TPUMP

c  COMMON /parms/ L,R1,R2,ALPHA,N0,RAT,A,GAMMA,BETA,PHAS0,
c  +TAU,DEL,G0,OMEGA,C,INDEX,xl,xr,PHASET,INTIN,PI,AIN,TOL
COMMON /parms/ L,R1,R2,ALPHA,N0,RAT,A,GAMMA,BETA,PHAS0,
+TAU,DEL,G0,OMEGA,C,INDEX,xl,xr,PHASET,INTIN,PI,AIN,TOL
COMMON /parmx/KK0,KK1,KK2
COMMON /SWITCH/SPUMP1,SPUMP2,SFIELD,SREFL,SSHOW,SLOG,SPHAS

M1=10
M2=12
c  M1=1
c  M2=M-1

```

```

C*** Assign initial values for intensities ****

```

```

DO 20 I=1,M
BF(I) = 0.5*SQRT(INJ)*SQRT(1.0d0-R1)/(1.0d0-SQRT(R1*R2))
CF(I) = 0.0D+00
BR(I) = 0.5*SQRT(INJ)*SQRT(1.0d0-R1)/(1.0d0-SQRT(R1*R2))
CR(I) = 0.0D+00
INF(I) = 0.5*INJ*(1.0d0-R1)/(1.0d0-SQRT(R1*R2))**2
INR(I) = 0.5*INJ*(1.0d0-R1)/(1.0d0-SQRT(R1*R2))**2
20  CONTINUE

```

```

C*** Assign initial values for average intensities and gain values ****

```

```

DO 21 I=1,M-1
AIF(I) = INJ*(1.0d0-R1)/(1.0d0-SQRT(R1*R2))**2
AIR(I) = INJ*(1.0d0-R1)/(1.0d0-SQRT(R1*R2))**2
F1 = 0.0d0

```

```

F2 = 0.0d0
NBAR(I) = 0.0d0
GBAR(I) = 0.0d0
P(I) = 0.0d0
Q(I) = 0.0d0
21 CONTINUE
DO 2121 I=M1,M2
  F1 = RAT*N0-KK2*(1.0d0+AIF(I)+AIR(I))
  F2 = 4*KK2*N0*(RAT+(AIF(I)+AIR(I)))
  NBAR(I) = (F1+SQRT(F1*F1+F2))/2.0D0
  GBAR(I) = KK0-(KK1*KK2)/(NBAR(I)+KK2)
  P(I) = DEL*(GAMMA*GBAR(I)-ALPHA)/2.0d0
  Q(I) = DEL*GAMMA*BETA*GBAR(I)/2.0d0
2121 CONTINUE
C*** The Iteration Loop ****
DO 40 J=1,ITER
  IF (J.EQ.ITER) THEN
    WRITE (5,2872) ITER
 2872 FORMAT (' Not Converging in',I5,' Iterations')
  ENDIF
C*** Calculate Points in grid using formula ****
  THETA = 0.0d0
C*** Iterate forward fields and use results to modify gain ****
  DO 30 I=1,M-1
    IF ((I.GE.M1).AND.(I.LE.M2)) THEN
      c      F1 = RAT*N0-KK2*(1.0d0+AIF(I)+AIR(I))
      c      F2 = 4*KK2*N0*(RAT+(AIF(I)+AIR(I)))
      F1 = RAT*N0-KK2*(1.0d0+(KK1/KK0)*(AIF(I)+AIR(I)))
      F2 = 4*KK2*N0*(RAT+(KK1/KK0)*(AIF(I)+AIR(I)))
      NBAR(I) = (F1+SQRT(F1*F1+F2))/2.0D0
      GBAR(I) = KK0-(KK1*KK2)/(NBAR(I)+KK2)
      P(I) = DEL*(GAMMA*GBAR(I)-ALPHA)/2.0d0
      Q(I) = DEL*GAMMA*BETA*GBAR(I)/2.0d0
    ENDIF
    BF(I+1)=EXP(P(I))*(BF(I)*COS(Q(I))+CF(I)*SIN(Q(I)))
    CF(I+1)=EXP(P(I))*(CF(I)*COS(Q(I))-BF(I)*SIN(Q(I)))
    INF(I+1)=BF(I+1)*BF(I+1) + CF(I+1)*CF(I+1)
    IF (P(I).EQ.0.0D0) THEN
      AIF(I)=INF(I)
    ELSE
      AIF(I)=INF(I)*(EXP(2.0d0*P(I))-1.0d0)/(2.0d0*P(I))
    ENDIF
    THETA = THETA + BETA*DEL*GAMMA*GBAR(I)
 30 CONTINUE
C*** Calculate boundary values for convergence and set new
C*** values of reverse field at the end ****
  BC2A=SQRT(R2)*(BF(M)*COS(PHAS0)-CF(M)*SIN(PHAS0))-BR(M)
  BC2B=SQRT(R2)*(CF(M)*COS(PHAS0)+BF(M)*SIN(PHAS0))-CR(M)
  BR(M) = SQRT(R2)*(BF(M)*COS(PHAS0)-CF(M)*SIN(PHAS0))
  CR(M) = SQRT(R2)*(CF(M)*COS(PHAS0)+BF(M)*SIN(PHAS0))
  INR(M) = BR(M)*BR(M) + CR(M)*CR(M)
C*** Iterate the reverse fields and recalculate gain ****

```

```

THETA = 0.0d0
DO 31 I=M-1,1,-1
IF ((I.GE.M1).AND.(I.LE.M2)) THEN
  F1 = RAT*N0-KK2*(1.0d0+AIF(I)+AIR(I))
  F2 = 4*KK2*N0*(RAT+(AIF(I)+AIR(I)))
  F1 = RAT*N0-KK2*(1.0d0+(KK1/KK0)*(AIF(I)+AIR(I)))
  F2 = 4*KK2*N0*(RAT+(KK1/KK0)*(AIF(I)+AIR(I)))
  NBAR(I) = (F1+SQRT(F1*F1+F2))/2.0D0
  GBAR(I) = KK0-(KK1*KK2)/(NBAR(I)+KK2)
  P(I) = DEL*(GAMMA*GBAR(I)-ALPHA)/2.0d0
  Q(I) = DEL*GAMMA*BETA*GBAR(I)/2.0d0
ENDIF
BR(I)=EXP(P(I))*(BR(I+1)*COS(Q(I))+CR(I+1)*SIN(Q(I)))
CR(I)=EXP(P(I))*(CR(I+1)*COS(Q(I))-BR(I+1)*SIN(Q(I)))
INR(I)=BR(I)*BR(I) + CR(I)*CR(I)
IF (P(I).EQ.0.0D0) THEN
  AIR(I)=INR(I+1)
ELSE
  AIR(I)=INR(I+1)*(EXP(2.0d0*P(I))-1.0d0)/(2.0d0*P(I))
ENDIF
THETA = THETA + BETA*DEL*GAMMA*GBAR(I)
31  CONTINUE

```

```

C*** Calculate boundary values at beginning and reset forward field ****
BC1A = SQRT(R1)*BR(1) + SQRT(1.0d0-R1)*INJ - BF(1)
BC1B = SQRT(R1)*CR(1) - CF(1)
BF(1) = SQRT(R1)*BR(1) + SQRT(1.0d0-R1)*INJ
CF(1) = SQRT(R1)*CR(1)
INF(1) = BF(1)*BF(1) + CF(1)*CF(1)

```

```

C*** Check for convergence and exit if within tolerance ****
IF ((ABS(BC1A).LT.TOL).AND.(ABS(BC1B).LT.TOL).AND.
+ (ABS(BC2A).LT.TOL).AND.(ABS(BC2B).LT.TOL)) THEN
  GO TO 50
ENDIF

```

```
40  CONTINUE
```

```
50  CONTINUE
```

```
C*** Put results in the A0** matrixes for use by other routines ****
```

```

DO 78 I = 1,M
  A0FR(I) = BF(I)
  A0FI(I) = CF(I)
  A0RR(I) = BR(I)
  A0RI(I) = CR(I)
78  CONTINUE

```

```
PHASET = THETA
```

```

RETURN
END

```

```

C*****
C SUBROUTINE pcip0(M,ITER,A0FR,A0FI,A0RR,A0RI,INJ,GBAR,NBAR)
C*****
C This program implements the Piecewise Continuous Inversion
C Population (PCIP) solution to the internal pump field in a
C semiconductor laser. See Yee and Shore, JOSA B, vol. 11,
C no. 7, p 1221 for a description. The Middlemast reference
C in the article is even more enlightening.
C*****

```

```

INTEGER M
DOUBLE PRECISION BR(M),CR(M),BF(M),CF(M)
DOUBLE PRECISION A0RR(M),A0RI(M),A0FR(M),A0FI(M)
DOUBLE PRECISION INR(M),INF(M)
DOUBLE PRECISION AIF(M-1),AIR(M-1),P(M-1),Q(M-1)
DOUBLE PRECISION NBAR(M-1),GBAR(M-1)
DOUBLE PRECISION x1,x2
DOUBLE PRECISION BC1A,BC1B,BC2A,BC2B,THETA
DOUBLE PRECISION F1,F2,KK0,KK1,KK2
INTEGER I,J,II,ITER,M1,M2
INTEGER SPUMP1,SPUMP2,SFIELD,SREFL,SSHOW
DOUBLE PRECISION L, R1,R2,ALPHA,N0,RAT,A,GAMMA,BETA,PHAS0,
+TAU,DEL,G0,OMEGA,C,INDEX,xl,xr,PHASET,INTIN,PI,AIN,TOL
DOUBLE PRECISION INJ,RPUMP,TPUMP
c  COMMON /parms/ L,R1,R2,ALPHA,N0,RAT,A,GAMMA,BETA,PHAS0,
c  +TAU,DEL,G0,OMEGA,C,INDEX,xl,xr,PHASET,INTIN,PI,AIN,TOL
COMMON /parms/ L,R1,R2,ALPHA,N0,RAT,A,GAMMA,BETA,PHAS0,
+TAU,DEL,G0,OMEGA,C,INDEX,xl,xr,PHASET,INTIN,PI,AIN,TOL
COMMON /parmx/KK0,KK1,KK2
COMMON /SWITCH/SPUMP1,SPUMP2,SFIELD,SREFL,SSHOW,SLOG,SPHAS

M1=10
M2=12
c  M1=1
c  M2=M-1

```

```

C*** Assign initial values for intensities *****
DO 20 I=1,M
  BF(I) = 0.5*SQRT(INJ)*SQRT(1.0d0-R1)/(1.0d0-SQRT(R1*R2))
  CF(I) = 0.0D+00
  BR(I) = 0.5*SQRT(INJ)*SQRT(1.0d0-R1)/(1.0d0-SQRT(R1*R2))
  CR(I) = 0.0D+00
  INF(I) = 0.5*INJ*(1.0d0-R1)/(1.0d0-SQRT(R1*R2))**2
  INR(I) = 0.5*INJ*(1.0d0-R1)/(1.0d0-SQRT(R1*R2))**2
20  CONTINUE

```

```

C*** Assign initial values for average intensities and gain values *****
DO 21 I=1,M-1
  AIF(I) = INJ*(1.0d0-R1)/(1.0d0-SQRT(R1*R2))**2
  AIR(I) = INJ*(1.0d0-R1)/(1.0d0-SQRT(R1*R2))**2
  F1 = 0.0d0

```

```

F2 = 0.0d0
NBAR(I) = 0.0d0
GBAR(I) = 0.0d0
P(I) = 0.0d0
Q(I) = 0.0d0
21 CONTINUE
DO 2121 I=M1,M2
  F1 = RAT*N0-KK2*(1.0d0+AIF(I)+AIR(I))
  F2 = 4*KK2*N0*(RAT+(AIF(I)+AIR(I)))
  NBAR(I) = (F1+SQRT(F1*F1+F2))/2.0D0
  GBAR(I) = KK0-(KK1*KK2)/(NBAR(I)+KK2)
  P(I) = DEL*(GAMMA*GBAR(I)-ALPHA)/2.0d0
  Q(I) = DEL*GAMMA*BETA*GBAR(I)/2.0d0
2121 CONTINUE
C*** The Iteration Loop ****
DO 40 J=1,ITER
  IF (J.EQ.ITER) THEN
    WRITE (5,2872) ITER
  ENDIF
2872  FORMAT (' Not Converging in',I5,' Iterations')
C*** Calculate Points in grid using formula ****
  THETA = 0.0d0
C*** Iterate forward fields and use results to modify gain ****
  DO 30 I=1,M-1
    IF ((I.GE.M1).AND.(I.LE.M2)) THEN
      c   F1 = RAT*N0-KK2*(1.0d0+AIF(I)+AIR(I))
      c   F2 = 4*KK2*N0*(RAT+(AIF(I)+AIR(I)))
      F1 = RAT*N0-KK2*(1.0d0+(KK1/KK0)*(AIF(I)+AIR(I)))
      F2 = 4*KK2*N0*(RAT+(KK1/KK0)*(AIF(I)+AIR(I)))
      NBAR(I) = (F1+SQRT(F1*F1+F2))/2.0D0
      GBAR(I) = KK0-(KK1*KK2)/(NBAR(I)+KK2)
      P(I) = DEL*(GAMMA*GBAR(I)-ALPHA)/2.0d0
      Q(I) = DEL*GAMMA*BETA*GBAR(I)/2.0d0
    ENDIF
    BF(I+1)=EXP(P(I))*(BF(I)*COS(Q(I))+CF(I)*SIN(Q(I)))
    CF(I+1)=EXP(P(I))*(CF(I)*COS(Q(I))-BF(I)*SIN(Q(I)))
    INF(I+1)=BF(I+1)*BF(I+1) + CF(I+1)*CF(I+1)
    IF (P(I).EQ.0.0D0) THEN
      AIF(I)=INF(I)
    ELSE
      AIF(I)=INF(I)*(EXP(2.0d0*P(I))-1.0d0)/(2.0d0*P(I))
    ENDIF
    THETA = THETA + BETA*DEL*GAMMA*GBAR(I)
30   CONTINUE
C*** Calculate boundary values for convergence and set new
C*** values of reverse field at the end ****
  BC2A=SQRT(R2)*(BF(M)*COS(THETA)-CF(M)*SIN(THETA))-BR(M)
  BC2B=SQRT(R2)*(CF(M)*COS(THETA)+BF(M)*SIN(THETA))-CR(M)
  BR(M) = SQRT(R2)*(BF(M)*COS(THETA)-CF(M)*SIN(THETA))
  CR(M) = SQRT(R2)*(CF(M)*COS(THETA)+BF(M)*SIN(THETA))
  INR(M) = BR(M)*BR(M) + CR(M)*CR(M)
C*** Iterate the reverse fields and recalculate gain ****

```

```

THETA = 0.0d0
DO 31 I=M-1,1,-1
IF ((I.GE.M1).AND.(I.LE.M2)) THEN
  c   F1 = RAT*N0-KK2*(1.0d0+AIF(I)+AIR(I))
  c   F2 = 4*KK2*N0*(RAT+(AIF(I)+AIR(I)))
  F1 = RAT*N0-KK2*(1.0d0+(KK1/KK0)*(AIF(I)+AIR(I)))
  F2 = 4*KK2*N0*(RAT+(KK1/KK0)*(AIF(I)+AIR(I)))
  NBAR(I) = (F1+SQRT(F1*F1+F2))/2.0D0
  GBAR(I) = KK0-(KK1*KK2)/(NBAR(I)+KK2)
  P(I) = DEL*(GAMMA*GBAR(I)-ALPHA)/2.0d0
  Q(I) = DEL*GAMMA*BETA*GBAR(I)/2.0d0
  ENDIF
  BR(I)=EXP(P(I))*(BR(I+1)*COS(Q(I))+CR(I+1)*SIN(Q(I)))
  CR(I)=EXP(P(I))*(CR(I+1)*COS(Q(I))-BR(I+1)*SIN(Q(I)))
  INR(I)=BR(I)*BR(I) + CR(I)*CR(I)
  IF (P(I).EQ.0.0D0) THEN
    AIR(I)=INR(I+1)
  ELSE
    AIR(I)=INR(I+1)*(EXP(2.0d0*P(I))-1.0d0)/(2.0d0*P(I))
  ENDIF
  THETA = THETA + BETA*DEL*GAMMA*GBAR(I)
31  CONTINUE

```

```

C*** Calculate boundary values at beginning and reset forward field *****
BC1A = SQRT(R1)*BR(1) + SQRT(1.0d0-R1)*INJ - BF(1)
BC1B = SQRT(R1)*CR(1) - CF(1)
BF(1) = SQRT(R1)*BR(1) + SQRT(1.0d0-R1)*INJ
CF(1) = SQRT(R1)*CR(1)
INF(1) = BF(1)*BF(1) + CF(1)*CF(1)

```

```

C*** Check for convergence and exit if within tolerance *****
IF ((ABS(BC1A).LT.TOL).AND.(ABS(BC1B).LT.TOL).AND.
+ (ABS(BC2A).LT.TOL).AND.(ABS(BC2B).LT.TOL)) THEN
  GO TO 50
ENDIF

```

```

40  CONTINUE
50  CONTINUE

```

```

C*** Put results in the A0** matrixes for use by other routines *****
DO 78 I = 1,M
  A0FR(I) = BF(I)
  A0FI(I) = CF(I)
  A0RR(I) = BR(I)
  A0RI(I) = CR(I)
78  CONTINUE

```

```

PHASET = THETA

RETURN
END

```

Appendix B: MathCad Document for Analytic Solution

This computes an analytic (mostly) solution to the problem of four wave mixing (FWM) in a semiconductor laser. The analytic solution exists only for a very special case, where BETA = 0. We also have to assume a pump intensity that does NOT vary in z, which is close to true for highly reflective mirrors. In these cases, the eight first order differential equations have constant coefficients, and we can use matrix methods to solve them analytically. See Schaum's outline on Theory and Problem of Modern Introductory Differential Equations for a good description of the matrix method. While in principle an analytic solution, actually finding the solutions would be a nightmare. So rather than writing the matrices analytically, I've treated them numerically and inverted them numerically.

First, read in the data from the FWMIN file, which is the data input file for the FORTRAN program with the labels removed. Then assign variables based on this input data. The names closely match the names in the FORTRAN program.

```

Data := READPRN(fwmin)
L := Data1      R1 := Data2      R2 := Data3      Alpha := Data4      Rat := Data6      Γ := Data8      b := Data9
L = 2.5·10-4    R1 = 0.99      R2 = 0.99      Alpha = 20      Rat = 2.4      Γ = 1      b = 0
τ := Data10     Ω := Data15     K0 := Data24     K1 := Data25     K2 := Data26
τ = 1·10-9      Ω = 6.28·109  K0 = 2·104    K1 = 2.034·104  K2 = 6.557·1019

```

Now assign some global variables.

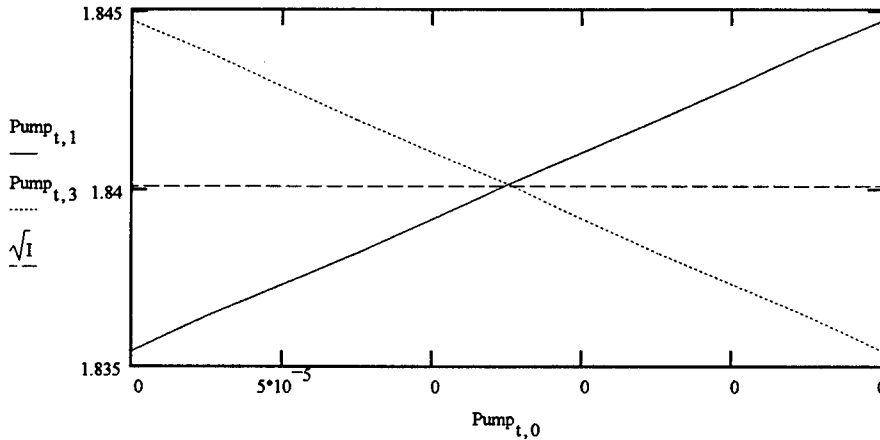
$$n := 3.6 \quad c := 2.9979 \cdot 10^{10}$$

Now create variables for the calculation, based on the input constants. N0 is the transparency carrier density, N is the injected carrier density with no field, and g0 is the corresponding small signal gain. Nsat is the carrier density required to saturate the gain to equal the losses. I is the intensity required to produce Nsat.

$$\begin{aligned}
N0 &:= K2 \cdot \left(\frac{K1}{K0} - 1 \right) & N &:= Rat \cdot N0 & g0 &:= K0 - \frac{K1 \cdot K2}{K2 + N} \\
N0 &= 1.115 \cdot 10^{18} & N &= 2.675 \cdot 10^{18} & g0 &= 457.341 & Γ \cdot g0 \cdot L &= 0.114 & Alpha \cdot L &= 0.005 \\
Nsat &:= -K2 + \frac{K1 \cdot K2}{K0 - \frac{\Alpha}{\Gamma} + \frac{\ln(R1 \cdot R2)}{2 \cdot L \cdot \Gamma}} & I &:= \frac{(K2 + Nsat) \cdot ((N - Nsat) \cdot K0)}{2 \cdot K1 \cdot K2 \cdot (Nsat - N0)} & g &:= K0 - \frac{K1 \cdot K2}{K2 + Nsat} \\
Nsat &= 1.316 \cdot 10^{18} & I &= 3.386 & g \cdot \Gamma &= 60.201
\end{aligned}$$

Read in the pump intensity information from the full model for comparison. The plot shows the analytic solution (I) is equal to the average of the forward and backward pump solutions from the full model.

Pump := READPRN(pumpfdout) T := rows(Pump) t := 0..T-1



Fill out the matrix representing the set of 8 differential equations. The original equation is of the form $y' = Dy$, where y is the vector of field amplitudes, y' is the vector of field amplitude derivatives (wrt z) and D is the matrix of constant coefficients. The quantities are defined the same as the full model. B is the field amplitude of the forward and backward pump waves. Since $BETA=0$, there is no imaginary part to the field ($C=0$).

$$B := \sqrt{I} \quad u := \frac{1 + 2B^2}{(1 + 2B^2)^2 + (\Omega \cdot \tau)^2} \quad v := \frac{\Omega \cdot \tau}{(1 + 2B^2)^2 + (\Omega \cdot \tau)^2}$$

$$B = 1.84 \quad u = 0.078 \quad v = 0.063 \quad n \cdot \frac{\Omega}{c} = 0.754$$

$$\alpha := \left(g - g \cdot u \cdot B^2 \right) \cdot \frac{\Gamma}{2} - \left(\frac{\text{Alpha}}{2} \right) \quad \beta := \frac{\Gamma}{2} \cdot g \cdot B^2 \cdot v - n \cdot \frac{\Omega}{c} \quad \mu := \frac{\Gamma}{2} \cdot g \cdot u \cdot B^2 \quad v := \frac{\Gamma}{2} \cdot g \cdot v \cdot B^2$$

$$\alpha = 12.167 \quad \beta = 5.657 \quad \mu = 7.933 \quad v = 6.411$$

$$D := \begin{bmatrix} \alpha & \beta & -\mu & v & -\mu & -v & -\mu & -v \\ -\beta & \alpha & -v & -\mu & -v & \mu & -v & \mu \\ \mu & -v & -\alpha & -\beta & \mu & v & \mu & v \\ v & \mu & \beta & -\alpha & v & -\mu & v & -\mu \\ -\mu & v & -\mu & v & \alpha & -\beta & -\mu & -v \\ v & \mu & v & \mu & \beta & \alpha & v & -\mu \\ \mu & -v & \mu & -v & \mu & v & -\alpha & \beta \\ -v & -\mu & -v & -\mu & -v & \mu & -\beta & -\alpha \end{bmatrix} \quad D = \begin{bmatrix} 12.167 & 5.657 & -7.933 & 6.411 & -7.933 & -6.411 & -7.933 & -6.411 \\ -5.657 & 12.167 & -6.411 & -7.933 & -6.411 & 7.933 & -6.411 & 7.933 \\ 7.933 & -6.411 & -12.167 & -5.657 & 7.933 & 6.411 & 7.933 & 6.411 \\ 6.411 & 7.933 & 5.657 & -12.167 & 6.411 & -7.933 & 6.411 & -7.933 \\ -7.933 & 6.411 & -7.933 & 6.411 & 12.167 & -5.657 & -7.933 & -6.411 \\ 6.411 & 7.933 & 6.411 & 7.933 & 5.657 & 12.167 & 6.411 & -7.933 \\ 7.933 & -6.411 & 7.933 & -6.411 & 7.933 & 6.411 & -12.167 & 5.657 \\ -6.411 & -7.933 & -6.411 & -7.933 & -6.411 & 7.933 & -5.657 & -12.167 \end{bmatrix}$$

Get the eigenvalues and eigenvectors and check for orthogonality and linear independence of the eigenvectors.

$\lambda\lambda := \text{eigvals}(D)$ $\lambda := \text{sort}(\lambda\lambda)$

$$\lambda\lambda = \begin{bmatrix} -12.992 + 19.592i \\ -12.992 - 19.592i \\ 12.992 + 19.592i \\ 12.992 - 19.592i \\ 20.101 + 0.754i \\ 20.101 - 0.754i \\ -20.101 + 0.754i \\ -20.101 - 0.754i \end{bmatrix} \quad \lambda = \begin{bmatrix} -20.101 + 0.754i \\ -20.101 - 0.754i \\ -12.992 + 19.592i \\ -12.992 - 19.592i \\ 12.992 + 19.592i \\ 12.992 - 19.592i \\ 20.101 - 0.754i \\ 20.101 + 0.754i \end{bmatrix}$$

$w := 0..7$ $q := 0..7$ $EVec^{<w>} := \text{eigenvec}(D, \lambda_w)$ $\text{Dot}_{w,q} := EVec^{<w>} \cdot \overline{EVec^{<q>}}$

$$\lambda = \begin{bmatrix} -20.101 + 0.754i \\ -20.101 - 0.754i \\ -12.992 + 19.592i \\ -12.992 - 19.592i \\ 12.992 + 19.592i \\ 12.992 - 19.592i \\ 20.101 - 0.754i \\ 20.101 + 0.754i \end{bmatrix} \quad \text{Dot} = \begin{bmatrix} 1 & 0 & 0 & 0 & 0 & 0 & 0 & 0 \\ 0 & 1 & 0 & 0 & 0 & 0 & 0 & 0 \\ 0 & 0 & 1 & 0 & 0 & -0.151 - 0.034i & 0 & 0 \\ 0 & 0 & 0 & 1 & -0.151 + 0.034i & 0 & 0 & 0 \\ 0 & 0 & 0 & -0.151 - 0.034i & 1 & 0 & 0 & 0 \\ 0 & 0 & -0.151 + 0.034i & 0 & 0 & 1 & 0 & 0 \\ 0 & 0 & 0 & 0 & 0 & 0 & 1 & 0 \\ 0 & 0 & 0 & 0 & 0 & 0 & 0 & 1 \end{bmatrix}$$

$$|D| = 4.999 \cdot 10^{10} \quad |EVec| = -0.976$$

Since the determinant of EVec is nonzero, the eigenvectors are linearly independent. However, they are not orthogonal, since the matrix of their dot products (Dot) has nondiagonal elements.

Now calculate the rotation matrix and make sure it works by seeing if it transforms the D matrix into a diagonal matrix with eigenvalues.

$LL_{w,q} := \text{if}(w=q, \lambda_w, 0)$ $U := EVec^{-1}$

Now solve the differential equations using the method derived by hand. This will use a lot of index variables, so assign them all right now.

$$i := 0..7 \quad j := 0..7 \quad k := 0..3 \quad n := 0..3 \quad M := 10 \quad m := 0..M \quad z_m := \frac{m}{M} \cdot L$$

Since this is a boundary value problem, some numerical iterations are required. We'll use the terminology and approach for a shooting algorithm described in Numerical Recipes. The vector v represents the freely chosen initial conditions, which translates into the vector y with the appropriately restricted initial conditions. Then we'll calculate a vector y at the end of the laser and create a vector f with the boundary conditions. If we've chosen well, $f = 0$. If not, go through the process described in Numerical Recipes to change the initial guess until $f = 0$. With a set of linear differential equations, only one iteration is required so do it manually.

$$v_0 := \begin{bmatrix} 0.1 \\ 0.1 \\ 0.1 \\ 0.1 \end{bmatrix} \quad v := v_0 + \begin{bmatrix} 1.811 \\ 131.634 \\ 1.861 \\ 134.709 \end{bmatrix} \quad v = \begin{bmatrix} 1.911 \\ 131.734 \\ 1.961 \\ 134.809 \end{bmatrix}$$

These are the initial guesses. The blind guess (v_0) is augmented by a dv obtained from the first iterations.

The S vector and T matrix represent the transformation of the initial guesses (v) into a valid set of initial values for vector y , called y_0 .

$$T := \begin{bmatrix} \sqrt{R1} & 0 & 0 & 0 \\ 0 & \sqrt{R1} & 0 & 0 \\ 1 & 0 & 0 & 0 \\ 0 & 1 & 0 & 0 \\ 0 & 0 & \sqrt{R1} & 0 \\ 0 & 0 & 0 & \sqrt{R1} \\ 0 & 0 & 1 & 0 \\ 0 & 0 & 0 & 1 \end{bmatrix} \quad S := \begin{bmatrix} \sqrt{1 - R1} \\ 0 \\ 0 \\ 0 \\ 0 \\ 0 \\ 0 \\ 0 \end{bmatrix} \quad y_0 := T \cdot v + S \quad y_0 = \begin{bmatrix} 2.001 \\ 131.074 \\ 1.911 \\ 131.734 \\ 1.951 \\ 134.133 \\ 1.961 \\ 134.809 \end{bmatrix}$$

Now use the analytical results derived by hand to calculate the value of y at every z step. The method transforms initial values (y_0) to the eigenvector basis (Y_0), then propagates along z to get Y , then transforms Y back to original basis (y).

$$Y_0 := U \cdot y_0$$

$$Y_{i,m} := Y_0 \cdot \exp(\lambda_i \cdot z_m)$$

$$y := U^{-1} \cdot Y$$

Now calculate the parameters for analyzing the error and changing initial condition. Again, the nomenclature follows Numerical Recipes for the most part. The matrix W is the Jacobian, T is just a shorthand way of writing the initial relation between v and y_0 , and F is the discrepancy vector with the boundary conditions at the end.

$$F := \begin{bmatrix} y_{2,M} - \sqrt{R2} \cdot y_{0,M} \\ y_{3,M} - \sqrt{R2} \cdot y_{1,M} \\ y_{6,M} - \sqrt{R2} \cdot y_{4,M} \\ y_{7,M} - \sqrt{R2} \cdot y_{5,M} \end{bmatrix}$$

$$W_{0,n} := \sum_j \sum_k \left[(U^{-1})_{2,j} - (U^{-1})_{0,j} \cdot \sqrt{R2} \right] \cdot U_{j,k} \cdot T_{k,n} \cdot \exp(\lambda_j \cdot L)$$

$$W_{1,n} := \sum_j \sum_k \left[(U^{-1})_{3,j} - (U^{-1})_{1,j} \cdot \sqrt{R2} \right] \cdot U_{j,k} \cdot T_{k,n} \cdot \exp(\lambda_j \cdot L)$$

$$W_{2,n} := \sum_j \sum_k \left[(U^{-1})_{6,j} - (U^{-1})_{4,j} \cdot \sqrt{R2} \right] \cdot U_{j,k} \cdot T_{k,n} \cdot \exp(\lambda_j \cdot L)$$

$$W_{3,n} := \sum_j \sum_k \left[(U^{-1})_{7,j} - (U^{-1})_{5,j} \cdot \sqrt{R2} \right] \cdot U_{j,k} \cdot T_{k,n} \cdot \exp(\lambda_j \cdot L)$$

$$dv := (W^{-1}) \cdot F$$

Now look at the results. If F is not close enough to zero, take the results from dv and use it to modify the guess as many times as necessary. This is a linear problem, so it should only take one iteration to get within roundoff error.

$$v = \begin{bmatrix} 1.911 \\ 131.734 \\ 1.961 \\ 134.809 \end{bmatrix} \quad F = \begin{bmatrix} -1.916 \cdot 10^{-6} \\ 9.508 \cdot 10^{-6} \\ -1.89 \cdot 10^{-6} \\ -9.603 \cdot 10^{-6} \end{bmatrix} \quad dv = \begin{bmatrix} -3.452 \cdot 10^{-4} + 6.16 \cdot 10^{-11} i \\ -3.997 \cdot 10^{-4} - 7.399 \cdot 10^{-11} i \\ -9.334 \cdot 10^{-5} - 6.139 \cdot 10^{-11} i \\ 4.668 \cdot 10^{-4} - 7.449 \cdot 10^{-11} i \end{bmatrix}$$

$$Rp := (1 - R1) \cdot \left[(y_{2,0})^2 + (y_{3,0})^2 \right] + R1 - 2 \cdot \sqrt{R1 \cdot (1 - R1)} \cdot y_{2,0} \quad Rp = 174.185$$

$$Rc := (1 - R1) \cdot \left[(y_{6,0})^2 + (y_{7,0})^2 \right] \quad Rc = 181.773$$

$$Tp := (1 - R2) \cdot \left[(y_{0,M})^2 + (y_{1,M})^2 \right] \quad Tp = 173.577$$

$$Tc := (1 - R2) \cdot \left[(y_{4,M})^2 + (y_{5,M})^2 \right] \quad Tc = 181.773$$

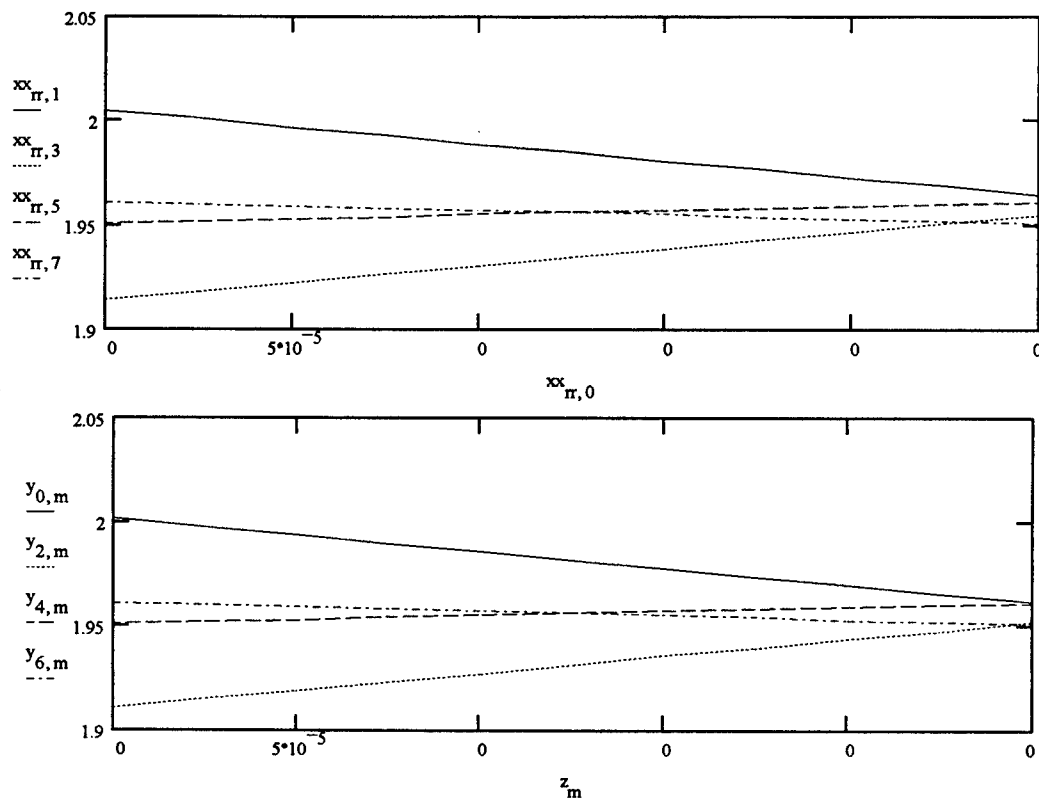
Read in the results for reflectivity and transmissivity from the full model for comparison.

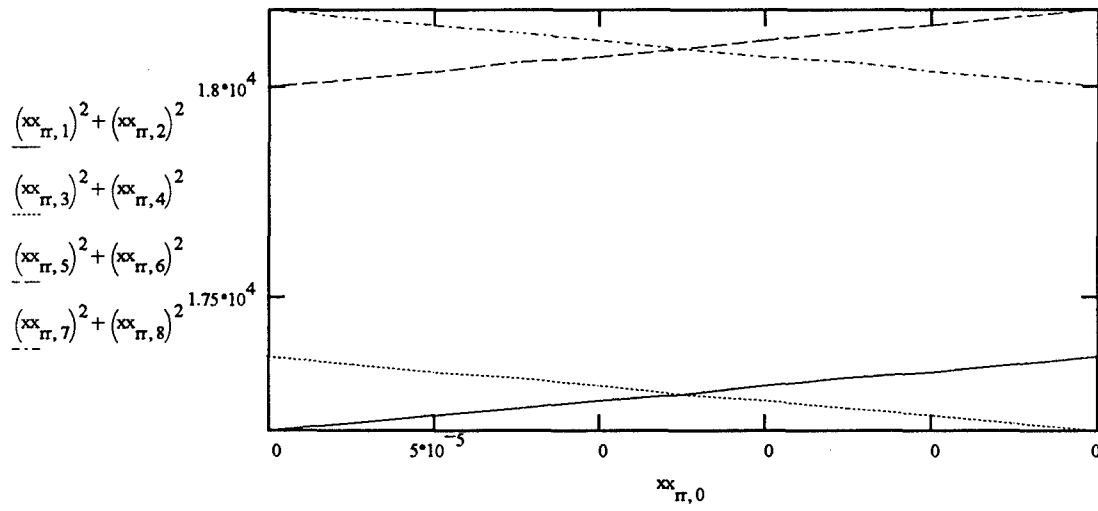
$$REF := READPRN(REFL)$$

$$REF = (174.2 \ 181.8 \ 173.6 \ 181.8)$$

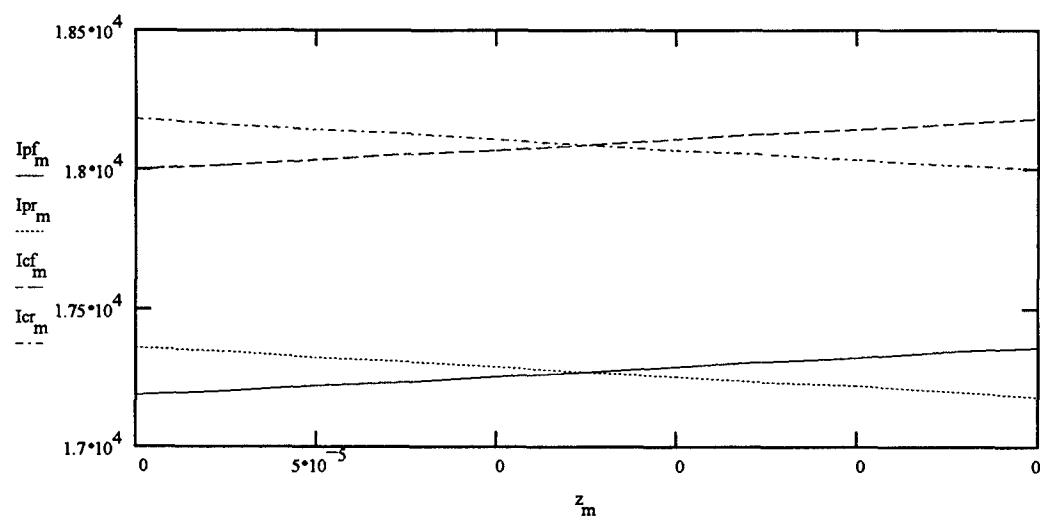
Now read in the results for the internal probe and conjugate fields from the full numerical solution to the problem for comparison.

```
xx:=READPRN(fwmfdout)      RR:=rows(xx)-1      SS:=cols(xx)-1      rr:=0..RR ss:=0..SS      f:=1..8
```





$$Ipf_m := (y_{0,m})^2 + (y_{1,m})^2 \quad Ipr_m := (y_{2,m})^2 + (y_{3,m})^2 \quad Icf_m := (y_{4,m})^2 + (y_{5,m})^2 \quad Icr_m := (y_{6,m})^2 + (y_{7,m})^2$$



Vita

Major Gregory J. Vansuch [REDACTED] of American parents at [REDACTED]. He graduated from Lakenheath American High School at RAF Lakenheath, England in 1978 and attended the University of Notre Dame, graduating in 1982 with a Bachelor of Science in physics. He began active duty in the U.S. Air Force the same year, serving initially as a physicist at the Foreign Technology Division, Wright-Patterson AFB, OH, where he worked on a variety of infrared remote sensing projects. He received a Master of Arts in Political Science (International Affairs) from the University of Dayton in 1985. In 1986, he transferred to Detachment 4, Foreign Technology Division, Yokota AB, Japan, where he served as scientific/technical liaison to U.S. Pacific Air Forces, allied air forces in Korea, Japan, and Thailand, and the Japanese defense scientific community. In 1989 he transferred to the 544th Strategic Intelligence Wing (SAC), Offutt AFB, NE. There he headed SAC's effort to model at the engineering level the ability of advanced bombers and cruise missiles to penetrate hostile air defenses. As part of his duties, he advised SAC's bombers participating in Operation DESERT STORM on the technical capability of Iraqi air defenses. He entered the School of Engineering, Air Force Institute of Technology, in May 1992. He received a Master of Science in Engineering Physics and the Edwin S. Aldrin, Sr. Award for student leadership in December 1993. He began his doctoral studies in January 1994.

[REDACTED]:

[REDACTED]
[REDACTED]

REPORT DOCUMENTATION PAGE

Form Approved
OMB No. 0704-0188

Public reporting burden for this collection of information is estimated to average 1 hour per response, including the time for reviewing instructions, searching existing data sources, gathering and maintaining the data needed, and completing and reviewing the collection of information. Send comments regarding this burden estimate or any other aspect of this collection of information, including suggestions for reducing this burden, to Washington Headquarters Services, Directorate for Information Operations and Reports, 1215 Jefferson Davis Highway, Suite 1204, Arlington, VA 22202-4302, and to the Office of Management and Budget, Paperwork Reduction Project (0704-0188), Washington, DC 20503.

1. AGENCY USE ONLY (Leave blank)	2. REPORT DATE	3. REPORT TYPE AND DATES COVERED
	January 1997	Doctoral Dissertation
4. TITLE AND SUBTITLE Four-Wave Mixing and Optical Phase Conjugation in Vertical Cavity Surface Emitting Lasers		5. FUNDING NUMBERS
6. AUTHOR(S) Gregory J. Vansuch, Major, USAF		
7. PERFORMING ORGANIZATION NAME(S) AND ADDRESS(ES) Air Force Institute of Technology/ENP 2950 P Street, Bldg 640, Area B Wright-Patterson AFB, OH 45433-7765		8. PERFORMING ORGANIZATION REPORT NUMBER AFIT/DS/ENP/97-01
9. SPONSORING/MONITORING AGENCY NAME(S) AND ADDRESS(ES) Wright Laboratory WL/AAJL Wright-Patterson AFB, OH 45433		10. SPONSORING/MONITORING AGENCY REPORT NUMBER
11. SUPPLEMENTARY NOTES		
12a. DISTRIBUTION / AVAILABILITY STATEMENT Approved for public release; distribution unlimited		12b. DISTRIBUTION CODE
13. ABSTRACT (Maximum 200 words) Four-wave mixing (FWM), a nonlinear optical process, was investigated in resonant cavity light emitting diodes (RCLEDs) and vertical cavity surface emitting lasers (VCSELs) below lasing threshold. These semiconductor photonic devices consisted of an optical gain region of quantum wells sandwiched between two distributed Bragg reflector (DBR) mirrors. Pump and probe lasers were injected into the devices to generate FWM. The dependence of FWM on bias current, pump laser power, and spectral and spatial separation between pump and probe lasers was investigated experimentally. A computer model of FWM based on the wave and carrier density equations was developed and agreed well with experimental results. Conjugate reflectivities of 1 were obtained in the VCSEL when bias current was below threshold but above transparency. Reasonable conjugate reflectivities were obtained for pump-probe detunings up to 2 GHz in both devices. Noncollinear FWM was performed for the first time in VCSELs or RCLEDs at angles up to 10°. Both experiment and model showed the possibility of generating a strong reflected conjugate signal while minimizing the reflected pump signal. The noncollinear FWM demonstrated the possibility of phase front conjugation for correcting aberrated signals in vertical cavity devices.		
14. SUBJECT TERMS Four-Wave Mixing, Nonlinear Optics, Optical Phase Conjugation Semiconductor Lasers, VCSEL, RCLED, Vertical Cavity Surface Emitting Laser		15. NUMBER OF PAGES 137
		16. PRICE CODE
17. SECURITY CLASSIFICATION OF REPORT Unclassified	18. SECURITY CLASSIFICATION OF THIS PAGE Unclassified	19. SECURITY CLASSIFICATION OF ABSTRACT Unclassified
		20. LIMITATION OF ABSTRACT UL